Development of Fission Gas Swelling and Release Models for Metallic Nuclear Fuels

by

Nathan Christopher Andrews

B.S. Nuclear Engineering
The Pennsylvania State University, 2010

SUBMITTED TO THE DEPARTMENT OF NUCLEAR SCIENCE AND ENGINEERING
IN PARTIAL FULFILLMENT OF THE REQUIREMENTS FOR THE DEGREE OF

MASTER OF SCIENCE in NUCLEAR SCIENCE AND ENGINEERING

AT THE

MASSACHUSETTS INSTITUTE OF TECHNOLOGY

June 2012

Signature of Author: _____
Department of Nuclear Science and Engineering
May 2012

Certified by: _____
Mujid S. Kazimi
TEPCO Professor of Nuclear Engineering
Thesis Adviser

Certified by: _____
Michael J. Driscoll
Professor Emeritus of Nuclear Engineering
Thesis Reader

Accepted by: _____
Mujid S. Kazimi
TEPCO Professor of Nuclear Engineering
Chairman, Committee for Graduate Studies

Development of Fission Gas Swelling and Release Models for Metallic Nuclear Fuels

by

Nathan Christopher Andrews

Submitted to the Department of Nuclear Science and Engineering
on May 9, 2012 in Partial Fulfillment of the Requirements for the
Degree of Master of Science in Nuclear Science and Engineering

ABSTRACT

Fuel swelling and fission gas generation for fast reactor fuels are of high importance since they are among the main limiting factors in the development of metallic fast reactor fuel. Five new fission gas and swelling modules for the fast reactor metallic fuel code FEAST-METAL were developed. This increases the number of degrees of freedom in the code and enhances the science -based modeling options for fuel swelling. All of the modules developed were benchmarked against data from EBR-II. Particularly, the code was benchmarked against U-19Pu-10Zr fuel and was applied to U-6Zr fuel.

The modifications made still kept the overall GRSIS algorithm present in the code. The GRSIS model tracks "closed" and "open" bubbles. The new modifications increased the number of closed bubble groups used in the algorithm, inserted a model that changed the bubble groups from being based on constant volumes to ones with constant numbers of atoms, added phase dependence and reexamined closed bubble spacing through the implementation of a Monte-Carlo algorithm to calculate the effective distance between the nearest bubbles.

All model options added to the code predicted the swelling, fission gas release and cladding strain effectively for the benchmark cases. However, significant differences in the results were found when the codes were applied to long-term U-6Zr fuel. The differences in the results cannot be resolved without more data on fuel behavior under irradiation; particularly, breeder fuel (blanket) data is needed to develop effective benchmarks. Until more data becomes available, it is advisable to use the original two group constant volume version of the code and the phase dependent version of the code and compare the results. The latter offers a much more scientifically based version of the code.

Sensitivity analysis to the number of bubble groups indicate limited benefit may be obtained by using more than 2 bubble sizes. Additionally, care should be taken to ensure that the axial nodding of the fuel be such that the axial mesh length is smaller than 10% of the fuel length. Furthermore, if the FEAST code is to be used in a coupled fashion with the coolant sub-channel analysis code COBRA, the accuracy of the results depend on the model used for fuel swelling.

Thesis Adviser: Mujid S. Kazimi
Title: TEPCO Professor of Nuclear Engineering

Thesis Reader: Michael J. Driscoll
Title: Professor Emeritus of Nuclear Engineering

Acknowledgements

This work was supported by TerraPower LLC, to whom I am very thankful for funding my research and allowing me the opportunity to continue my studies in nuclear engineering. In conjunction with this, I would particularly like to thank Pavel Hejzlar, who served as my contact at TerraPower.

I owe a great debt to my adviser Professor Mujid S. Kazimi. He has helped me to become a better thinker, researcher and engineer. Discussions with my adviser and other members of the Fuel Development Group at the Center for Advanced Nuclear Energy Studies (CANES) significantly aided me in the completion of this research.

Dr. Aydin Karahan, who originally developed the code FEAST-METAL and worked with me for my first year in graduate school, was also an invaluable resource.

The lads and lasses of Marth are acknowledged for their general support: William Herbert, Elison Matioli, Alexandre Guion, Samuel Humphry-Baker, Katy Stout, Federico Cismondi, Ines Gaisset and Benjamin Mailly.

Finally, I thank my family. My father, Dr. Steven Andrews; my mother, Barbara Andrews; and my sister, Maria Andrews, have continually supported me in my endeavors both academic and humanistic.

Table of Contents

List of Figures

List of Tables

1. Introduction

Fast reactors in both the United States and in Europe developed two main types of fuel that were extensively tested. The first type of fuel is mixed oxide (MOX) using oxides of uranium, plutonium and other actinides. The second type of fuel is metallic fuel, which primarily consists of uranium, zirconium and plutonium. Both of these types of fuels have been extensively tested in reactors both in the United States and in Europe. The EBR-II in the United States, Phenix and Superphenix in France and the BN-600 in Russia all proved the viability of fast reactor technology based on these fuel types for the generation of large amounts of electricity. Carbide and nitride fuels, while tested, have not been as extensively characterized because of the success of oxide and metallic fuel in the 1980s and 1990s. More recently, the push towards the creation of new Generation IV reactors has renewed interest in the development of liquid metal fast reactors. New reactor concepts proposing ultra-high burnups (~35 at%) and extended cycle lengths (~40 years) are currently being developed. One such example is the Travelling Wave Reactor proposed by TerraPower. [1] These reactors are all Liquid Metal Fast Reactors (LMFR) and are sodium cooled.

One of the main constraints in the development and deployment of this type of reactor is the fuel itself. Due to the fast flux environment and the use of sodium as a coolant, the degradation and failure of materials and fuel is the limiting factor to increasing burnup. Because of the large difference in the environment of a fast reactor in comparison to a light water reactor (LWR), the tools developed for the materials and fuel analyses of LWR systems were not viable for use in fast reactors. Because of this, an entirely different set of codes was needed. This necessity led to the development a large number of fuel performance codes for both oxide and metallic fuels. Due to the large difference in behavior between the ceramic oxide fuel and the oxide fuel, one code cannot model both oxide and metallic fuel without separate modules.

This thesis focuses on the improvement of the fuel performance code FEAST-METAL, which was developed to simulate the performance of metallic fuel and its cladding in a liquid sodium environment. In particular, the fission gas and swelling modules of FEAST-METAL are examined. In this section, background information necessary to understanding metallic fuel and fast reactors will be presented. Its physical behavior under irradiation and modeling tools developed to predict its behavior are addressed accordingly.

1.1. Metallic Fast Reactor Fuel Overview

Metallic fuel as we know it is composed of uranium, plutonium and zirconium. A cylindrical slug made up of a composite of these three elements is encased in stainless steel cladding. The gap between the fuel and the clad is filled with sodium which increases conductance between the clad and the fuel, reducing peaking. See Figure 1. This section discusses the development of this fuel and some of the physical phenomena that occur when it is irradiated. Particularly it covers fuel swelling, constituent redistribution, phase structure and morphology, fission gas release, fuel clad chemical interaction and fuel clad mechanical interaction.

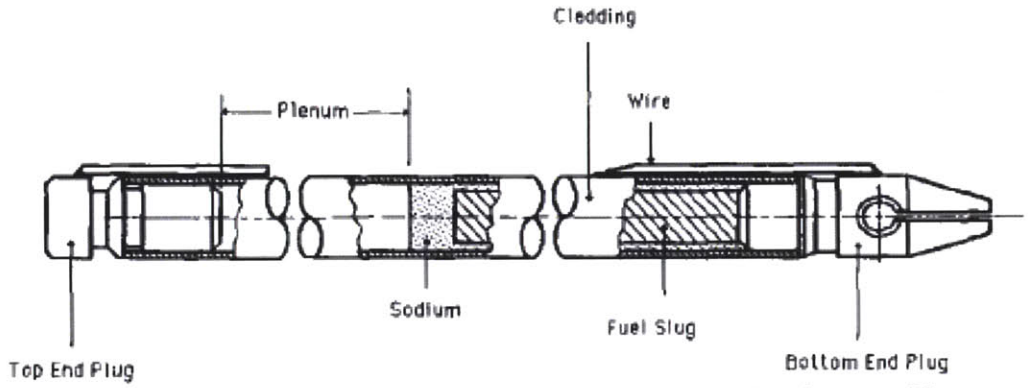

Figure 1: Typical metallic fuel pin from EBR-II, showing key features. [2]

In comparison to oxide fuels and other ceramics, metallic fuel carries a number of advantages. High thermal conductivity in the fuel leads the system to have a passively safe response to anticipated-transient-without-scram initiators in metallic-cooled fast pool reactors. High thermal conductivity also leads the fuel to have a lower peaking factor; thus allowing a higher linear pin power. Also, experimental testing has shown that the fuel can reach near 20 at% burn-up without failure. [3] The heavy metal density and low moderating power provide a harder spectrum, allowing better neutron economy than oxide fuels. [4]

The facility with the largest amount of data on metallic fuel irradiations is EBR-II, which operated at what is now the Idaho National Laboratory (INL). Through testing at EBR-II and other facilities, the fuel was demonstrated to be safe in both transient and steady-state operation. After pin failure, metallic fuel is quickly cooled due to its high porosity. If a pin failure occurs during normal

operation, the core can still be run without further degradation at the location of the breach. Tests in EBR-II demonstrated the ability for fuel to be irradiated up to 200 days after failure [5] The inclusion of zirconium in the fuel prevents a large release of iodine, which is a one of the most common fission products. While reprocessing the fuel is relatively simple, the fission products can never be fully separated from the fuel, reducing the possibility of using plutonium and other actinides for weapons.

Current metallic fast reactor fuel is initially a homogenous mixture of U-Pu-Zr in varying weight percent. Plutonium concentration varies from 0-19 wt%, while zirconium concentration is typically 6-10 wt%. In EBR-II, uranium enrichment was high and ranged from 60 to 90 wt% and over. [6] These percentages depend primarily on whether the fuel is part of the blanket or initial central core (driver fuel). The fuel cannot simply contain uranium and plutonium because the melting point of the solution is too low. Zirconium is a good added material because it both reduces the effect of fuel-clad-chemical interactions and raises the solidus. The concentration of zirconium is limited to roughly 10% because the fuel can no longer be cast into molds if it is present in a higher weight fraction. [5] To form the fuel, it is heated up and cast into quartz molds. [7] The smear density of the fuel is usually between 60% and 75%. [6] The rest of the clad interior has a sodium bond. Additionally, the fuel pin must have a large plenum to accommodate the large amount of fission gas that is released from the fuel matrix. See Figure 2. The low smear density is necessary because of the large amount of volumetric swelling the metallic fuel undergoes. The cladding is ferritic stainless steel, usually HT-9. Other steels were tested in the past, notably 316, D9 and 304, but their swelling rate was too high for them to be viable at higher burnups. [5]

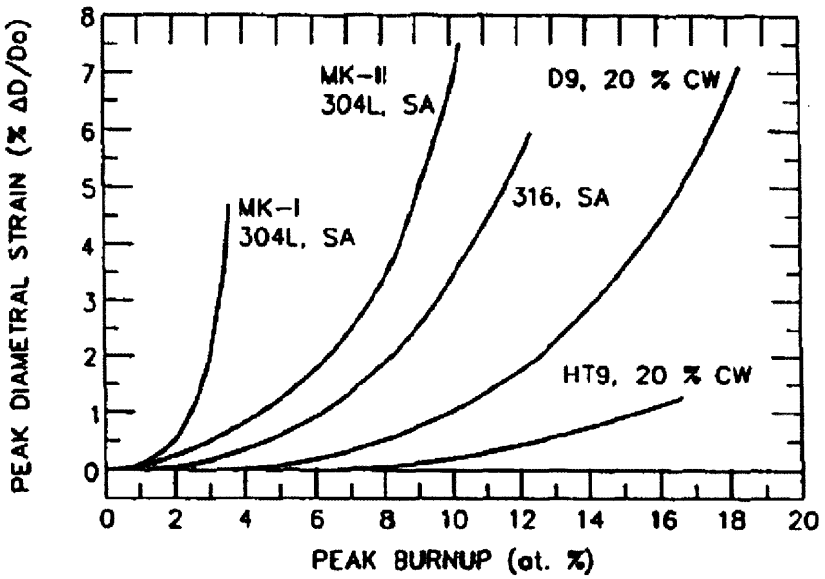

Figure 2: Comparison of various cladding materials for metallic fuels. [5]

1.1.1. Constituent Redistribution

Initially the fuel is a near homogenous solution of U-Pu-Zr in their initial concentrations. However, after irradiation begins, the thermal gradient created within the fuel causes the different phases in the fuel to form, corresponding to different regions of the ternary phase field. These different phases have different concentrations of zirconium and uranium. These different phases ultimately lead to the diffusion of zirconium and uranium into and out of specific radial regions of the fuel. Thermo-transport may also be a contributing factor to this redistribution. [8] Modeling this phenomenon is important because each of the fuel regions has its own unique characteristics. Figure 3 shows the formation of three distinct regions within the fuel. The center and outer regions have become enriched with zirconium, while the middle region is depleted. The uranium conversely has a higher concentration in the middle region and is depleted in the center and outer regions. The plutonium concentration shows a slight gradient from the center to the fuel exterior. [9]

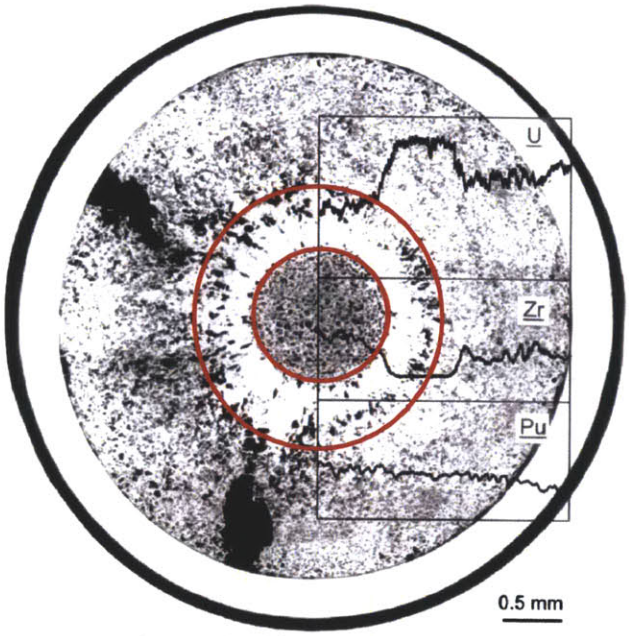

Figure 3: Axial cross section of the fuel with an overlay showing the radial distribution of the elements present for a U-19Pu-10Zr fuel pin from EBR-II at 1.9 at% burnup. [9]

1.1.2. Fuel Phase Structure and Morphology

Because the fuel is a ternary alloy consisting of U-xPu-yZr or a binary alloy of U-yZr, the phase structure of a fuel slug can become very complex when the temperature gradient and subsequent constituent redistribution is taken into account. The ternary alloy phase diagram can be seen in Figure 4, while the binary alloy phase diagram can be seen in Figure 5.

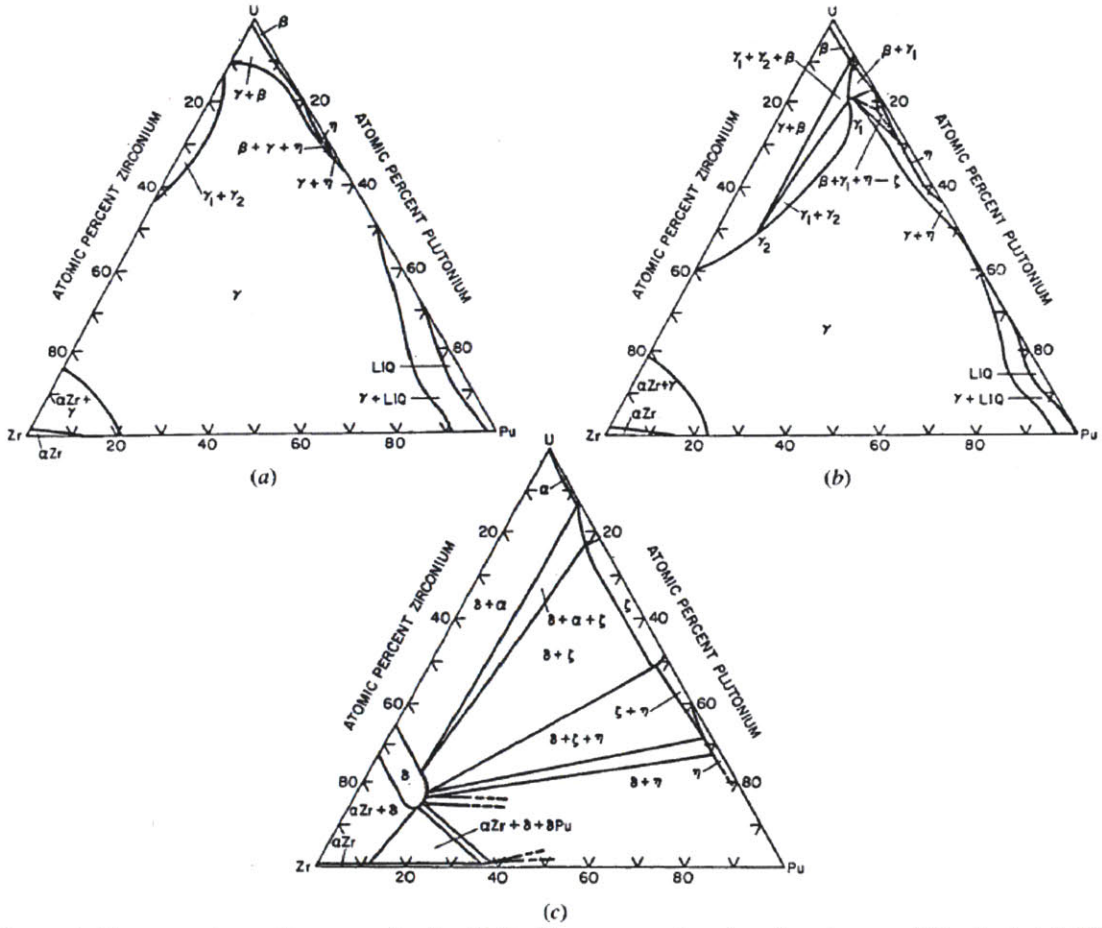

Figure 4: Ternary phase diagrams for the U-Pu-Zr system, showing the phases of the fuel. (a) 700 C, (b) 670 C, (c) 500 C [10]

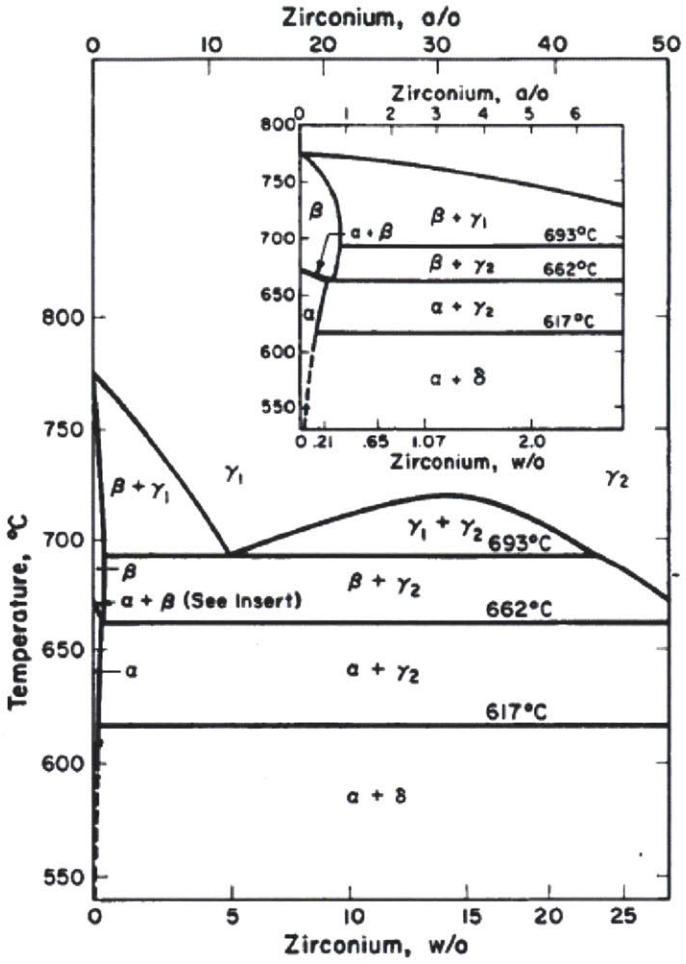

Figure 5: Binary uranium-zirconium phase diagram [10]

In a ternary alloy, three main regions form. Figure 3, Figure 6 and Figure 7 all show this three-region nature in different ways. Figure 3 in the preceding sub-section shows the axial cross section; Figure 7 shows a radial cross section; Figure 6 shows a calculated radial temperature distribution. All are of a U-19Pu-10Zr fuel pin. [9]In fuel with this make-up, the central region become γ phase, the outer region becomes $\delta + \zeta$ and the intermediate region becomes $\gamma + \zeta$. [9]Each of these different regions has a distinct morphology and behaves differently under irradiation. Figure 7 shows the morphology of each of these different regions. The issue is further complicated when the diffusion of gas atoms through this three-region fuel slug, and the constituent redistribution of uranium and zirconium is taken into account. Each of these three regions has a different amount of porosity created by fission gas, a different thermal conductivity and different mechanical properties.

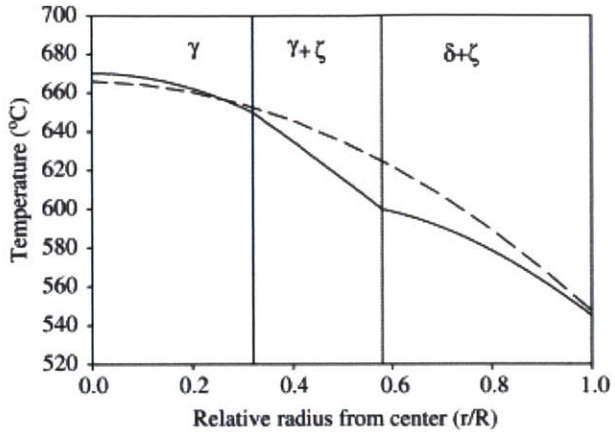

Figure 6: Calculated temperature distribution of EBR-II pin T-179 at axial location x/L=0.67 from the bottom showing phase fields. The dashed line is the beginning of life temperature and the solid line is the temperature distribution later in life. [9]

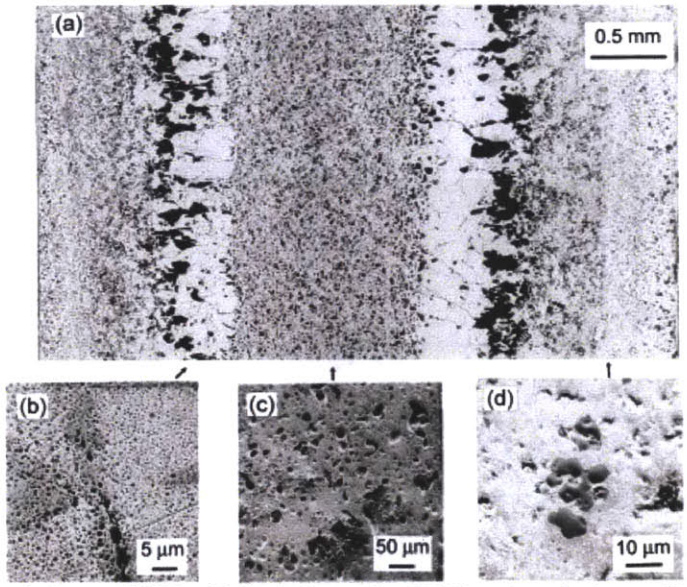

Figure 7: Pore morphology of U-Pu-Zr fuel shown by SEM and optical metallography: (a) optical micrograph of axial cross section, SEM image of, (b) intermediate zone, (c) central zone, (d) outer zone. [9]

Additionally, fuel that has a different initial composition of uranium, plutonium and zirconium will have different phases present in the fuel slug. For instance, the U-10Zr fuel has three radial phase regions. However, these phase rings are different from those in the U-19Pu-10Zr fuel. This can be seen by referencing Figure 3. The main phase regions for this binary fuel are the central $\beta + \gamma$, the

outer $\alpha + \delta$ and the intermediate $\alpha + \gamma$. If the temperature is high enough, then a γ-only region can also form. [10]

1.1.3. Fuel Swelling

Swelling in metallic fuel is primarily a result of fission gas release, irradiation growth, grain boundary mechanical cavitation and solid fission product accumulation. [10] Fission gas release and grain boundary cavitation cause both open and closed porosities. Solid fission product formation is linearly dependent on burnup, since it is dependent on the fluence. Due to the different phases present in the fuel, swelling is highly anisotropic.

Anisotropic irradiation growth of single crystals occurs in orthorhombic alpha uranium, which primarily forms between 400 C and 650 C. In this phase {010} elongation and {100} shrinkage occur simultaneously due to the anisotropic condensation of interstitial and vacancy loops. [10] This anisotropic growth causes mismatched stresses and results in cavities forming in the fuel. [10]Here the zirconium can form the hexagonal delta phase (UZr_2), the tetragonal zeta phase, or precipitates stabilized by oxygen, carbon or nitrogen. [10] Though these cavitation voids are partially filled with lanthanide-rich fission products, these tears are relatively compressible, unless filled by fission gas due to migration at higher burnup. [5] [10]

Fission gas, particularly Kr and Xe, nucleates into bubbles which migrate to phase boundaries; eventually they migrate from there to the fuel surface, where the contents of the bubble are released to the plenum. [10] When the gas bubbles are contained within the matrix of the fuel, they are considered closed porosity. When they are connected to the plenum, they are considered open porosity. Open porosity begins at roughly 0.5 at% burnup, which corresponds to ~10% volumetric swelling. This is an experimental data point. Metallic fuel codes use one of the two previous conditions to trigger the release of fission gas from the fuel matrix.

Solid fission products accumulate linearly with burnup, since their rate of production is dependent on the fluence. They account for roughly 1.2% volumetric swelling per atom percent burnup. [5]

While this is not a limiting condition at burnups less than 20 at%, it can become a primary failure mechanism if burnup is increased to 30 at% or higher. The primary solid fission products are Mo, Ru, Pd and the lanthanide series. [10]

Fuel swelling occurs rapidly after irradiation starts and does not see a decrease in rate until the fuel becomes radially restrained by the clad. The fuel becomes radially restrained at roughly 2 at% burnup which corresponds to 15 to 25 at% burnup. [10] At this point the swelling rate decreases because of the pressure exerted on the fuel by the cladding. The cladding is not breached because, at this point, the fuel contains a large amount of open porosity, which becomes sintered as the pressure on the fuel increases. The average radial swelling ($\Delta d/d_0$) was greater than the axial swelling ($\Delta l/l_0$) of the fuel by a factor 2 to three. This is thought to be a result of the manufacture process and the directional solidification of the alloy in its quartz mold. [10] Axial fuel swelling can be found experimentally, while radial fuel growth is not directly found because of the difficulties in making a measurement. Axial growth also has a large dependence upon the concentration of plutonium in the fuel; larger concentrations of plutonium lead to smaller axial fuel growth, which corresponds to a larger degree of fuel anisotropy deformation. [10]

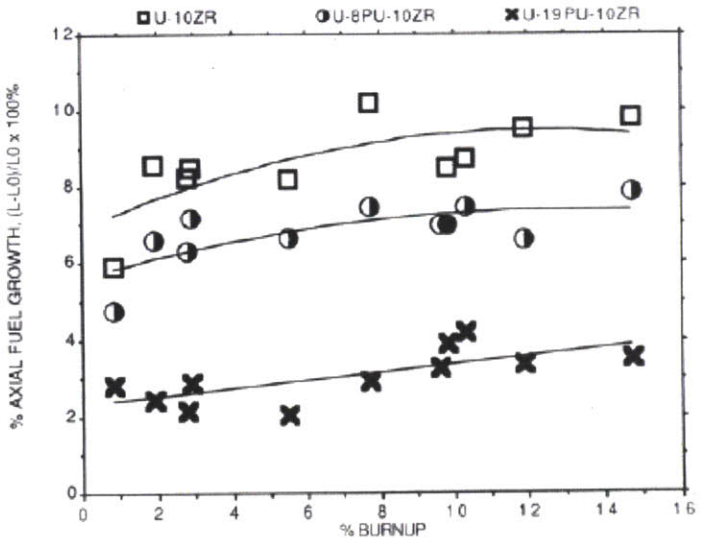

Figure 8: Axial fuel growth as a function of burnup and plutonium content [11]

1.1.4. Fission Gas

Because fission gas is the primary cause of pin swelling and thus cladding strain, understanding the mechanisms of fission gas release and retention is of utmost importance. This thesis, in fact, focuses on new ways to model this phenomenon in the code FEAST-METAL. Based upon experimental results, some conclusions can be made about the behavior of the fission gas. The quantity of gas which percolates into the pin plenum shows a nearly linear dependence on burn-up, once an initial gas formation period of about 0.5 at% has passed. [11]

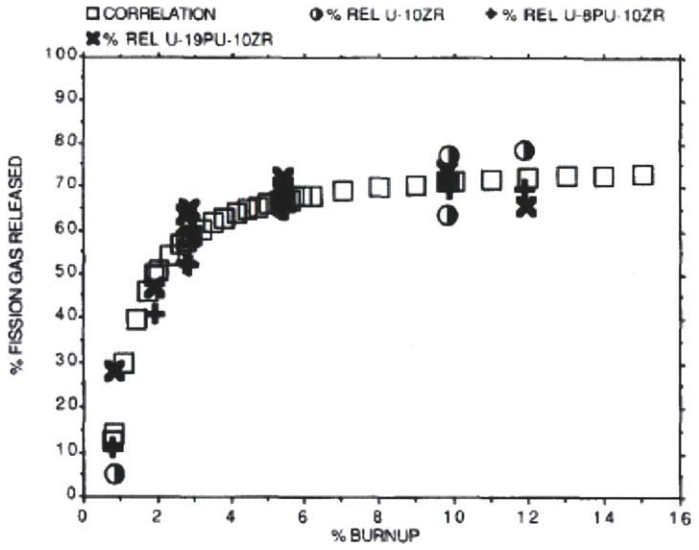

Figure 9: Fractional fission gas release behavior in U-xPu-10Zr metallic fuel [11]

Figure 9 shows that fractional gas release (the percentage of gas that is created that is released from the fuel matrix to the plenum) increases rapidly and asymptotically reaches a maximum of 60% to 80% depending on the fuel initial composition and irradiation history. Finally experimental studies show that there is little axial variation in the rate of fission gas release, indicating that temperature and diffusion distance to the plenum are not driving forces. [11] Open porosity is attained at a low burnup, which is apparent in Figure 9. Fission gas cannot be released unless there are open pores in the fuel. This means fission gas release occurs at all relevant temperatures. Figure 10 shows the total amount of gas released as a function of burnup.

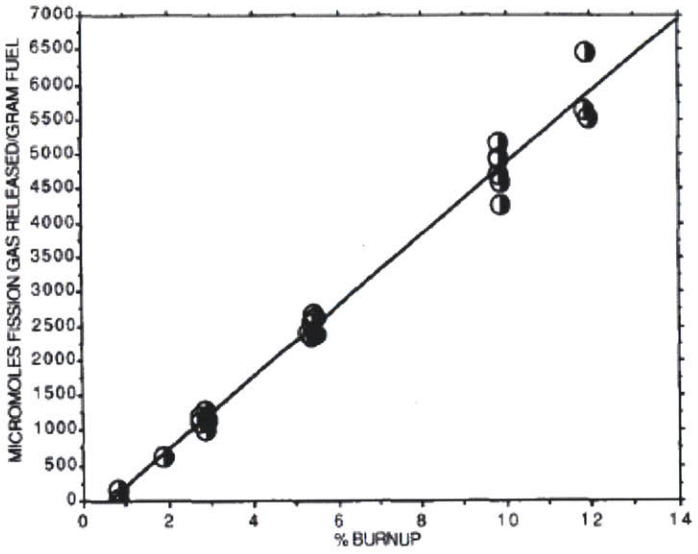

Figure 10: Total amount of fission gas released as a function of burnup for U-xPu-10Zr fuels (includes 0, 8 and 19 wt% Pu) [11]

1.1.5. Fuel Clad Mechanical Interaction (FCMI)

The creation of solid fission products and fission gas within the fuel matrix causes the fuel to swell until it reaches the cladding. When it is there it will exert pressure upon the cladding, resulting in creep and possibly causing failure. This was a limiting factor in the design of early metallic fuel, which had a higher smear density. Original smear density was ~85%; current fuel has a smear density of ~75%. [7] When the fuel touches the clad, the porosity of the fuel becomes compressed, but the fuel can only be compressed up to a certain point and eventually failure occurs due to the pressure exerted by the formation of solid fission products. At low smear densities, only when a low-swelling cladding material such as HT-9 is used does FCMI become an issue. The hoop strain of D9, 316 and 304 stainless steels seen in Figure 2 can all be accounted for by cladding creep due to plenum pressure and irradiation swelling. [5] At very high burnups, FCMI becomes the limiting factor, because the smear density of the fuel can only be effectively reduced to a certain point and solid fission product swelling is increases linearly with burnup.

1.1.6. Fuel Clad Chemical Interaction (FCCI)

Since both the fuel slug and its stainless steel cladding are both alloyed metals, the problem of interdiffusion between constituents of the cladding and fuel and fission products can be a limiting factor. Diffusion between the clad and the fuel can result in structural weakening of the clad and the formation of low melting point compositions in the fuel. [5] Fe and Ni diffuse into the fuel, while lanthanide fission products diffuse into the clad. Lowering the melting point of the fuel limits the transient performance and off-normal capabilities of the fuel pin. Penetration of lanthanides leads to the formation of an interaction layer that grows with burnup. This region is harder and more brittle than the rest of the clad and limits steady state performance. [11] The resultant interaction layer can be seen in Figure 11.

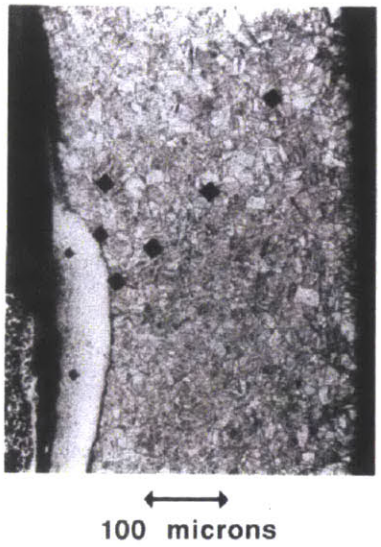

Figure 11: SEM of the interaction between D9 cladding and U-Pu-Zr fuel at ~12 at% burnup showing the increased hardness of the interaction region [11]

1.2. Metallic-Fueled Fast Reactors

This section provides an overview on the operational history of EBR-II and a synopsis of the Travelling Wave Reactor concept developed by TerraPower. Both of these reactors utilize ternary U-Pu-Zr fuel. Additionally, the EBR-II fuel experience is used to benchmark the FEAST-METAL code. Fuel irradiations similar to those used in the Travelling Wave Reactor are also examined for long-term cases. The Phenix, Superphenix and BN-600 reactors are not discussed in depth since they did not use metallic fuel and are therefore provide neither benchmark nor test cases for this thesis.

1.2.1. EBR-II

The Experimental Breeder Reactor-II (EBR-II) operated at 62.5 MW_{th} and 20 MW_e; it was a pool type reactor cooled with sodium. It operated for 30 years, going critical in 1964. The reactor itself was immersed in a 90,000 gallon pool of molten sodium. The core was surrounded by both axial and radial uranium blankets which were used to generate (breed) plutonium. The reactor ran on both metallic and oxide fuel pins. [7]

Early in the life of the reactor, the burnup of fuel pins were severely limited by material, fuel design and hexagonal ducts which contained the fuel. Stainless steel, that was originally used as cladding, had a much higher swelling rate than the HT-9, that was used later in life. Early fuel designs had a much higher smear density than 75%. Initially the smear density ranged from 85% to 100%. This high smear density did not accommodate the large amount of fission gas swelling that occurs in metallic fuel, leading to fuel pin failure at low burnup. The stainless hexagonal ducts that contained fuel pins underwent significant deformation due to swelling as a result of irradiation. These material and design shortcomings were eventually fixed, and the burnup limit increased accordingly. The burn-up limit for different fuel pin designs can be seen in Figure 12. [7]

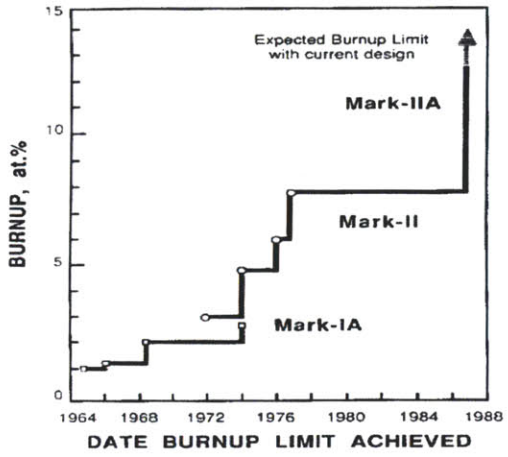

Figure 12: Burnup limit for different generations EBR-II driver fuel [7]

The initial fuel used in the reactor was a combination of uranium and fisium (Fs), which is an equilibrium concentration of fission product elements left by the pyro-metallurgical reprocessing cycle. [7] Mark-IA fuel had U-5Fs fuel and was clad in austenitic stainless steel. [7] Mark II fuel also used U-5Fs fuel but was clad in 304 stainless steel; later in 316 stainless steel was also used as cladding. [7] Eventually this fuel evolved into the ternary U-Pu-Zr fuel described in the previous section. The fuel itself was formed by injection casting into quartz molds, a process which can be seen in Figure 13. [7] Mark IIA fuel used ternary fuel and was clad in ferritic stainless steel (D9 or HT9).

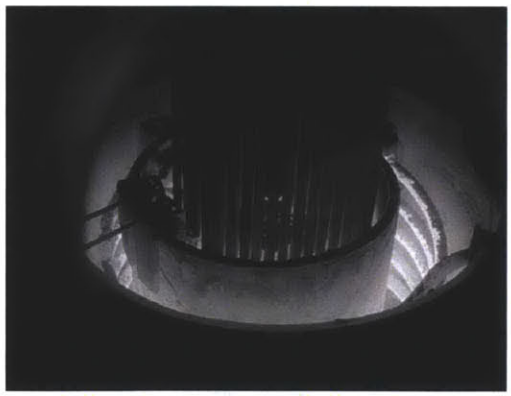

Figure 13: EBR-II fuel pins being fabricated by injection casting. [7]

In order to determine which specific fuel pin failed, each pin had a unique mixture of xenon in the plenum. When a pin failed, the gas would escape and be detected by a mass spectrometer, leading to easy identification. This allowed the exact time of cladding failure to be determined. The highest burnups for the EBR-II, roughly 20 at%, were achieved for low smear density fuel clad in HT-9.

Cases from EBR-II were used to benchmark the FEAST-METAL codes developed in this thesis. More information on the irradiation history of those pins is included in the section of this report which details the benchmarks performed. [7]

1.2.2. Travelling Wave Reactor

The Travelling Wave Reactor (TWR) is a reactor currently being engineered by TerraPower LLC. It aims to offer significant advantages over both LWRs and traditional fast reactor technologies. Namely, it aims at being fueled with internally generated fissile material for most of its life. Like many other fast reactor designs, this reactor makes use of blanket and driver regions. The central region is at a much higher power initially due to its fuel with higher enriched heavy metal. The fast fission neutrons are absorbed in the blanket region, resulting in fertile isotopes there becoming fissile. When the central region of the core begins to lose reactivity, the newly made fissile isotopes are moved from the outer blanket region to the central region. Figure 14 shows this core schematic. [1]

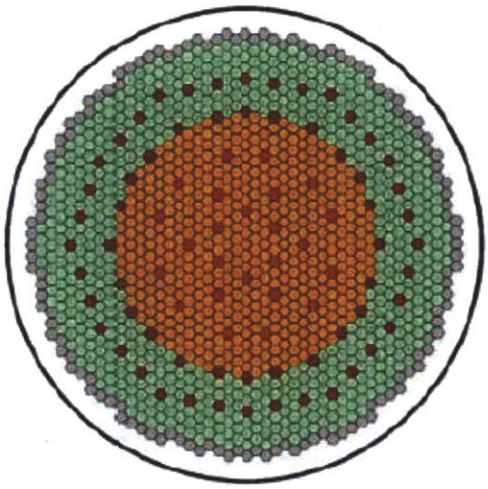

Figure 14: Core layout of TerraPower's TWR, showing the central (orange) and blanket regions (green) [1]

The proposed design has the capability of fuel utilization roughly forty times greater than a conventional LWR, which uses 0.79% of mined uranium. A first generation TWR could maintain

criticality to near 15 at% burnup, while later generations could remain critical to over 40 at% burnup. However, with so high a desired burnup, the radiation resistance requirements placed on the materials in the reactor become much greater. FEAST-METAL and other metallic fast reactor fuel codes are currently being used to evaluate the performance of TWR fuel under the conditions proposed by TerraPower. [1]

1.3. Fuel Performance Code Evolution

In order to predict the behavior of metallic fuel beyond current experimental data and to interpolate between existing points, fuel codes were developed to model the behavior of metallic fuel. This modeling especially becomes an issue when predicting behavior of the fuel well beyond the current data. The highest burnup data points correspond to 20 at% burnup, while for the proposed fuels it is desired to extend burnup to over 30 at%. Because the predictions are entirely dependent on the models used in the code, the development of codes based on physical principles is of the utmost importance. Experimental correlations cannot be used to extrapolate fuel behavior to 50% beyond the highest burnup data point. Because of this, metallic fuel codes have moved away from empirical correlations to physics-based models. Although, without experimental proof, these models cannot be verified; they are an improvement over a purely extrapolated and empirical approximation. This thesis focused on improving the fission gas and swelling module of the code FEAST-METAL. In order to better understand previous models that were created and used, a literature review of fission gas modules of each of these codes was conducted. In addition, the general capabilities of each of the relevant Metallic fuel codes were reviewed and discussed in this section. Table 1, which is taken from Karahan's thesis, covers the basic models present in relevant codes and their capabilities.

Table 1: Steady-state metallic fuel performance codes [4]

Modules	LIFE-METAL	SESAME	ALFUS	MACSIS	FEAST-METAL
Developer	ANL (US)	CRIEPI (JAPAN)	CRIEPI (JAPAN)	KAERI (Korea)	MIT (US)
General Capabilities	Steady-state and Transient Behavior	Steady-state Behavior	Steady-state Behavior	Steady-state Behavior	Steady-state and Transient Behavior
Fission Gas Release and Fuel Swelling	Empirical Correlation	Empirical Correlation	Mechanistic Model, based on UO_2 Fuel	Mechanistic Model, Based on UO_2 Fuel	Mechanistic Model, Based on Metallic Fuel
Constituent Redistribution	Empirical Correlation	Chemical Equilibrium Model	Thermo-transport theory	Thermo-transport theory	Thermo-transport theory
Temperature Distribution	1D Model	1D Model	1D Model	1D Model	1D Model
Mechanical Analysis	1D Model	1D Model	2D Model	1D Model	1D Model
FCCI	Empirical Correlation	Not Included	Empirical Correlation	Not Included	Diffusion Model based on Precipitation Kinetics
Creep Fracture	Cumulative Damage Fraction Model	N/A	N/A	N/A	(1) Cumulative Damage Fraction Model (2) Constrained Diffusional Cavity Growth Model

The most important physical phenomena that need to be modeled are discussed in detail in the Metallic Fast Reactor Fuel Overview section of this thesis. They include fission gas release, swelling, anisotropic fuel deformation, temperature, FCCI, mechanical behavior, creep fracture, constituent redistribution and phase structure. This section focuses on the five codes in the above table and the GRSIS and OGRES algorithms, which are used in some of these codes. Special emphasis is taken to describe the fission gas and swelling modules of each of the codes since these phenomena are the main focus of this thesis. This is done to show the wide range of current models.

1.3.1. LIFE-METAL

LIFE-METAL is an adaptation of the oxide code LIFE. It includes thermo-mechanical analyses of the fuel and cladding in the radial direction. The code can accommodate axial variation through different fast flux and specific power inputs. Fuel temperatures are based on calculated coolant temperatures at the given axial height. There is no axial coupling for either mechanical processes or temperatures. The code calculates fuel swelling and fission gas release based upon empirical correlations which use temperature, porosity and burnup as independent variables. Since porosity can be seen as a function of burnup and temperature, these are the two main driving variables for fission gas release and swelling determination. The swelling and fission gas release correlations are very similar to the SESAME models without a maximum bubble concentration correction. {See Equations 2 and 3} The code models both steady-state and transient behavior. For FCCI and constituent redistribution, empirical correlations based on EBR-II data are used. Overall, the code uses a 1D model for temperature and mechanical analyses. [4] [12]

1.3.2. SESAME

Since the code LIFE-METAL was not well developed in comparison to the mixed oxide fuel performance codes, the Central Research Institute of the Electric Power Industry in Japan developed their own code to model metallic fuel in a liquid metal environment. This code, SESAME, predicts steady-state irradiation performance of metallic fuels through the use of simple empirical correlations. The code uses a finite element method (FEM) with one degree of freedom for both the fuel temperature and stress-strain calculations. The fission gas release model is based on those employed in LIFE-METAL and are based on empirical relations dependent on burn-up and other fuel parameters. [12]

$$\dot{G}_r = F_g \cdot G_s \qquad \text{Eqn. 1}$$

$$F_g = [1 - \exp(-\alpha \cdot Bu)]\left[1 + C_g(P-.01)P^{\frac{2}{3}}\right] R_g \times \exp\left(-\frac{Q_g}{RT}\right) + f \cdot (\epsilon_s - \epsilon_i) \qquad \text{Eqn. 2}$$

$\dot{G}_r$: Fission product gas release rate (mol/sm^3)

G_s: Retained fission product gas (mol/m^3)

Bu: Burnup (at%)

P: Porosity

ϵ_s: Gas swelling (volumetric change)

T: Temperature (K)

α, C_g, ϵ_i: Dimensionless fitting parameters

$R_g, \frac{Q_g}{R}, f$: Dimensional fitting parameters

Like the fission gas release model, the fuel swelling model is also based on the LIFE-METAL code. Gas bubble radius is found by applying the equilibrium condition between internal gas pressure and external pressure plus surface tension. To find the concentration of fission gas atoms, the following relation is used. The minimum function is applied to better model the bottom of fuel pins, which was predicted incorrectly by LIFE-METAL. [12]

$$\boldsymbol{C_b = \min\left[B_b\, exp\left(\frac{Q_b}{RT}\right), C_{max}\right]} \qquad \textbf{Eqn. 3}$$

C_b: Fission product gas bubble density (#/m^3)

C_{max}: Maximum allowed concentration (#/m^3)

B_b: Dimensionless parameter

The code also models constituent redistribution and sodium bond infiltration into the fuel, which results from the fuel's high porosity. Finally, there are corrections to take into account the anisotropic deformation of the fuel. While the code is valid for examining the fuel from EBR-II, the fact that there are very few degrees of freedom in the empirical correlation developed, leads to questions about the code's ability to accurately model metallic fuel which has irradiation histories different from the types found in EBR-II. [12]

1.3.3. OGRES

The first use of multiple bubble groups in modeling the creation and release of fission gas in metallic fuel was performed in the OGRES code, which models fission gas swelling and release for ternary metallic fuel under steady-state conditions. The model was originally created for oxide fuel and then adapted to ternary metallic fuel. This model assumes that gas atoms that are generated in the fuel either precipitate together to form bubbles or remain dispersed within the fuel matrix. Both these atoms and bubbles then diffuse through the fuel matrix, eventually reaching the grain boundaries of the alloy. Bubble number density is determined by the same equilibrium analysis that SESAME uses. This model uses six different bubble group classifications. Five of the bubble groups represent closed bubbles, while one represents open ones. The probability that any gas is released is a function of local swelling. This code only models the formation of fission gas bubbles, related gas release and swelling. It does not couple these phenomena with mechanical, chemical or thermal properties. [13]

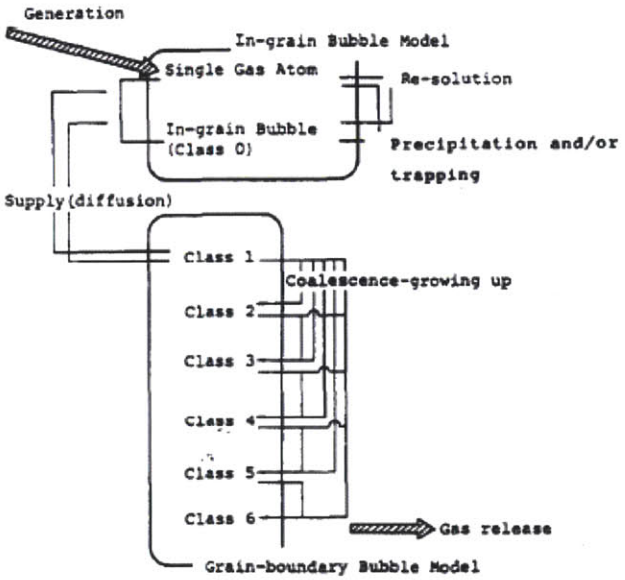

Figure 15: ORGRES fission gas behavior algorithm [13]

Fission product gas atom concentration can be explained by the following equation for in-grain bubbles. [13]

$$\frac{\partial C_t}{\partial t} = \frac{1}{r^2}\frac{\partial}{\partial r}\left(\left(D_g r^2 \frac{\partial C_g}{\partial r}\right) + \left(D_{gb} r^2 \frac{\partial C_{gb}}{\partial r}\right)\right) + K_g \qquad \text{Eqn. 4}$$

$$C_t = C_g + C_{gb} \qquad \textbf{Eqn. 5}$$

C_t: Total fission gas concentration (#/m^3)

C_g: Concentration of gas atoms dissolved in the fuel matrix (#/m^3)

C_{gb}: Concentration of gas included in the in-grain bubbles (#/m^3)

D_g: Diffusion coefficient of a single gas atom (m^2/s)

D_{gb}: Diffusion coefficient of in-grain bubbles (m^2/s)

K_g: Generation rate of FP atoms (1/m^{3}s)

Evaluated at steady state, this yields the rate of gas transfer from bubbles inside the fuel grain to the grain boundary. The concentration of bubbles within the grains can be found using the following relation for bubble types 1 to 5, which are all closed. Each closed bubble type has a constant number of atoms, resulting in a varying radius. [13]

$$\frac{dC_i}{dt} = G_i + \sum_{j=1}^{i-1} R'_{i-1,j} - \sum_{j=1}^{i} R'_{i,j} - \sum_{j=1}^{6} R_{i,j} \; ; \; i = 1 \; to \; 5 \qquad \textbf{Eqn. 6}$$

C_i: Number density of bubble type-i (#/m^3)

G_i: Increase in the number density of the type-i bubbles due to FP gas transfer from the grain (#/m^{3}s)

$R'_{i-1,j}$: Shifting rate of smaller bubbles to type-i bubble due to coalescence with type-j (#/m^{3}s)

$R'_{i,j}$: Shifting rate of type-i bubble to large bubbles (#/m^{3}s)

$R_{i,j}$: Collision rate of type-i bubbles with type-j bubbles, and hence the coalescence of the bubbles (#/m^{3}s)

The collision rates and shifting rates depend on the bubble class; however, they are all similar in form. [13]

$$R_{i,j} = 4\pi\delta(D_i + D_j)(r_i + r_j)C_iC_j \cdot M \qquad \textbf{Eqn. 7}$$

δ: Correction factor (1/2 when i=j, 1 in all other cases)

D_i: Diffusion coefficient of bubble type-i (m^2/s)

r_i: Radius of bubble type-i (m)

M: Mass correction or probability correction depending upon the bubble group

Open bubbles use a different concentration equation because they cannot collide with other bubbles because they are immobile, which is part of the definition of open porosity used in fuel codes. The variables here are the same as above with different indices. [13]

$$\frac{dC_6}{dt} = G_6 + \sum_{j=1}^{5} R'_{5,j} - \sum_{j=1}^{5} R'_{6,j} \qquad \text{Eqn. 8}$$

Based on this concentration, the rate of change of swelling is calculated as a function of both open and closed bubbles.

1.3.4. ALFUS

The ALFUS code (ALoyed Fuel Unified Simulator) mechanistically predicts the fission gas release rate and the deformation behavior of ternary U-Pu-Zr fuel. Unlike other metallic fuel performance codes, it incorporates a 2D mechanical analysis model; its temperature model is still 1D though. This code is also the first code to use a mechanistic model to predict the behavior of fission gas and related swelling. This aids in the determination of the fission gas release rate, the amount of anisotropic fuel deformation and the analysis of the FCMI. This code also mechanistically takes into account constituent redistribution, but it does not couple this to the mechanical model. The ALFUS fission gas model is based on the OGRES fission gas release model. The size of the grain-boundary bubbles used in the OGRES algorithm is fixed based upon a constant number of atoms. Accordingly, the radii vary. In comparison of the FEAST-METAL and the GRSIS algorithm it uses, there are a few differences. In-grain bubbles are treated explicitly by the ALFUS, while they are not done so in FEAST-METAL. Additionally probabilities of coalescence and diffusion rates of bubbles through the fuel are treated differently. The FCCI model is based on an empirical correlation. [14]

1.3.5. MACSIS

The MACSIS code is a steady-state which models temperature and fuel mechanics in 1D. Like other models, it uses thermo-transport theory for constituent redistribution and a mechanistic model based on UO_2 fuel to predict fission gas release and swelling. There is no FCCI or creep fracture module within the code. The fission gas release model involves two separate models for intra-granular and inter-granular fission gas release. The intra-granular model is based on Booth's classical diffusion theory. This model treats the release of fission gas from the fuel matrix as diffusion to the surface of a spherical grain. Gas is created uniformly with a radius of "a" at a rate of β. This leads to the following diffusion equation, which must be satisfied at all points. [15]

$$\frac{\partial c}{\partial t} = D\nabla^2 C + \beta \quad \text{where } 0 \leq r \leq a, t = 0 \text{ and } c = 0 \text{ at } r = a, t \leq 0 \qquad \text{Eqn. 9}$$

β: Gas atom generation rate (#/m^{3}s)

C: Concentration of gas atoms (#/m^3)

D: Diffusion coefficient (m^2/s)

a: Grain radius (m)

t: Time (s)

The quantity of gas released after a time "t" is found by integrating the divergent flux across the specimen boundary up to the time "t". This result is then fed into the inter-granular model, like the OGRES and GRSIS algorithms, which uses a multi-bubble group approach. Here multi-bubble size distribution on the grain boundary and the number of bubbles per unit volume at a specified bubble-i size $0 \leq r \leq a, t = 0$ is estimated based on the following equation. [15]

$$\int_{n_i}^{n_i+1} F(m, \tau, n)dn = \bar{f}_i(n_{i+1} - n_i) \qquad \text{Eqn. 10}$$

This can be rewritten:

$$\bar{f}_i(n_{i+1} - n_i) = .23m \cdot \tau^{\frac{4}{5}} \int_{n_i}^{n_i+1} \{\exp(-A(n\tau^{-\frac{2}{5}} - .5)\} \times \{\sinh\left[B\left(n\tau^{-\frac{2}{5}} - .5\right)\right]^{-\frac{2}{5}}\}dn \qquad \text{Eqn. 11}$$

f_i: Number of bubbles for median atom's size at given bubble size range

n_i: Number of gas atoms in the i size bubble

τ: Reduced time as a dimensionless constant

$m = \frac{m_{gb}}{E_t}$: The number of gas atoms per unit volume at the grain boundary surface

m_{gb}: Number of gas atoms per unit area on the grain boundary

E_t: The effective thickness of grain boundary

A, B: Dimensionless constants

The desired result here is the number of gas atoms per unit area on the grain boundary or m_{gb}. This can be found using f_i. [15]

$$m_{gb} = C_s \sum_{Size\ range} \bar{f}_i \cdot \frac{n_{i+1}+n_i}{2} \qquad \textbf{Eqn. 12}$$

C_s: Correlation coefficient for concentration per unit area of grain boundary

This can be rewritten to solve for C_s. Based on these equations, the number of bubbles in a given bubble size group is found to be: [15]

$$f_i = \bar{f}_i \cdot C_s \qquad \textbf{Eqn. 13}$$

From here a portion of the gas bubbles connect with one another and form larger bubbles. This continues until a saturation condition is reached and then the contents of the bubbles are released to the plenum. In the model, the point when bubble interconnection first begins is described in the following equation. [15]

$$\left(\frac{r_{sb}}{R_{sb}}\right)^2_{crit} = \frac{\pi r_{sb}^2}{(2r_{sb})^2} = \frac{\pi}{4} \qquad \textbf{Eqn. 14}$$

r_{sb}: Radius of a gas bubble (m)

R_{sb}: Radius of a circular unit cell of the grain boundary (specified parameter), (m)

From here the saturation condition at which gas release begins for a given location is described in the following manner. [15]

$$\frac{1}{4} = \sum_{Size\ range} r_{sb,i}^2 \cdot f_i \qquad \textbf{Eqn. 15}$$

For the purposes of gas swelling, the volume of a bubble is determined according to the van der Waals equation based on the number of gas atoms in the bubble. With these radii, the total swelling is calculated with the following equation. This is then used to determine diametrical fuel and clad change. Since the code uses 10 separate annuli, it is summed over all of these; it is also summed over all bubble groups. [15]

$$\Delta V_s = \sum_{j=1}^{10} \left\{ \frac{\left[\frac{4}{3}\pi n_{ij} \Sigma_i r_{ij}^3\right]}{V_j} \right\} + f_s \qquad \textbf{Eqn. 16}$$

n_{ij}: Number of bubbles of size-i at annulus-j

ΔV_s: Total volumetric change due to fuel swelling

r_{ij}: Radius of bubble-i at annulus-j (m)

V_j: Volume of annulus-j

f_s: Solid Fission product volumetric change

1.3.6. GRSIS and FEAST-METAL

In comparison to previous codes, the FEAST-METAL code relies less on outright empirical correlations. However, fitting factors are still required to make the models valid. The code is capable of both transient and steady-state analysis. The fission gas model is based on the GRSIS algorithm. The GRSIS algorithm models the creation and diffusion of fission gas within a metallic fuel matrix. In logic, it is similar to the OGRES algorithm; however, there are significant differences in the treatment of in-grain bubbles, coalescence probabilities and diffusion properties. FCCI uses a diffusion model. A full analysis of relevant models in the FEAST-METAL code and the GRSIS algorithm is contained in the next chapter. Table 2 provides a comparison of the results (for clad strain at a given burnup) from the initial version of FEAST-METAL with ALFUS and LIFE-METAL. [4]

Table 2: Comparison of X425 peak clad strain for ALFUS, FEAST and LIFE [16]

Peak Burnup (at%)	Experimental Data	FEAST		ALFUS		LIFE	
		Clad Strain (%)	Relative Error (%)	Clad Strain (%)	Relative Error (%)	Clad Strain (%)	Relative Error (%)
10.4	.25	.22	-12.0	~.37	48.0	~.25	0.0
15.8	.98	1.0	2.0	~.86	-14.0	~.98	0.0
18.9	2.0	2.23	11.5	~1.55	22.5	~2.4	20.0

2. Relevant Models in FEAST-METAL Version 1

In order to improve the ability of FEAST-METAL to predict the cladding strain, axial elongation and fission gas release fraction that are used to benchmark the code against results from EBR-II, multiple models in the code were altered and re-written. This section contains a description of the models originally used in the first version of FEAST-METAL. While work primarily centered on the fission gas release module within the code, many of the alterations to it are directly related to other portions of the code. Hence, this section provides a high-level breakdown of the FEAST-METAL algorithm, as well as detailed descriptions of the fission gas release module, the fuel creep and plasticity model, the swelling model, the axial elongation model and the phase boundary model. These models were all directly impacted by the work of this thesis. The results obtained from the initial version of the code can be seen in Chapter 4, which details the results of the updates performed to the code.

2.1. The Overall FEAST-METAL Algorithm

FEAST-METAL takes as input operating conditions (burn-up, power, neutron flux, fast flux fraction, plutonium atom fraction and fission rate) and pin geometry and then determines the mechanical behavior of the fuel pin and surrounding cladding. The code inputs are axially discretized and radial geometry is taken into account at each of these axial locations. A flow chart of the process of the algorithm can be seen in Figure 16. All of the results from one time step are taken as the initial conditions for the next one. Additionally, the outputs from one module are taken as inputs for the others, leading all of the separate modules in the code to be linked to each other and to the values of parameters from the previous step. [4]

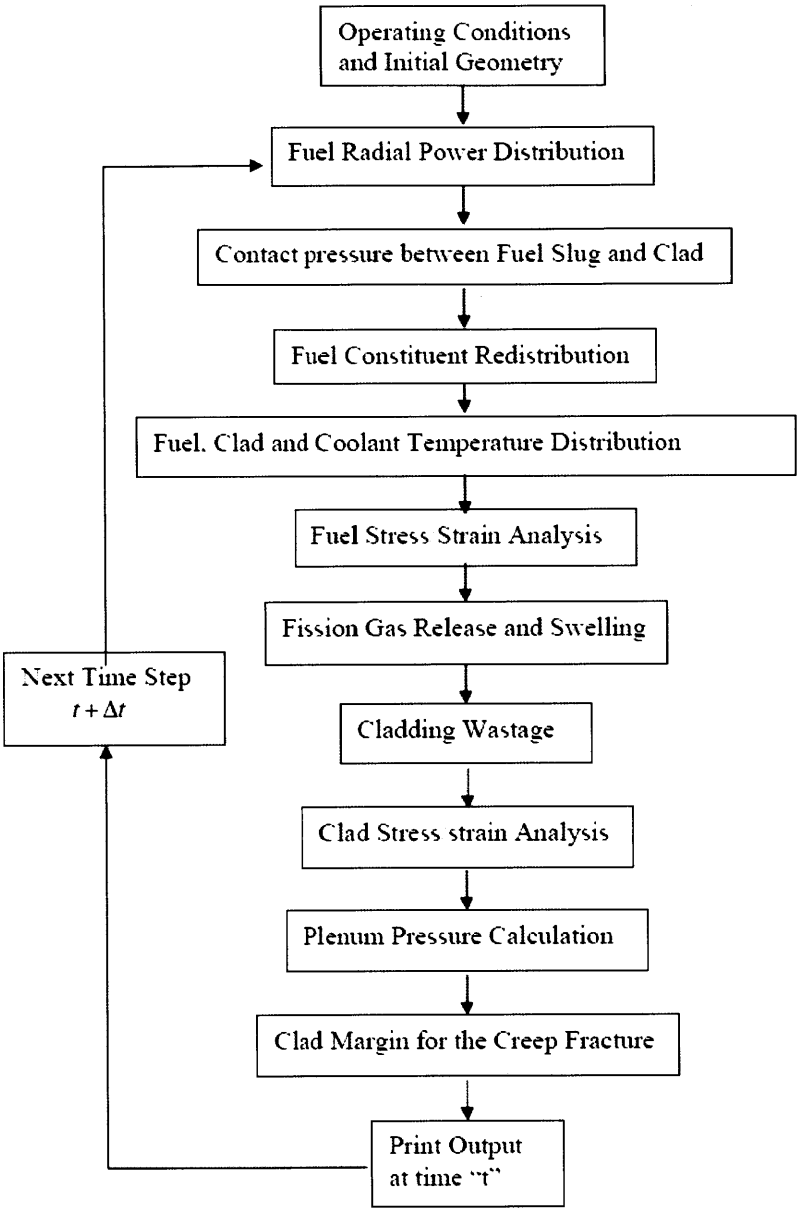

Figure 16: Flow chart of FEAST-METAL [4]

2.2. Fission Gas Release Model

The fission gas release model used in FEAST-METAL is based on the GRSIS algorithm. A schematic of the algorithm can be seen in Figure 17. Initially fission gas atoms are created by fission in the fuel matrix. These atoms nucleate together to form bubbles or diffuse into existing bubbles. The bubbles form uniformly in the fuel, since they are assumed to form on both phase and grain boundaries. The bubbles generated are classified into two groups based upon their size; one group has a radius of 0.5 micron (type 1 bubbles), while the other has a radius of 10 microns (type 2 bubbles). Eventually, these two types of bubbles collide with one another, coalesce and finally diffuse to make contact with the plenum or gap gas. At this point, the bubbles form open pores. These open pore bubbles are assumed to have the same size and shape as normal bubbles. When closed bubbles interact with the open pores they release their gas atoms to the plenum. Additionally a certain fraction of closed bubbles are assumed to form open pores once a swelling threshold is reached by the fuel (10% for FEAST-METAL). While closed bubbles are assumed to be able to diffuse through the fuel matrix, the open pores are immobile since their gas has already been released. [4]

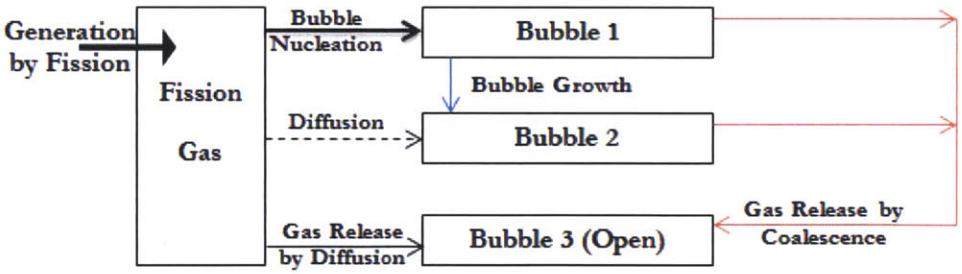

Figure 17: Schematic of the GRSIS-based fission gas and bubble movement model utilized by FEAST-METAL Version 1 [17]

2.2.1. Governing Equations

The GRSIS model uses constant bubble radii, as opposed to ALFUS, which adopted a constant atom number per bubble approach. In the basic GRSIS algorithm upon which the first version of FEAST-METAL is based, two closed bubble groups are used and one open bubble group. The governing equations for the gas atoms and bubble groups are: [4]

$$\frac{dC_g}{dt} = YF - (J_{g1} + J_{g2} + J_{g3}) - J_{b_1,nucl} \qquad \text{Eqn. 17}$$

$$\frac{dC_{gb1}}{dt} = J_{b_1,nucl} + J_{g1} - (ab_{12} + ab_{13}) - (gab_{12} + gab_{21} + gab_{13}) - f_{12}(ab_{11} + gab_{11}) - I_1 \qquad \text{Eqn. 18}$$

$$\frac{dC_{gb2}}{dt} = J_{g2} + ab_{12} + gab_{12} + gab_{21} + f_{12}(ab_{11} + gab_{11}) - ab_{23} - gab_{23} - I_2 \qquad \text{Eqn. 19}$$

$$\frac{dC_{gb3}}{dt} = J_{g3} + ab_{13} + ab_{23} + gab_{13} + gab_{23} + I_1 + I_2 \qquad \text{Eqn. 20}$$

C_g: Gas atom concentration in the fuel matrix (atoms/m^3)

C_{gb1}: Concentration of gas atoms present as bubble-1 (closed, small) in the matrix (atoms/m^3)

C_{gb2}: Concentration of gas atoms present as bubble-2 (closed, large) in the matrix (atoms/m^3)

C_{gb3}: Concentration of gas atoms present as bubble-3 (open) in the matrix (atoms/m^3)

Y: Fission yield of gas atoms (0.25 atoms/fission)

F: Fission Density (fissions/s/m^3)

I_i: Instantaneous release by bubble interconnection at threshold for closed bubble swelling, for bubble-i

$J_{b1,nucl}$: Bubble-1 nucleation rate (atoms/s/m^3)

J_{gi}: Gas diffusion rate to bubble-i (atoms/s/m^3)

ab_{ij}: Transfer rate of bubble-i into bubble-j by bubble diffusion (atoms/s/m^3)

gab_{ij}: Transfer rate of bubble-i into bubble-j by radial growth of bubble-i (atoms/s/m^3)

$f_{i,i+1}$: Transition probability of bubble-i into bubble-i+1 by collision with bubble

Bubble density (N_{bi}) and the gas atom density of bubble-i (C_{gbi}) can also be expressed as follows. [4]

$$C_{gbi} = \rho_{g1} N_{bi} \qquad \textbf{Eqn. 21}$$

ρ_{gi}: Number of gas atoms in bubble-i (atoms/bubble)

N_{bi}: The concentration of bubble-i (bubble/m^3)

The gas density can be defined according to the following equation, making use of a Van der Waals Parameter: [4]

$$\rho_{gi} = \left(B + \left(\left(\frac{2\gamma}{kT} \right) \frac{1}{R_i} + \frac{\sigma_h}{kT} \right)^{-1} \right)^{-1} \times V_{bi} \qquad \textbf{Eqn. 22}$$

B: Van der Waals parameter (85×10^{-30} m^3/atom)

γ: Surface tension (8 N/m)

R_i: Radius of bubble-i (m)

σ_h: Hydrostatic stress (Pa)

k: Boltzmann constant (1.381×10^{-23} J/K)

V_{bi}: Volume of bubble-i (m^3)

The hydrostatic stress can then be expressed as follows, where σ_i is the stress in the direction i: [4]

$$\sigma_h = -\frac{\sigma_r + \sigma_\theta + \sigma_z}{3} \qquad \textbf{Eqn. 23}$$

Since the open pores are formed from both large and small bubbles the open pore transfer rate equations can be rewritten in the following manner: [4]

$$ab_{i3} = ab_{i31} + ab_{i32} \qquad \textbf{Eqn. 24}$$

$$gab_{i3} = gab_{i31} + gab_{i32} \qquad \textbf{Eqn. 25}$$

The closed bubble group is denoted by i (either 1-small or 2-large), while the open pores are denoted by 31 for small pores and 32 for large pores. For example, ab_{232} refers to transfer from small bubbles to small open pores

This leads to two more balance equations that can be used for large and small open pores: [4]

$$\frac{dC_{gb31}}{dt} = \rho_{g1}\frac{d}{dt}N_{b31} = ab_{131} + ab_{132} + gab_{131} + gab_{132} \qquad \text{Eqn. 26}$$

$$\frac{dC_{gb32}}{dt} = \rho_{g2}\frac{d}{dt}N_{b32} = ab_{231} + ab_{232} + gab_{231} + gab_{232} \qquad \text{Eqn. 27}$$

At the end of a time step, the results of the rate of change calculations seen in Equation 26 and 27are multiplied by the change in time to find the increase in the change in bubble concentration over a given time-step. [4]

$$\Delta C_{gbi} = \frac{dC_{gbi}}{dt} \cdot dt \qquad \text{Eqn. 28}$$

This change in concentration is then used to find the change in the number of bubbles of a given type over a given time-step in the code. [4]

2.2.2. Bubble-1 Nucleation Rate

The bubble-1 nucleation rate ($J_{b1,nucl}$) is determined from the bubble nucleation constant and the concentration of gas atoms in the fuel matrix: [4]

$$J_{b1,nucl} = k_{b1,nucl} C_g \rho_{g1} \qquad \text{Eqn. 29}$$

$k_{b1,nucl}$: Bubble-1nucleation constant (bubble/s/atom)

2.2.3. Gas Diffusion

In the GRSIS model, the diffusion rate of gas atoms into bubbles is calculated from the assumption that the gas atoms are diffusing into a spherical sink (bubble), from which they cannot escape. Therefore, the atom flux of gas into bubble-i through diffusion (J_{gi}) can be calculated as a function of the rate of gas diffusion and the concentrations of gas and bubbles. [4]

$$\boldsymbol{J_{gi} = k_{gi} C_g N_{bi}} \qquad \textbf{Eqn. 30}$$

$$\boldsymbol{k_{gi} = E_{gbi}(4\pi r_{bi}) D_g} \qquad \textbf{Eqn. 31}$$

k_{gi}: Gas diffusion constant to bubble-i (m^3/s)

E_{gbi}: Empirical bias factor for gas diffusion to bubble-i

r_{bi}: Radius of bubble-i (m)

D_g: Diffusion coefficient of gas atom (m^2/s)

The diffusion coefficient can then be expressed as follows, where the diffusion constant (D_{g0}) is a fitting factor: [4]

$$\boldsymbol{D_g = D_{g0} \exp\left(-\frac{Q_g}{RT}\right)} \qquad \textbf{Eqn. 32}$$

D_{g0}: Diffusion constant (m^2/s)

Q_g: Activation energy for a mole of jumps (52000 cal/g-mol)

R: Gas constant (1.987 cal/g-mol/K)

T: Temperature of the fuel (K)

2.2.4. Coalescence by Bubble Diffusion

First, a bubble diffusion coefficient (D_{bi}) needs to be defined. This is calculated based on the surface diffusion coefficient (D_s), which is in turn related to the gas diffusion coefficient (D_g). [4]

$$D_{bi} = \frac{3a_0^2}{2\pi r_{bi}^4} D_s \qquad \textbf{Eqn. 33}$$

$$D_s = 1000 D_g \qquad \textbf{Eqn. 34}$$

D_{bi}: Diffusion coefficient of bubble-i (m^2/s)

a_0^4: Area occupied by a gas atom at the bubble surface (m^2)

D_s: Surface diffusion coefficient (m^2/s)

The rate of bubble-i/bubble-j collisions caused by diffusion movement is dependent on the collision constant (k_{ij}), which is calculated according to Equation 35. [4]

$$k_{ij} = E_{bb} 4\pi (r_{bi} + r_{bj})(D_{bi} + D_{bj}) \qquad \textbf{Eqn. 35}$$

E_{bb}: Empirical bias factor for bubble diffusion to other bubbles

k_{ij}: Collision constant of bubble-i into bubble-j (m^3/s)

From this, the total transfer rate via diffusion of bubble-i to bubble-j can be found. It is dependent on the collision constant (k_{ij}), the number of atoms in bubble-i (ρ_{gi}) and the concentration of both bubble-i and bubble-j (N_{bi}, N_{bj}). [4]

$$ab_{ij} = k_{ij} N_{bi} N_{bj} \rho_{gi} \qquad \textbf{Eqn. 36}$$

Also, the transition rate of bubble-i to bubble-i+1 after a collision between two bubble-i (ab_{ii}) can be expressed as follows: [4]

$$ab_{ii} = k_{ii} N_{bi}^2 2\rho_{gi} \qquad \textbf{Eqn. 37}$$

Finally, if two bubbles of the same group coalesce, then the probability of those bubbles transforming into a larger bubble is given by a mass balance. [4]

$$f_{i,i+1} = \frac{2\rho_{gi}}{\rho_{gi+1}} \qquad \textbf{Eqn. 38}$$

2.2.5. Coalescence by Bubble Growth

If the assumption is made that all of the bubble-i 's are distributed homogenously in an FCC matrix in the fuel, then the average distance (l_{ij} in meters) between two bubbles of the same type can be found using the following equation. [4]

$$l_j = 1.122 N_{bj}^{-1/3} \qquad \textbf{Eqn. 39}$$

l_j: Average distance between the centers of bubble-j (m)

Assuming that bubbles of type-i are randomly distributed in this FCC-matrix of j-type bubbles, the average distance between the bubbles becomes $0.5\ l_j$. This was calculated using a Monte Carlo algorithm. The original GRSIS model used $0.25\ l_j$ based on a 2D calculation. From this, the probability per unit time of bubble-i colliding with bubble-j due to radial growth (P_{ij}) can be expressed by the following equation when both bubbles are closed. [4]

$$\boldsymbol{P_{ij}} = \frac{\text{radial growth of bubble-i}}{\text{distance between the surfaces of bubble-i and j}} = \frac{\boldsymbol{\Delta r_{bi}}}{\boldsymbol{0.5 l_j - (r_{bi} + r_{bj})}} \qquad \textbf{Eqn. 40}$$

P_{ij}: Probability per unit time of bubble-i colliding with bubble-j due to radial growth (#/s)

Δr_{bi}: Rate of change of the radius of bubble-i (m/s)

When one of the two bubbles is a stationary open pore, then the probability of collision changes to include a fitting factor (d_l) since spacing of open porosity cannot easily be characterized. [4]

$$\boldsymbol{P_{ij}} = \frac{\boldsymbol{\Delta r_{bi}}}{\boldsymbol{d_l l_j}} \qquad \textbf{Eqn. 41}$$

d_l: Open bubble formation coefficient (fitting factor)

The rate of change of the volume of bubble-i can be written as a function of the influx or outflux of atoms and the concentration of gas bubbles. This can then be adapted to the bubble radius. [4]

$$\Delta V_{bi} = \frac{J_{gbi}}{C_{gbi}} V_{bi} \qquad \text{Eqn. 42}$$

$$\Delta r_{bi} = \frac{\Delta V_{bi}}{4\pi r_{bi}^2} = \frac{J_{gbi} r_{bi}}{3 C_{gbi}} \qquad \text{Eqn. 43}$$

Using this probability, the collision rate between bubble-i with bubble-j can be found for the case of radial growth (gab_{ij}). Here the factor "k" is the minimum of "i" and "j". [4]

$$gab_{ij} = P_{ij} C_{gbk} \qquad \text{Eqn. 44}$$

When two bubbles of the same type collide, there is a probability that they will form a larger bubble. This probability is dictated by the mass balance. It is the same as the probability as for growth by diffusion. [4]

$$f_{i,i+1} = \frac{2\rho_{gi}}{\rho_{gi+1}} \qquad \text{Eqn. 45}$$

2.2.6. Swelling

In the FEAST-METAL code, there are three sources of fuel swelling. The first it closed bubbles swelling. The second is open pore swelling, which is related to the fission gas release. The third is solid fission product swelling. The swelling volume of closed bubbles (S_c) can be expressed as the total volume taken up by both type 1 and type 2 bubbles. [4]

$$S_c = V_1 + V_2 \qquad \text{Eqn. 46}$$

$$V_i = \frac{4}{3}\pi r_{bi}^3 N_{bi} \qquad \text{Eqn. 47}$$

When a swelling threshold is reached by the fuel, some of the closed pores become instantaneously open and release their contents into the plenum. This fraction is expressed by the factor "f_{th}". In FEAST-METAL, the swelling threshold is 20%. After the threshold is reached, two fitting factors are applied to the open pores. One corrects for volume, the other for surface area. This leads to the following equations, once the threshold has been reached. The open pores contribute to open porosity swelling (S_0). [4]

$$V_i \rightarrow (1 - f_{th})V_i \qquad i = 1,2 \qquad \text{Eqn. 48}$$

$$V_3 = f_{th} f_v (V_1 + V_2) \qquad \text{Eqn. 49}$$

$$S_O = V_3 \qquad \text{Eqn. 50}$$

$$A_i \rightarrow (1 - f_{th})A_i \qquad i = 1,2 \qquad \text{Eqn. 51}$$

$$A_3 = f_{th} f_s (A_1 + A_2) \qquad \text{Eqn. 52}$$

f_{th}: Fraction of closed bubbles that interconnect when swelling threshold is reached

f_s: Fractional surface area of a closed bubble after interconnection with open bubbles

f_v: Fractional volume of a closed bubble after interconnection with open bubbles

Solid fission product swelling is considered to increase linearly with burn-up at a rate of 1.2-1.5% per at%. Originally the value was set to 1.5%, then in newer versions of the code this rate was changed to 1.2% per at% burnup after a reexamination of the experimental data. Combining these three sources of swelling, the total swelling, without hot pressing, becomes: [4]

$$S_T = S_c + S_O + S_{SFP} = V_1 + V_2 + V_3 + .015 \times Bu \qquad \text{Eqn. 53}$$

2.2.7. Fission Gas Release

From this, the fission gas release can be calculated. There are three separate regimes based on the amount of swelling that is present in the fuel. [4]

$$FGR = \begin{cases} 0 & S_g < S_{th} \\ f_{th}(C_{gb1} + C_{gb2}) & S_g = S_{th} \\ C_{gb3} & S_g > S_{th} \end{cases} \qquad \text{Eqn. 54}$$

2.3. Fuel Creep and Plasticity

The effective permanent strain ($\epsilon_i \quad i = r, \theta, z$) in the fuel is seen to be a result of the sum of creep, both irradiation and thermal, and plastic strains. Since the creep and plastic deformations occur at a constant volume, the radial, azimuthal and axial components of the strain must sum to zero. [4]

$$\epsilon_i = \epsilon_i^{creep} + \epsilon_i^{plastic} \qquad \text{Eqn. 55}$$

$$\epsilon_r + \epsilon_\theta + \epsilon_z = 0 \qquad \text{Eqn. 56}$$

ϵ_i : Effective permanent strain in direction i (mm/mm)

ϵ_r : Permanent strain in the radial direction (mm/mm)

ϵ_θ : Permanent circumferential strain (hoop strain) (mm/mm)

ϵ_z : Permanent strain along z-axis (mm/mm)

The calculation of these three permanent strain components is based on the von Mises assumption, where creep and plastic deformations occur only when the stress state varies from pure hydrostatic compression or tension. This leads to the following stress-strain relations, which are known as the Prandtl-Reuss flow laws or the Soderberg equations. [4]

$$\Delta\epsilon_r = \left(\frac{\epsilon_{eq}}{\sigma_{eq}}\right)\left(\sigma_r - \frac{1}{2}(\sigma_\theta + \sigma_z)\right) \qquad \text{Eqn. 57}$$

$$\Delta\epsilon_\theta = \left(\frac{\epsilon_{eq}}{\sigma_{eq}}\right)\left(\sigma_\theta - \frac{1}{2}(\sigma_r + \sigma_z)\right) \qquad \text{Eqn. 58}$$

$$\Delta\epsilon_z = \left(\frac{\epsilon_{eq}}{\sigma_{eq}}\right)\left(\sigma_z - \frac{1}{2}(\sigma_\theta + \sigma_r)\right) \qquad \text{Eqn. 59}$$

σ_{eq}: Equivalent stress for porous fuel (Pa)

The expression for the equivalent stress is taken from the model used in ALFUS. [4]

$$\sigma_{eq} = \left(\frac{1}{2}\left((\sigma_r - \sigma_\theta)^2 + (\sigma_\theta - \sigma_z)^2 + (\sigma_z - \sigma_r)^2\right) + 3\alpha_c\left(\sigma_r + \sigma_\theta + \sigma_z + 3P_p\right)^2\right)^{.5} \qquad \text{Eqn. 60}$$

α_c: Open pore compressibility factor

P_p: Plenum pressure (Pa)

Here the net effective hydrostatic stress applied to the fuel is $(\sigma_r + \sigma_\theta + \sigma_z + 3P_p)$. The gas plenum pressure is equal to the internal pressure of the open pores necessarily. Additionally the factor α_c is the open pore compressibility factor. [4] It is based on experimental data for hot isostatic pressing at high temperature single gamma phase. [18] The model itself was developed by Ogata et al. for pore compression in creep dependent form. [19] Additionally, in the cladding region this factor is zero.

$$\alpha_c = \begin{cases} 0 & \epsilon_{sw}^{opn} = 0 \\ \frac{1}{6}\left(\epsilon_{sw}^{opn}\right)^{1.5} & 0 < \epsilon_{sw}^{opn} < .1 \\ \frac{1}{6} & .1 > \epsilon_{sw}^{opn} \end{cases} \qquad \text{Eqn. 61}$$

ϵ_{sw}^{opn}: Open pore swelling (fraction)

The creep strain rate for the fuel can be found using the following equations. Once found, it is used to calculate the total creep over the code-inputted time step. [4]

$$\dot{\epsilon_{eq}} = \begin{cases} \left(5 \times 10_{eq}^{3}\sigma_{eq} + 6 \times \sigma_{eq}^{4.5}\right) \times \exp\left(-\frac{26170}{T}\right) & T < 923.15\ K \\ \left(.08 \times \sigma_{eq}^{3}\right) \times \exp\left(-\frac{14350}{T}\right) & T \geq 923.15\ K \end{cases} \qquad \text{Eqn. 62}$$

$\dot{\epsilon_{eq}}$: Equivalent creep strain rate (1/s)

σ_{eq}: Equivalent stress (MPa)

This model assumes "perfect plasticity." So if the yield stress is exceeded, then the fuel will increase its strain rate such that the stress on the fuel remains at the yield stress level. It is unlikely for the fuel to be in the $> \sigma_y$ region for extended periods of time during steady state operation due to effectiveness of fuel creep in stress relaxation. [4]

2.4. Fuel Swelling

In FEAST-METAL the fuel swelling strain (ϵ^S) is calculated through the following equation.

$$\epsilon^S = \frac{1}{3}\left(\left(\frac{\Delta V}{V}\right)_{Solid\ FP} + \left(\frac{\Delta V}{V}\right)_{Closed\ Bubble} + \left(\frac{\Delta V}{V}\right)_{Open\ Porosity} - \left(\frac{\Delta V}{V}\right)_{Hot\ Pressing}\right) \quad \textbf{Eqn. 63}$$

The values of these three gas related terms are calculated using the results of the fission gas release module. The solid fission product swelling term is found based on an empirical relation assuming there is 1.5% swelling every 1 at% of burn-up. Closed and open porosity swelling is taken directly from the fission gas module. Decrease in the volume of bubbles due to hot isostatic pressing is based on the open pore compressibility factor (α_c) and is found using the following equation. [4]

$$\Delta\epsilon_{HIP} = 9\alpha_c(\sigma_r + \sigma_\theta + \sigma_z + 3P_p)\left(\frac{\Delta\epsilon_{eq}}{\sigma_{eq}}\right) \quad \textbf{Eqn. 64}$$

$\Delta\epsilon_{HIP}$: Swelling due to hot isostatic pressing

This is incorporated into the code as a modification on the number of bubbles in a given open pore group. Because $\Delta\epsilon_{HIP}$is calculated at each time step, the change in the number of bubbles due to pressing is expressed as follows: [4]

$$N_{bi,t} = N_{bi,t-1} \times (1 + \Delta\epsilon_{HIP}) \quad \textbf{Eqn. 65}$$

$N_{bi,t}$: The concentration of bubble-i (bubble/m^3) at time-step-t

2.5. Phase Boundary Model

Normally in a ternary system a three-sided phase diagram is used to determine the phase of the fuel. However, since the Pu concentration of the fuel can be approximated as a constant value, FEAST-METAL simplifies the ternary U-Pu-Zr system to a binary one. The ternary diagram can be seen in Figure 4, while the binary one is in Figure 5. The pseudo-binary diagram can be seen in Figure 18. [4]

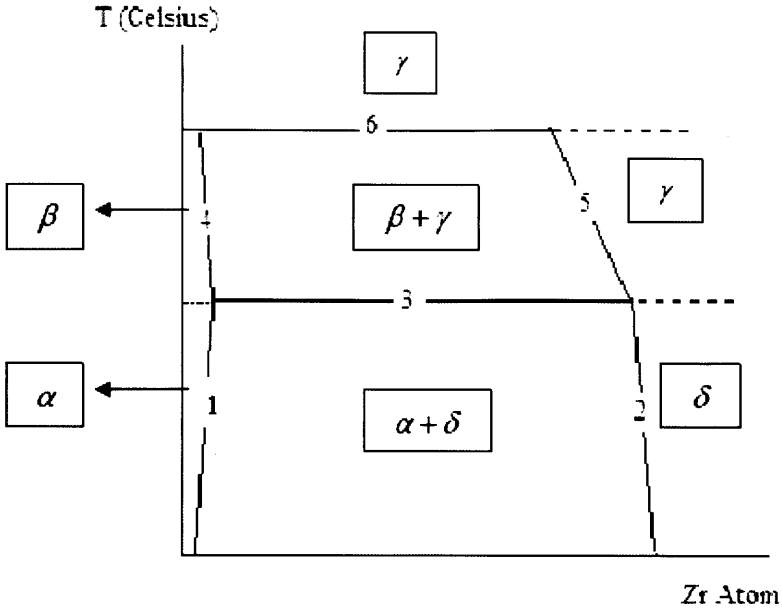

Figure 18: Pseudo-binary phase diagram for U-Pu-Zr fuel for a fixed Pu content. [4]

After the phase diagram is simplified, the transition temperatures between phases can be approximated linearly based on Pu concentration. The six lines of the binary diagram are fully described in Karahan's Ph.D. Thesis. [4] For the X-425 and X-430 benchmark cases, which are U-19Pu-10Zr, the transition temperatures are 583 °C and 642 °C.

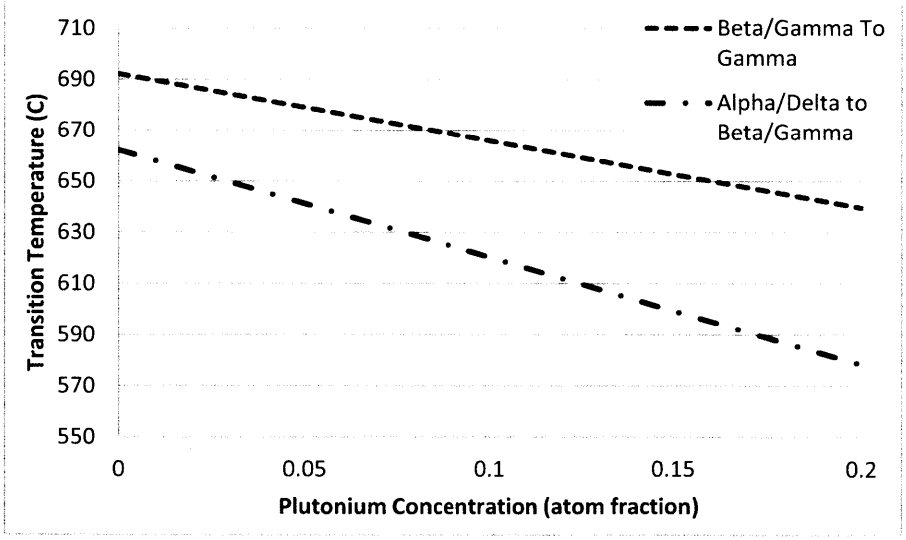

Figure 19: Transition temperatures currently used in FEAST-METAL

2.6. Anisotropic Fuel Deformation

Once the metallic fuel slug comes into contact with the cladding it becomes axially restrained. Before this restraint occurs, fuel slug swelling is anisotropic. In ternary fuel, this is due to large cracks that occur radially on phase or grain boundaries. In binary fuel, this is primarily due to the irradiation growth of α-U crystals. To represent these effects well, an empirical model is used. The model is based on the one employed in the code ALFUS. This model defines the effective radius of the fuel in the following manner. [4]

$$\boldsymbol{r_{eff} = r_0 + dr_{slug} + dr_{crack} = r_{slug} + dr_{crack}} \qquad \textbf{Eqn. 66}$$

r_{eff}: Effective fuel radius

r_0: Initial fuel radius

dr_{slug}: Radial strain due to thermal expansion, elasticity, creep/plasticity and swelling

dr_{crack}: Radial strain due to cracks forming within the fuel

r_{slug}: Radius of the slug (computed in the rest of FEAST)

Using this method prevents the FCMI from growing too rapidly. FCMI does not rapidly build-up because the closed and open pores in the fuel are gradually sintered. Therefore, using this model the interaction between the cladding and the fuel can be broken into three different intervals: [4]

(1) $r_{eff} < r_i$: no contact between clad and fuel

(2) $r_{slug} < r_i = r_{eff}$: axial restraint but no radial restraint

(3) $r_i = r_{slug}$: both axial and radial restraint by cladding

Where r_i = inner cladding radius.

Additionally the radial strain due to crack formation is described in the following manner: [4]

$$\boldsymbol{dr_{crack} = f_{crack} \times r_0^{gap}} \qquad \textbf{Eqn. 67}$$

f_{crack}: Empirically based fitting factor for fuel anisotropy

r_0^{gap}: Initial gap radius

The determination of the anisotropy factor is based on experimental results and is a function of the plutonium content of the slug as well as linear power. [4] Figure 20 shows the value of this factor for Version 1 of FEAST-METAL.

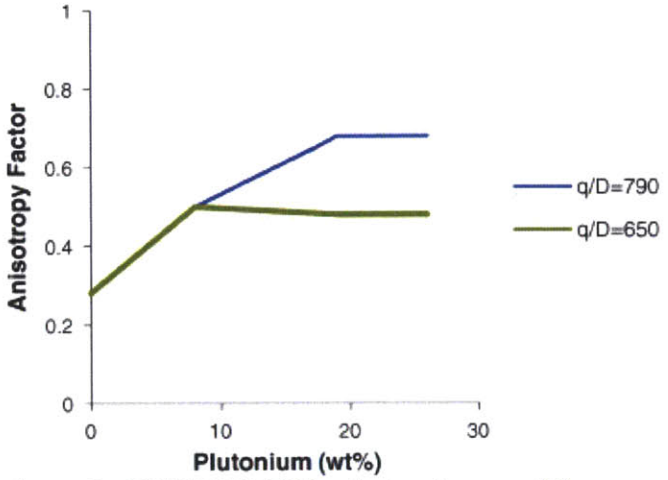

Figure 20: Anisotropy factor for FEAST-METAL v. 1, showing two different power densities (q/D is expressed in terms of W/cm²) [16]

3. Description of Updates to Models

The work presented in this thesis focused on performing four major updates to the fission gas and swelling modules of the FEAST-METAL code. These updates were then benchmarked against fuel irradiation data from EBR-II. The first study performed examined the sensitivity of the code to the number of closed bubble groups. The original model, which used two closed groups, was extended to three and four groups. The second study performed altered the code so that radii of bubble groups could change with time. This involved making bubble size dependent on a constant number of atoms per bubble. The first version had bubbles of constant volume with varying numbers of atoms in each bubble type. This second step sought to bridge some of the gap between the GRSIS algorithm used in FEAST-METAL and the OGRES algorithm used in ALFUS. The third study performed made the size and shape of bubbles dependent on the phases present in the fuel. This follows from the morphological differences in the phases present in ternary fuel. Finally, the logic to determine the spacing of bubbles was examined. The first version of the code approximated the spacing between gas bubbles to be based on an FCC lattice. To derive a better approximation of the spacing a Monte-Carlo algorithm was devised and implemented. After each of these code modifications were developed, they were benchmarked against data from the X-425 and X-430 cases from EBR-II.

This section examines the logic behind the above described four code alterations and how they were implemented in the code. It shows the equations that were developed and implemented in the algorithms of the code. It also provides information on the fitting factors that were used to benchmark the code. The benchmark was performed to match fission gas release and total cladding strain to experimental results. To benchmark the code, four main fitting factors were used. The first was the diffusion rate of gas through the fuel. The second factor altered the rate of open pore formation from closed bubbles. The third altered surface area calculations made on gas bubbles. The fourth altered the compressibility of the fuel. This fourth fitting factor was introduced when the fission gas model was changed to a constant atom number approach and was not used beforehand. Modifications to anisotropy factors were also required. Since these are based purely on fitting the results of the code to match experimental results, they were not a factor in benchmarking. The necessary modifications to the code for the modeling of anisotropic deformation were made after

the code was benchmarked against fission gas release and cladding strain. A comparison of the results obtained from running these versions of the code is contained in Chapter 4.

3.1. Dependence of FEAST-METAL on the Number of Closed Bubble Groups

In order to assess the sensitivity of FEAST-METAL to the number of closed bubble groups, the number of bubble groups was altered from two to three and four. This section contains schematics of the new fission gas algorithms and the resultant equations. In this study, the fission bubble groups had constant radii, instead of a constant number of atoms as was the case in later studies. The radii of the smallest and larges bubble groups were kept the same as in the original group. Intermediate groups were chosen so that the ratio of the i-bubble group over the (i-1)-bubble group was roughly the same for all bubbles. The radii can be seen in Table 3 for all of the different groups addressed.

Table 3: Radii of bubble groups used (microns) [16]

	2-Group	3-Group	4-Group
Radius-1	0.5	0.5	0.5
Radius-2	10	2.5	1.35
Radius-3	-	10	3.67
Radius-4	-	-	10

The fitting factors used to benchmark the code for these versions were the fission gas diffusion constant, the open bubble formation constant and the surface area correction factor. The relation of these three factors to the rest of the code can be seen Equations 34, 41 and 52. For each of these there is a very small range of viability and small alterations percentage-wise can have a large impact on the results that the code returns. The surface area correction factor was kept the same from the original version of the code and fuel compressibility was not altered.

Table 4: Fitting factor in multi-group versions of FEAST-METAL [16]

Code	Diffusion Constant	Open Bubble Formation Coefficient	Surface Area Correction Factor
2-Group	2.70E-03	0.24	0.2
3-Group	1.75E-03	0.246	0.2
4-Group	3.00E-03	0.3109	0.2

The majority of the original fission gas and swelling modules in FEAST-METAL were not directly altered by expanding the model to more bubble group. This section focuses only on the portions of the code that were altered. The entire fission gas and swelling algorithms are discussed in the previous chapter. Along the same line, the two closed bubble group method will not be discussed further because it is discussed in the previous chapter. A schematic of the algorithm can be seen in Figure 17. The governing equations can be found in Section 2.2.1.

3.1.1. Three Group Algorithm

The algorithm for three groups is very similar to the two group model, yet the number of interactions between groups significantly increases.

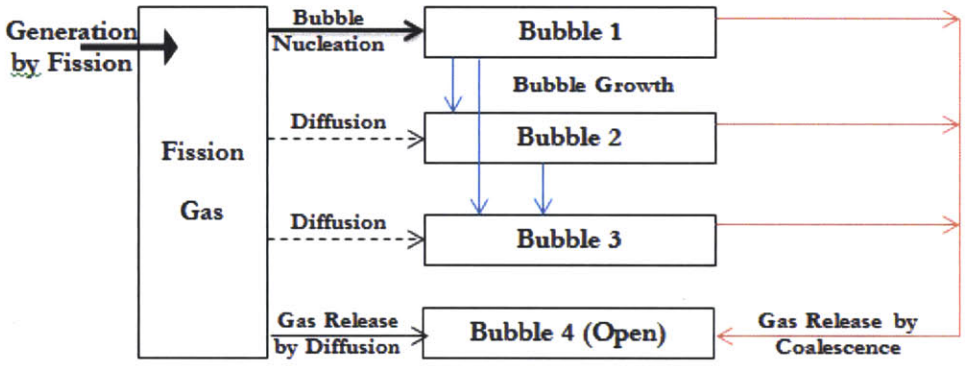

Figure 21: Fission gas algorithm for three closed bubble groups

Following this algorithm, the governing equations can be developed. They are similar in structure to Equations 18, 19 and 20 in the previous chapter, but they contain more terms to account for interactions with the additional bubble group. Each time a group is added, as will best be seen in the four group example, the complexity and therefore the computer runtime becomes much higher.

$$\frac{dC_g}{dt} = YF - (J_{g1} + J_{g2} + J_{g3} + J_{g4}) - J_{b_1,nucl} \qquad \text{Eqn. 68}$$

$$\frac{dC_{gb1}}{dt} = J_{b_1,nucl} + J_{g1} - (ab_{12} + ab_{13} + ab_{14}) - (gab_{12} + gab_{21} + gab_{13} + gab_{31} + gab_{14}) - f_{12}(ab_{11} + gab_{11}) - I_1 \qquad \text{Eqn. 69}$$

$$\frac{dC_{gb2}}{dt} = J_{g2} + (ab_{12} + gab_{12} + gab_{21}) + f_{12}(ab_{11} + gab_{11}) - f_{23}(ab_{22} + gab_{22}) - (ab_{23} + ab_{24}) - (gab_{23} + gab_{32} + gab_{24}) - I_2 \quad \text{Eqn. 70}$$

$$\frac{dC_{gb3}}{dt} = J_{g3} + (ab_{13} + ab_{23} + gab_{13} + gab_{23} + gab_{31} + gab_{32}) + f_{23}(ab_{22} + gab_{22}) - ab_{34} - gab_{34} - I_3 \quad \text{Eqn. 71}$$

$$\frac{dC_{gb4}}{dt} = J_{g4} + (ab_{14} + ab_{24} + ab_{34}) + (gab_{14} + gab_{24} + gab_{34}) + I_1 + I_2 + I_3 \quad \text{Eqn. 72}$$

C_g: Gas atom concentration in the fuel matrix (atoms/m3)

C_{gb1}: Concentration of gas atoms present as bubble-1 (closed) in the matrix (atoms/m^3)

C_{gb2}: Concentration of gas atoms present as bubble-2 (closed) in the matrix (atoms/m^3)

C_{gb3}: Concentration of gas atoms present as bubble-3 (closed) in the matrix (atoms/m^3)

C_{gb5}: Concentration of gas atoms present as bubble-4 (open) in the matrix (atoms/m^3)

Y: Fission yield of gas atoms (0.25 atoms/fission)

F: Fission Density (fissions/s/m^3)

I: Instantaneous release by bubble interconnection at threshold closed bubble swelling

$J_{b1,nucl}$: Bubble-1 nucleation rate (atoms/s/m^3)

J_{gi}: Gas diffusion rate to bubble-i (atoms/s/m^3)

ab_{ij}: Transfer rate of bubble-i into bubble-j by bubble diffusion (atoms/s/m^3)

gab_{ij}: Transfer rate of bubble-i into bubble-j by radial growth of bubble-i (atoms/s/m^3)

$f_{i,i+1}$: Transition probability of bubble-i into bubble-i+1 by collision with bubble

The density, closed bubble concentration and hydrostatic stress can are calculated in the same way as in the 2-group method. Since the open pores are formed now from three groups, the open pore transfer rate equations are rewritten in the following manner:

$$ab_{i4} = ab_{i41} + ab_{i42} + ab_{i43} \quad \text{Eqn. 73}$$

$$gab_{i4} = gab_{i41} + gab_{i42} + gab_{i43} \quad \text{Eqn. 74}$$

This leads to three more balance equations that can be used for open pores:

$$\frac{dC_{gb41}}{dt} = \rho_{g1}\frac{d}{dt}N_{b41} = ab_{141} + ab_{142} + ab_{143} + gab_{141} + gab_{142} + gab_{143} \quad \text{Eqn. 75}$$

$$\frac{dC_{gb42}}{dt} = \rho_{g2}\frac{d}{dt}N_{b42} = ab_{241} + ab_{242} + ab_{243} + gab_{241} + gab_{242} + gab_{243} \quad \text{Eqn. 76}$$

$$\frac{dC_{gb43}}{dt} = \rho_{g3}\frac{d}{dt}N_{b43} = ab_{341} + ab_{342} + ab_{343} + gab_{341} + gab_{342} + gab_{343} \quad \text{Eqn. 77}$$

Additionally, the swelling volume of closed bubbles (S_c) now incorporates three types of bubbles. The volume is calculated in the same manner as in the two group method.

$$S_c = V_1 + V_2 + V_3 \quad \text{Eqn. 78}$$

Area and volume correction factors for open bubbles also now need to include the added closed bubble group. In this manner, open porosity swelling "S_o" becomes reliant on the number of closed bubble groups.

$$V_i \rightarrow (1 - f_{th})V_i \qquad i = 1,2,3 \quad \text{Eqn. 79}$$

$$V_4 = f_{th}f_v(V_1 + V_2 + V_3) \quad \text{Eqn. 80}$$

$$S_O = V_4 \quad \text{Eqn. 81}$$

$$A_i \rightarrow (1 - f_{th})A_i \qquad i = 1,2,3 \quad \text{Eqn. 82}$$

$$A_4 = f_{th}f_s(A_1 + A_2 + A_3) \quad \text{Eqn. 83}$$

f_{th}: Fraction of closed bubbles that interconnect when swelling threshold is reached

f_s: Fractional surface area of a closed bubble after interconnection with open bubbles

f_v: Fractional volume of a closed bubble after interconnection with open bubbles

The total amount of swelling now needs to take into account the added closed bubble groups.

$$S_T = S_c + S_O + S_{SFP} = V_1 + V_2 + V_3 + V_4 + .015 \times Bu \quad \text{Eqn. 84}$$

Fission gas release is calculated in the same manner, but now there are three closed group concentrations to take into account. Like before, there are three separate regimes based on the amount of swelling that is present in the fuel.

$$FGR = \begin{cases} 0 & S_g < S_{th} \\ f_{th}(C_{gb1} + C_{gb2} + C_{gb3}) & S_g = S_{th} \\ C_{gb4} & S_g > S_{th} \end{cases} \quad \text{Eqn. 85}$$

3.1.2. Four Group Algorithm

In the same manner, an algorithm for the four group version of the fission gas module can be developed. The overall algorithm can be seen in Figure 22. Once again, because of the increased interactions between bubble groups, the complexity increases; and, therefore the runtime increases. This is especially an issue because for just benchmark cases with seven axial nodes, the runtime is on the order of two hours. More complex cases simulate of 30-40 years and have 20 axial nodes.

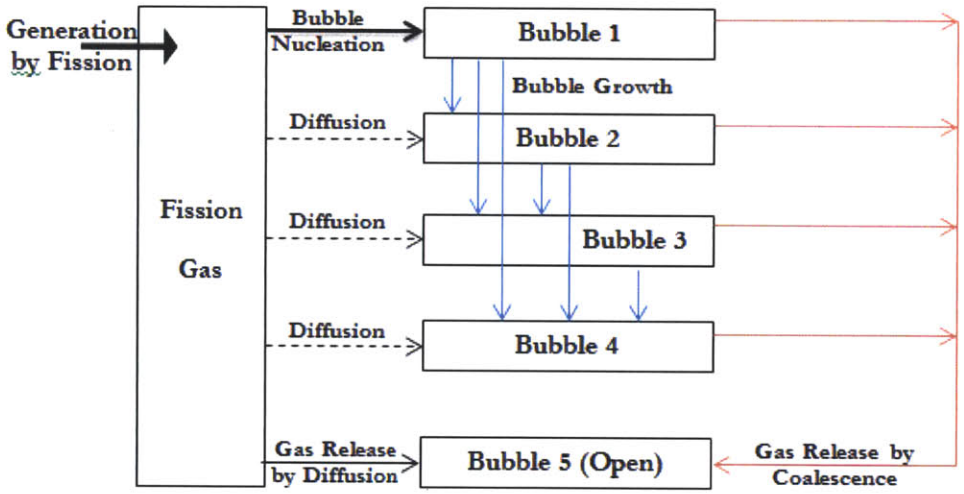

Figure 22: Fission gas algorithm for four closed bubble groups

Once again, the governing equations can be developed. They are as follows:

$$\frac{dC_g}{dt} = YF - (J_{g1} + J_{g2} + J_{g3} + J_{g4} + J_{g5}) - J_{b_1,nucl} \qquad \text{Eqn. 86}$$

$$\frac{dC_{gb1}}{dt} = J_{b_1,nucl} + J_{g1} - (ab_{12} + ab_{13} + ab_{14} + ab_{15}) - (gab_{12} + gab_{21} + gab_{13} + gab_{31} + gab_{14} + gab_{41} + gab_{15}) - f_{12}(ab_{11} + gab_{11}) - I_1 \qquad \text{Eqn. 87}$$

$$\frac{dC_{gb2}}{dt} = J_{g2} + (ab_{12} + gab_{12} + gab_{21}) + f_{12}(ab_{11} + gab_{11}) - f_{23}(ab_{22} + gab_{22}) - (ab_{23} + ab_{24} + ab_{25}) - (gab_{23} + gab_{32} + gab_{24} + gab_{42} + gab_{25}) - I_2 \qquad \text{Eqn. 88}$$

$$\frac{dC_{gb3}}{dt} = J_{g3} + (ab_{13} + ab_{23} + gab_{13} + gab_{23} + gab_{31} + gab_{32}) + f_{23}(ab_{22} + gab_{22}) - f_{34}(ab_{33} + gab_{33}) - (ab_{34} + ab_{35}) - (gab_{34} + gab_{43} + gab_{35}) - I_3 \qquad \text{Eqn. 89}$$

$$\frac{dC_{gb4}}{dt} = J_{g4} + (ab_{14} + ab_{24} + ab_{34} + gab_{14} + gab_{24} + gab_{34} + gab_{41} + gab_{42} + gab_{43}) + f_{34}(ab_{33} + gab_{33}) - ab_{45} - gab_{45} - I_4 \quad \text{Eqn. 90}$$

$$\frac{dC_{gb5}}{dt} = J_{g5} + (ab_{15} + ab_{25} + ab_{35} + ab_{45}) + (gab_{15} + gab_{25} + gab_{35} + gab_{45}) + I_1 + I_2 + I_3 + I_4 \quad \text{Eqn. 91}$$

C_g: Gas atom concentration in the fuel matrix (atoms/m^3)

C_{gb1}: Concentration of gas atoms present as bubble-1 (closed) in the matrix (atoms/m^3)

C_{gb2}: Concentration of gas atoms present as bubble-2 (closed) in the matrix (atoms/m^3)

C_{gb3}: Concentration of gas atoms present as bubble-3 (closed) in the matrix (atoms/m^3)

C_{gb4}: Concentration of gas atoms present as bubble-4 (closed) in the matrix (atoms/m^3)

C_{gb5}: Concentration of gas atoms present as bubble-5 (open) in the matrix (atoms/m^3)

Y: Fission yield of gas atoms (0.25 atoms/fission)

F: Fission Density (fissions/s/m^3)

I: Instantaneous release by bubble interconnection at threshold closed bubble swelling

$J_{b1,nucl}$: Bubble-1 nucleation rate (atoms/s/m^3)

J_{gi}: Gas diffusion rate to bubble-i (atoms/s/m^3)

ab_{ij}: Transfer rate of bubble-i into bubble-j by bubble diffusion (atoms/s/m^3)

gab_{ij}: Transfer rate of bubble-i into bubble-j by radial growth of bubble-i (atoms/s/m^3)

$f_{i,i+1}$: Transition probability of bubble-i into bubble-i+1 by collision with bubble

Since the open pores are formed now from four groups, the open pore transfer rate equations are rewritten in the following manner:

$$ab_{i5} = ab_{i51} + ab_{i52} + ab_{i53} + ab_{i54} \quad \text{Eqn. 92}$$

$$gab_{i5} = gab_{i51} + gab_{i52} + gab_{i53} + gab_{i54} \quad \text{Eqn. 93}$$

This leads to four more balance equation that can be used for open pores:

$$\frac{dC_{gb51}}{dt} = \rho_{g1}\frac{d}{dt}N_{b51} = ab_{151} + ab_{152} + ab_{153} + ab_{154} + gab_{151} + gab_{152} + gab_{153} + gab_{154} \quad \text{Eqn. 94}$$

$$\frac{dC_{gb52}}{dt} = \rho_{g2}\frac{d}{dt}N_{b52}$$
$$= ab_{251} + ab_{252} + ab_{253} + ab_{254} + gab_{251} + gab_{252} + gab_{253} + gab_{254}$$
Eqn. 95

$$\frac{dC_{gb53}}{dt} = \rho_{g3}\frac{d}{dt}N_{b53}$$
$$= ab_{351} + ab_{352} + ab_{353} + ab_{354} + gab_{351} + gab_{352} + gab_{353} + gab_{354}$$
Eqn. 96

$$\frac{dC_{gb54}}{dt} = \rho_{g4}\frac{d}{dt}N_{b54}$$
$$= ab_{451} + ab_{452} + ab_{453} + ab_{454} + gab_{451} + gab_{452} + gab_{453} + gab_{454}$$
Eqn. 97

Additionally, the swelling volume of closed bubbles (S_c) now incorporates four closed bubble groups.

$$S_c = V_1 + V_2 + V_3 + V_4$$ Eqn. 98

Area and volume correction factors for open bubbles also now need to include the added closed bubble group.

$$V_i \rightarrow (1 - f_{th})V_i \qquad i = 1,2,3,4$$ Eqn. 99

$$V_5 = f_{th}f_v(V_1 + V_2 + V_3 + V_4)$$ Eqn. 100

$$S_O = V_5$$ Eqn. 101

$$A_i \rightarrow (1 - f_{th})A_i \qquad i = 1,2,3,4$$ Eqn. 102

$$A_4 = f_{th}f_s(A_1 + A_2 + A_3 + A_4)$$ Eqn. 103

f_{th}: Fraction of closed bubbles that interconnect when swelling threshold is reached

f_s: Fractional surface area of a closed bubble after interconnection with open bubbles

f_v: Fractional volume of a closed bubble after interconnection with open bubbles

The total amount of swelling changes in the following manner:

$$S_T = S_c + S_O + S_{SFP} = V_1 + V_2 + V_3 + V_4 + V_5 + 0.015 \times Bu$$ Eqn. 104

Fission gas release is now described as follows:

$$FGR = \begin{cases} 0 & S_g < S_{th} \\ f_{th}(C_{gb1} + C_{gb2} + C_{gb3} + C_{gb4}) & S_g = S_{th} \\ C_{gb5} & S_g > S_{th} \end{cases} \qquad \text{Eqn. 105}$$

3.2. Adoption of a Constant Atom Number Approach to the Modeling of Bubble Groups

Originally, the FEAST-METAL code used a fission gas release model with a fixed volume for bubbles formed. This approach is based on the GRSIS model. There are a set number of bubble groups of varying volumes, which diffuse through the metal matrix and coalesce to form open pores or larger bubbles. This results in fuel swelling and cladding strain. Once a swelling threshold has been reached, open pore formation begins. Then fission gas is released to the plenum through the open pores in the fuel. In this model the number of atoms per bubble changes every time-step. For the two group model, the radius of bubbles is set to 0.5 and 10 microns for the two group version of the code. The number of atoms in a small bubble was set to be 0.75E+08, and the number in a large bubble was set to be 0.2E+12. These numbers are based on the normal operating temperature and pressure in the fuel.

In contrast to this model, the metallic code ALFUS has bubble groups with a constant number of atoms. This results in bubble group radii becoming dependent on a van der Waals relation and not an arbitrary radius. In the constant atom number version of FEAST-METAL, the GRSIS model has been altered to use bubble groups with constant atom numbers, yet the majority of the GRSIS algorithm has remained unaltered.

As in other versions of the code, the data was benchmarked against results from the EBR-II reactor. In order to match the data, a new fitting factor based on the effective open porosity at low temperature had to be introduced. This factor alters the compressibility of open pores. The resultant fitting factors can be seen in Table 5.

Table 5: Fitting factors for 2-group constant atom number version of FEAST-METAL [16]

Code	Diffusion Constant	Open Bubble Formation Coefficient	Surface Area Correction Factor	Effective Porosity Correction
Constant Volume	2.70E-03	0.24	0.2	1
Constant Atom Number	3.50E-03	0.40	0.5	0.3

3.2.1. Constant Atom Number Approach Algorithm

The logic of the implementation of the constant atom number approach is discussed in this section. As was covered in the previous chapter, the number of gas atoms in a bubble can be found using a van der Waals relation. From this relation and the definition of volume, the radius of fission gas bubbles can be found at each time step. Because both bubble volume and the number of atoms per bubble "ρ_{gi}" are dependent on bubble radius, an iterative approach was developed. Figure 23 shows the basic iterative algorithm that was developed.

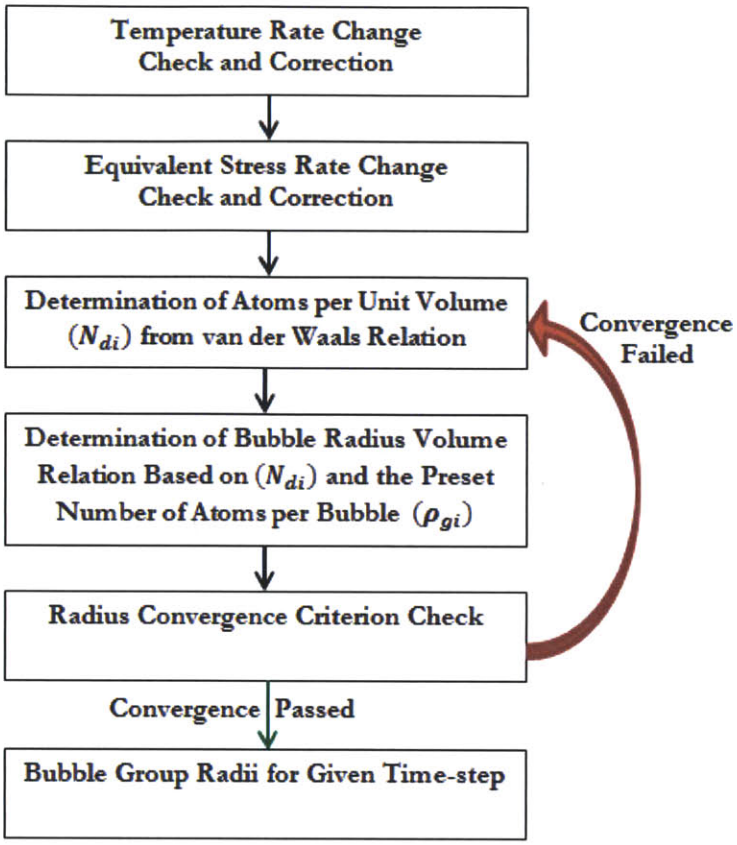

Figure 23: Bubble group radius determination algorithm for the constant atom number version of FEAST-METAL

As can be seen in Equation 106, the van der Waals relation is primarily dependent on temperature and pressure.

$$\rho_{gi} = \left(B + \left(\left(\frac{2\gamma}{kT} \right) \frac{1}{r_i} + \frac{\sigma}{kT} \right)^{-1} \right)^{-1} \times V_{bi} \qquad \text{Eqn. 106}$$

ρ_{gi}: Number of gas atoms in bubble-i (atoms/bubble)

B: van der Waals parameter (85×10^{-30} m^3/atom)

γ: Surface tension (8 N/m)

r_i: Radius of bubble-i (m)

σ: Hydrostatic stress (Pa)

k: Boltzmann constant (1.381×10^{-23} J/K)

V_{bi}: Volume of bubble-i (m^3)

The complex term on the right-hand side of the van der Waals equation can be defined as the density of atoms per unit volume inside a bubble of type-i (N_{di} in units of $\#/m^3$).

$$N_{di} = \left(B + \left(\left(\frac{2\gamma}{kT} \right) \frac{1}{r_i} + \frac{\sigma}{kT} \right)^{-1} \right)^{-1} \quad \textbf{Eqn. 107}$$

The number of gas atoms in the bubble-i equation can be simplified as follows:

$$\rho_{gi} = N_{di} \times V_{bi} \quad \textbf{Eqn. 108}$$

Using definition of volume, we can find the radius of a given bubble:

$$r_{bi} = \sqrt[3]{\left(\frac{3V_{bi}}{4\pi} \right)} \quad \textbf{Eqn. 109}$$

Since:

$$V_{bi} = \frac{\rho_{gi}}{N_{di}} \quad \textbf{Eqn. 110}$$

The radius can be solved in the following manner:

$$r_{bi} = \sqrt[3]{\left(\frac{3\rho_{gi}}{4\pi N_d} \right)} \quad \textbf{Eqn. 111}$$

However, since the term "N_{di}" is also dependent on bubble-i radius, an iterative loop needs to be constructed between Equations 107 and 111. First Equation 107 was evaluated. Then Equation 111 was evaluated. Finally the convergence of bubble radius checked. The convergence criterion was set to be 2.5%, which is a compromise between fidelity and computer runtime. Because this iteration needs to be performed at each time-step for each bubble group, setting the convergence criterion significantly lower drastically increased runtime.

$$\epsilon = \frac{|r_f - r_i|}{r_f} \quad \textbf{while } \epsilon > 0.025 \quad \textbf{Eqn. 112}$$

ϵ: Convergence criteria

r_i: Radius of a gas bubble at the end of iteration

r_f: Radius of a gas bubble at the beginning of iteration

Because the bubble radius changes with time, the numerical stability becomes dependent on the change in radius between two time steps. If the step is too large, then the code will fail artificially. This especially becomes an issue at the beginning of a calculation. Because the code is iterative, an initial guess for fission gas temperature and equivalent stress on bubbles needs to be made. Varying too quickly from this guess causes failure. To compensate for this, constraints were placed on the rate at which fuel temperature and equivalent stress can change. Equivalent stress on the fission gas bubbles was allowed to change at a maximum rate below 50 Pa/s. Fission gas temperature was allowed to change at a maximum rate of 0.1% per second. These constraints were only placed on the fission gas module of the code and did not alter the behavior of any other module directly.

Because, in previous versions of the code, bubbles maintained a constant radius; the average radii of open pores did not change with time. Adopting a model with a varying radius changed this. As a result, the average radius of open pores had to be calculated based on integration over time. That integration is simplified to the following equation, which takes into account the hot isostatic pressing of open pores during the time-step duration.

$$r_{ai} = \frac{r_{i,t-1}N_{bi,t-1}+(N_{bai,t}-N_{bi,t-1})r_i+\Delta\epsilon_{HIP}N_{bi,t-1}r_{i,t-1}}{N_{bai,t}+\Delta\epsilon_{HIP}N_{bi,t-1}} \qquad \textbf{Eqn. 113}$$

$\Delta\epsilon_{HIP}$: Swelling due to hot isostatic pressing

$N_{bi,t}$: The concentration of bubble-i (bubble/m^3) at time-step-t

In the constant atom number approach, the volume taken up by open porosity is dependent upon the phases present in the fuel. This is determined by the temperature of the fuel. So, for temperatures below the alpha to beta transition temperature, for the U-Pu-Zr system, the volume of open porosity is reduced by a significant factor. Since the exact scale of the change was not known, a fitting factor is used to scale the open porosity calculation. So, the new open porosity calculation follows Equation 114. The fitting factor "C" is less than one during the α phase and one during the β and γ phases. This is because, as the temperature decreases, the material anneals and becomes less porous than in the higher temperature phase regions.

$$\alpha_c = \begin{cases} 0 & \epsilon_{sw}^{opn} = 0 \\ C\frac{1}{6}\left(\epsilon_{sw}^{opn}\right)^{1.5} & 0 < \epsilon_{sw}^{opn} < 0.1 \\ \frac{1}{6} & 0.1 > \epsilon_{sw}^{opn} \end{cases} \qquad \text{Eqn. 114}$$

ϵ_{sw}^{opn}: Open pore swelling (fraction)

α_c: Open porosity compressibility factor

C: Effective porosity correction - fitting factor

Since experimental data is not available for the hot pressing behavior of multi-phase fuel it is difficult to make judgments regarding the fidelity of this factor. To date, only high temperature single phase gamma has been examined, not low temperature alpha, beta and zeta phase.

3.3. Modeling Phase Dependent Bubble Morphology

After the code was made to determine fission gas bubble radii based on a constant number of atoms per bubble, the constant atom number version of the code was altered to take into account the different phases present in the fuel. Accounting for different bubble morphologies that result from the phase structure of the fuel makes the code more scientifically based. Figure 3 and Figure 7 in the Introduction chapter show three distinct phase regions within the fuel and the different fission gas bubble morphologies in those regions. However, the identity of these phase regions depends on the initial plutonium concentration of the fuel. To account for this, instead of the actual ternary phase diagram, FEAST-METAL uses a binary phase diagram developed for constant concentrations of plutonium. The phase diagrams can be seen in Figure 4 and Figure 18.

Following this approximation, the morphology of fission gas was determined for the three phase regions present in FEAST-METAL. Morphological structures for the three phase regions are based on experimental results and SEM images showing the$(\alpha + \delta)$, the $(\beta + \gamma)$ and the single-γ phase regions. Differences can be seen most clearly in Figure 24.

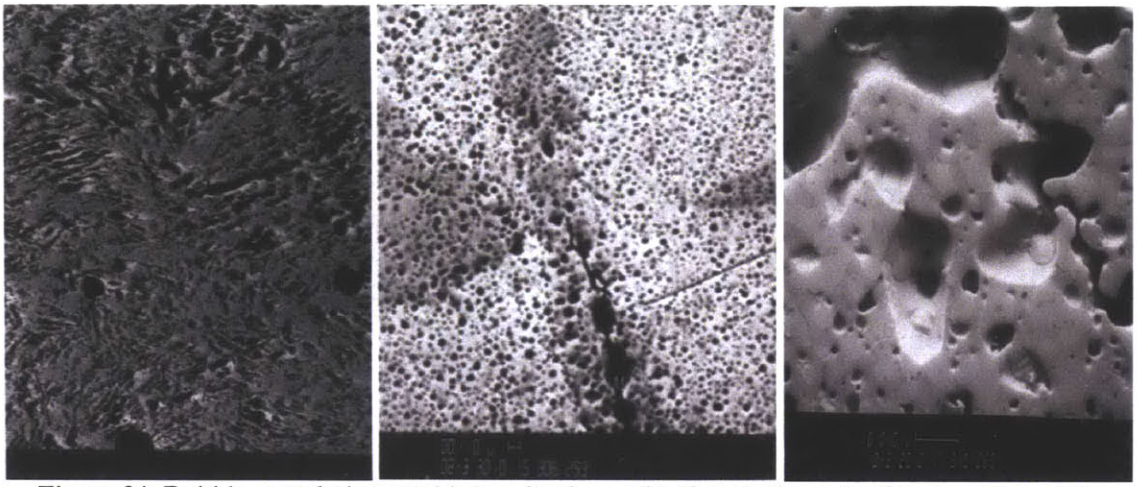

Figure 24: Bubble morphology at (a) (α + δ) phase, (b) (β + γ) phase, (c) Single γ phase [10]

This led the number of atoms in a bubble to be scaled based on representative bubble shapes for each phase region. These representative bubbles and corresponding number of atoms per bubble can be seen in Table 6.

Table 6: Small and large bubble size and number of atoms per bubble

Phase Structure	Small bubble atom number	Small bubble size/shape	Large bubble atom number	Large bubble size/shape
(α + δ)	0.37E+7	~0.2×0.2×0.05 μm Ellipsoidal	0.98E+10	~3.5×3.5×.5 μm Ellipsoidal
(β + γ)	0.20E+7	~0.15 μm Spherical	0.54E+10	~3 μm Spherical
Single γ	0.75E+8	~ 0.5 μm Spherical	0.2E+12	~10 μm Spherical

Accordingly, another benchmark had to be developed. This was done using the four fitting factors discussed in the previous section. Additionally, phase dependence was added to the diffusion coefficient. Measured activation energy of the corresponding phase structure was adopted as given in [20]. The fitting factor now takes on the follow form.

$$D_g = \begin{cases} \mathbf{1.0 \times 10^{-4}} \exp\left(-\frac{5200}{RT}\right) & T < T_\gamma \\ \mathbf{0.3 \times 10^{-8}} \exp\left(-\frac{28500}{RT}\right) & T > T_\gamma \end{cases} \qquad \textbf{Eqn. 115}$$

D_g: Gas diffusion coefficient (m^2/s)

R: Gas constant = 1.987 Cal/mol/K

T: Temperature

T_γ: Single gamma phase transition temperature (K) (The value is 923 K for U-19Pu-10Zr fuel)

Because the van der Waals relation that is used to determine the number of atoms in a unit of volume is dependent on the spherical radius of a bubble, the radius of an equivalent spherical radius needs to be calculated. This is done to conserve the volume of the given bubble. Accordingly, in order to conserve the surface effects of the bubbles, surface area corrections need to be made. Using the sizes of the large ellipsoidal bubbles in Table 6 as an example, the total surface area of an ellipsoidal bubble with those dimensions is 1.95 times larger than the surface area of the surface area of a volume-equivalent spherical bubble. An approximation for the surface area of ellipsoidal bubbles was found as follows.

$$A_s \approx 4\pi \left(\frac{a^p b^p + a^p c^p + b^p c^p}{3}\right)^{\frac{1}{p}} \qquad \textbf{Eqn. 116}$$

A_S: Surface area of an ellipsoid

a, b, c: Ellipsoid radii

p: 1.6075

Also, an angular dependence term needs to be added to account for the external pressure effects because of the ellipsoidal shape. For this study, an angle of 50 degrees was used.

$$N_d = \left(\left[\frac{\sigma}{kT} + \frac{1}{r_i \times 1.95}\left(\frac{2\gamma \times \sin(50)}{kT}\right)\right]^{-1} + B\right)^{-1} \qquad \textbf{Eqn. 117}$$

Additionally, the surface area correction had to be applied to the term in the governing equations which accounts for gaseous diffusion of atoms through the fuel matrix to bubbles. This term is dependent on available surface area and not bubble volume. Therefore, this term becomes:

$$J_{gi} = 1.95 \times k_{gi} C_g N_{bi} \qquad \textbf{Eqn. 118}$$

Following these changes to the code, a benchmark was performed and the following results were obtained.

Table 7: Fitting factors for phase dependent version of the code [16]

Code	Diffusion Constant $\beta+\gamma/\alpha+\delta$	Diffusion Constant γ-only	Open Bubble Formation Coefficient	Surface Area Correction Factor	Effective Porosity Correction
Constant Volume (2 Group)	2.70E-03	2.70E-03	0.24	0.2	1.0
Constant Atom Number	3.50E-03	3.50E-03	0.40	0.5	0.3
Phase Dependent Version	1.0E-04	0.3E-08	0.40	0.3	0.23

3.4. Coalescence Probability Verification

Since the probability of two bubbles coalescing is dependent on the distance between the bubbles, a Monte-Carlo algorithm was developed to find the distance between these bubbles. Initially, this was based on the assumption that the fission gas bubbles are isotropically distributed through the fuel matrix in an FCC lattice. Currently, the probability of two bubbles coalescing is expressed with the following equations. The relation of this model to the rest of the algorithm can be seen in the previous chapter. Equation 119 is for closed bubbles, and Equation 120 is for open bubbles; Equation 121 is the spacing between two bubbles in a homogenous FCC lattice.

$$P_{ij} = \frac{\Delta r_{bi}}{0.5 l_j - (r_{bi} + r_{bj})} \qquad \textbf{Eqn. 119}$$

$$P_{ij} = \frac{\Delta r_{bi}}{d_l l_j} \qquad \textbf{Eqn. 120}$$

$$l_j = 1.122 N_{bj}^{-1/3} \qquad \textbf{Eqn. 121}$$

In this study, a new expression was sought for the term l_j in the case of closed bubbles. The open bubble probability term is based on the closed bubble term for bubbles of the same size.

3.4.1. Monte-Carlo Algorithm for Bubble Spacing Determination

The Monte-Carlo algorithm developed generates bubbles randomly in a 200 micron cube with periodic boundary conditions. The size of the bubbles is based on the probability distribution function (PDF) obtained experimetally [18]. The PDF functions were developed for the size distribution of fission gas bubbles in a U-10Zr fuel before irradiation in the high temperature single–gamma phase.

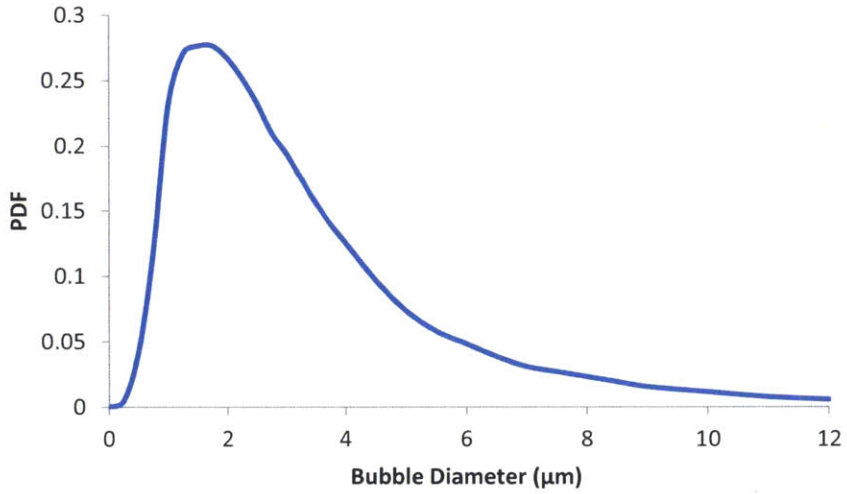

Figure 25: Probability distribution function for bubble diameter for experimental work given in [18]

For this PDF, the average bubble size is 2.7 microns. In order to account for the effects of irradiation and the fact that FEAST-METAL uses a two group model, the PDF was scaled to model bubbles with average radii of 0.5 and 5 microns. In order to account for the possibility of bubbles overlapping one another after they are generated by the code, once bubbles are generated they are checked against bubbles that were generated previously in the same region. If the bubbles are overlapping, they are moved apart along the line connecting them until they no longer touch. This is done by determining the vector between two successive bubbles and then increasing the magnitude of this vector if the bubbles overlap.

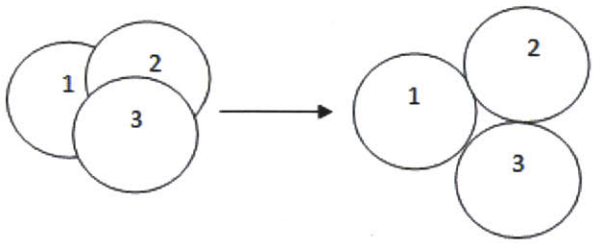

Figure 26: Bubble separation scheme [21]

Additionally, the algorithm needed to take into account the fact that there is a distribution between open and closed bubbles. In order to do this, bubbles contained in cracks that were over 30 microns wide were considered to be open pores. This definition is based on the selection criterion for critical crack length density at which fuel fracture (and thus fission gas release) takes place as defined in [21]. In that reference the critical crack length density is approximated as 1.5E+13 m/m^3 for cracks above 30 μm. In the algorithm, a crack is defined as the total length of connected bubbles. It contains at least 2 bubbles, but has no maximum number. The crack algorithm tracks interconnected bubbles up to the point at which the scalar product of the crack vector between the starting bubble pair and the last bubble pair becomes less than zero.

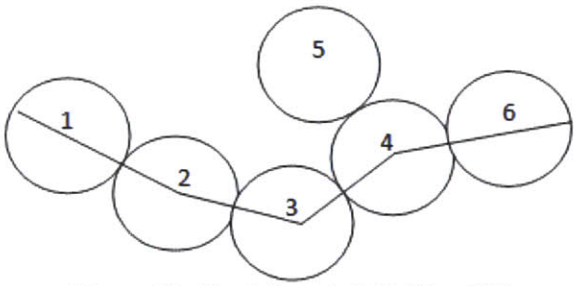

Figure 27: Crack length definition [21]

As can be seen in Figure 27, the crack follows bubble-1, 2, 3, 4, and 6. The chain starting with bubble-1 and ending at bubble-5 is not taken into consideration because the vector between bubble 4 and bubble-5 changes its direction with respect to the vector between the bubble-1 and bubble-2. Using this definition, swelling in 5% intervals from 5% to 60% was simulated. From this, the number density of open and closed pores for both small and large bubbles was determined. This was then plotted against the average distance between the bubbles of the same type. This led to Figure 28 and Figure 29 for closed pores. The intercept for both was set to zero.

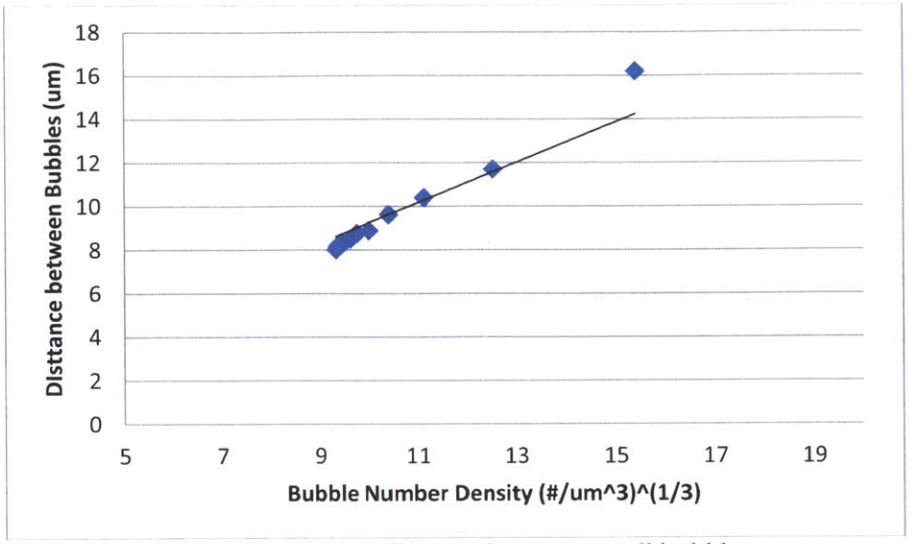

Figure 28: Average distance between small bubbles

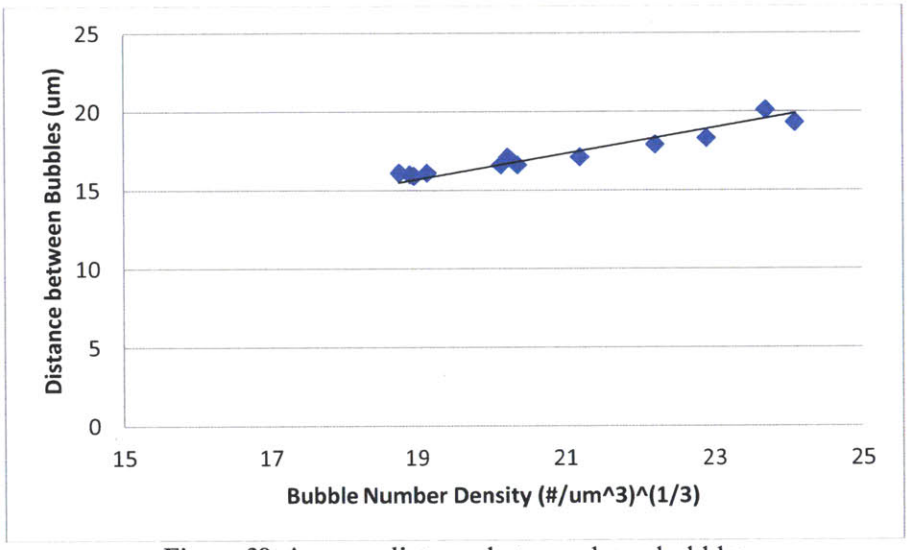

Figure 29: Average distance between large bubbles

Accordingly, Equation 122 becomes the new distance equation for small closed bubbles.

$$l_1 = 0.9239 N_{b1}^{-1/3} \qquad \text{Eqn. 122}$$

And, Equation 123 becomes the new distance equation for large closed bubbles.

$$l_2 = 0.8252 N_{b3}^{-1/3} \qquad \text{Eqn. 123}$$

With these equations, a new benchmark was developed using four new fitting parameters, which are the same four used in the other cases. Table 8 shows the fitting parameters used in this case. It should be noted that the version of the code with the new distance equations also contains the modifications present in the phase dependent version of the code.

Table 8: Fitting parameters used with new distance case [16]

Code	Diffusion Constant $\beta+\gamma/\alpha+\delta$	Diffusion Constant γ-only	Open Bubble Formation Coefficient	Surface Area Correction Factor	Effective Porosity Correction
Constant Volume (2 Group)	2.70E-03	2.70E-03	0.24	0.2	1.0
Constant Atom Number	3.50E-03	3.50E-03	0.40	0.5	0.3
Phase Dependent Version	1.0E-04	0.3E-08	0.40	0.3	0.23
New Distance Version	2.0E-4	0.3E-09	0.40	0.1	0.13

4. Verification of New FEAST-METAL Versions and Application to Long-term Irradiation

In this chapter, the results of the benchmarks performed with each version of the code are discussed. Specifically, the integral fractional fission gas release, total cladding hoop strain, axial fuel elongation and fuel swelling are examined for fuel irradiation cases from EBR-II and a long term case that is similar to the Travelling Wave Reactor fuel.

4.1. Irradiation Cases

This section contains information on irradiation cases from EBR-II against which the code was benchmarked. Both the X425 and the X430 benchmarks are detailed with information on the fuel parameters, the linear power and the coolant outlet temperature. The fuel fission density rate and total neutron flux are directly related to linear power and thus follow the same trend, so plots of their behavior are not included. This section also has information on a U-6Zr irradiation, which is similar to what may be experienced in the Travelling Wave Reactor. The full input decks can be seen in Appendix A and Appendix B. The X447 case from EBR-II was not used for comparison since FEAST-METAL does not model tertiary creep in an effective manner. Additionally, the temperature is well above the failure point for X447, so without cladding material information validity is suspect. FEAST-METAL is a pin analysis code and the X447 data provided is based on full assembly data, so this produces inaccuracies. Additionally, plutonium concentrations are based on initial HM content; ideally, this would be based on irradiation history, but the flux profile is not available to calculate this history.

4.1.1. X425 Benchmark

This section contains information on the irradiation of the X425 fuel assembly at EBR-II. Table 9 shows the parameters of the irradiation. Figure 30 and Figure 31 provide information on the linear power and peaking. Figure 32 shows the coolant outlet temperature. Because of the high initial plutonium content, this fuel is igniter fuel and not part of the blanket.

Table 9: X425 benchmark parameters [4]

Parameter	Value
Fuel composition	U-19Pu-10Zr
Cladding material	HT-9
Fuel slug radius (mm)	2.16
Cladding inner radius (mm)	2.54
Cladding outer radius (mm)	2.92
Active fuel length (cm)	34.3
Fuel smear density (%)	72.4
Plenum length to fuel length ratio	1.0
Fast flux fraction	1.0
Axial peaking factor	1.12
Initial maximum fission density rate (fissions/cm³/s)	0.812E+14
Initial maximum steady state neutron flux (neutrons/cm²/s)	0.230E+16
Coolant inlet temperature (°C)	370
Peak cladding temperature (°C)	590
Peak dose at end of life (dpa)	~95
Peak burnup (at%)	18.9

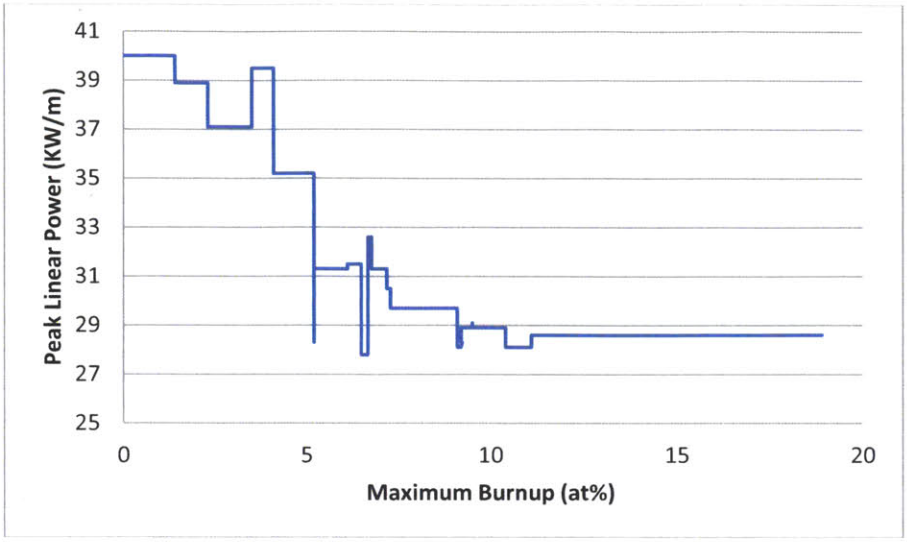

Figure 30: Peak linear power for X425 benchmark [4]

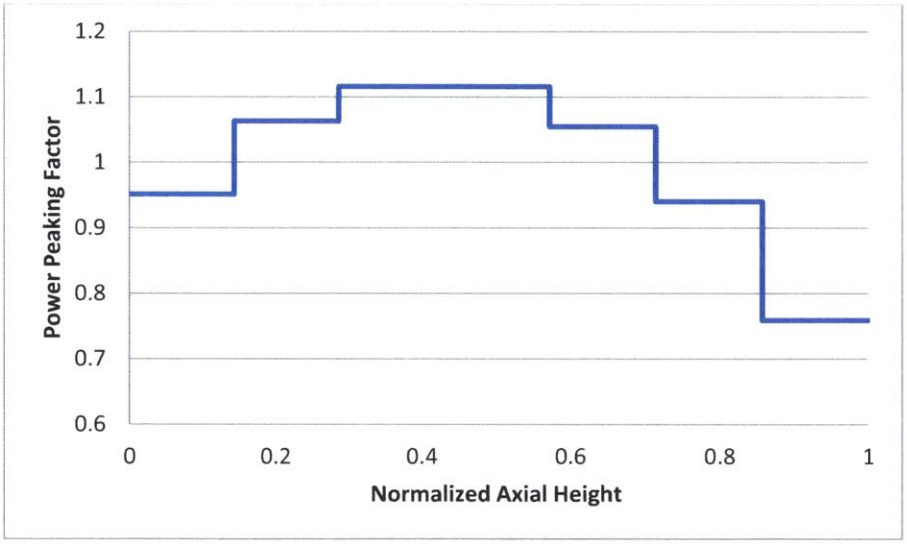

Figure 31: Power peaking factor for X425 benchmark [4]

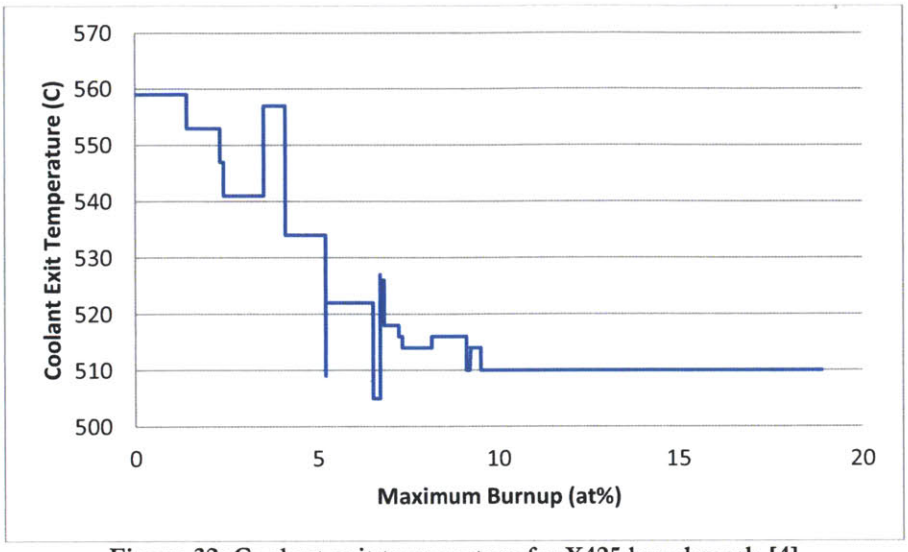

Figure 32: Coolant exit temperature for X425 benchmark [4]

4.1.2. X430 Benchmark

This section contains information on the irradiation of the X430 fuel assembly at EBR-II. Table 10 shows the parameters of the irradiation. Figure 33 and Figure 34 provide information on the linear power and peaking. Figure 35 shows the coolant outlet temperature. Because of the high initial plutonium content, this fuel is igniter fuel and not part of the blanket.

Table 10: X430 benchmark parameters [4]

Parameter	Value
Fuel composition	U-19Pu-10Zr
Cladding material	HT-9
Fuel slug radius (mm)	2.86
Cladding inner radius (mm)	3.28
Cladding outer radius (mm)	3.68
Active fuel length (cm)	34.3
Fuel smear density (%)	76.1
Plenum length to fuel length ratio	1.4
Fast flux fraction	1.0
Axial peaking factor	1.12
Initial maximum fission density rate (fissions/cm³/s)	0.574E+14
Initial maximum steady state neutron flux (neutrons/cm²/s)	0.163E+16
Coolant inlet temperature (°C)	370
Peak cladding temperature (°C)	590
Peak dose at end of life (dpa)	~60
Peak burnup (at%)	11.6

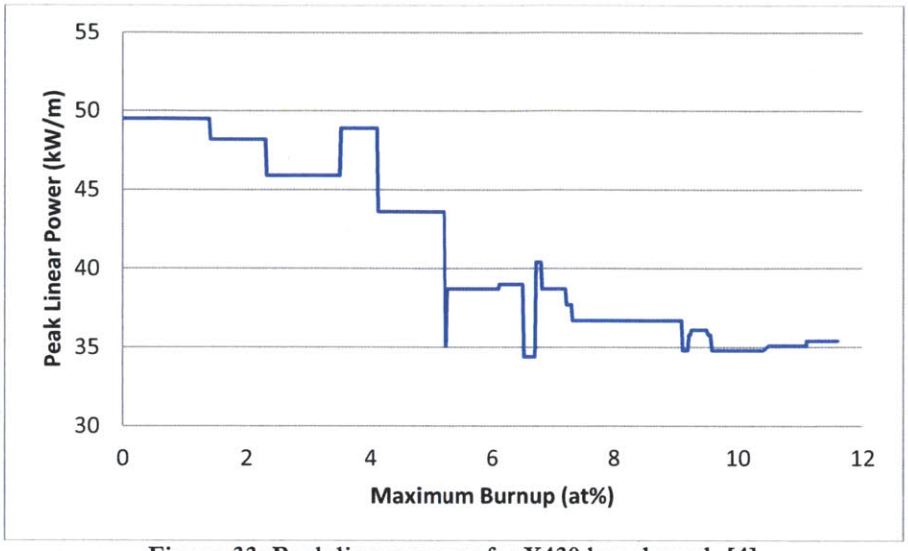

Figure 33: Peak linear power for X430 benchmark [4]

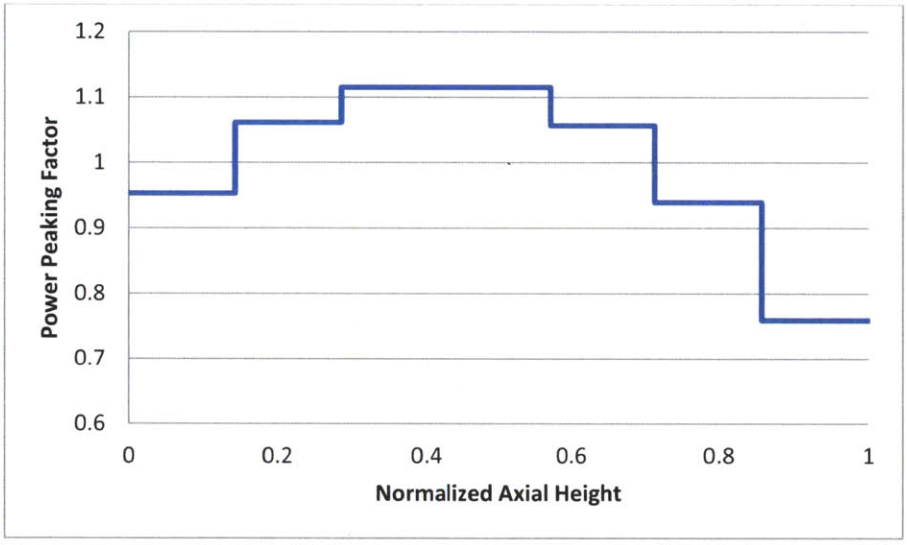

Figure 34: Power peaking factor for X430 benchmark [4]

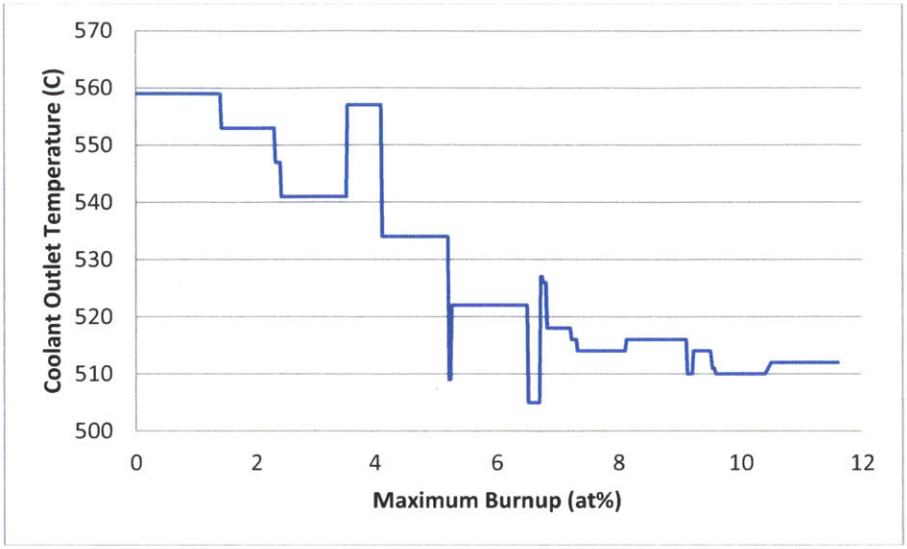

Figure 35: Coolant outlet temperature for X430 benchmark [4]

4.1.3. Long-term Irradiation

This section contains information on an assembly that is similar to the ones proposed for the Travelling Wave Reactor. The large increase in power at ~5 at% burnup indicates that the fuel has been moved from the exterior region of the core to the central region. Table 11 shows the parameters of the irradiation. Figure 36 and Figure 37 provide information on the linear power and peaking. Figure 38 shows the coolant outlet temperature.

Table 11: Long-term case parameters [21]

Parameter	Value
Fuel composition (wt %)	U-6Zr
Clad material	HT9
Fuel slug density (g/cm³)	17
Fuel slug radius (mm)	3.0
Clad inner radius (mm)	3.87
Clad outer radius (mm)	4.50
Fuel smear density (%)	60.0
Fuel active length (cm)	200
Plenum	Vented
Fast flux fraction	1.0
Axial peaking factor	1.4
Initial maximum fission density rate (fissions/cm³/s)	0.526E+13
Initial maximum steady state neutron flux (neutrons/cm²/s)	0.447E+15
Coolant inlet temperature (°C)	390
Peak cladding temperature (°C)	550
Peak dose at end of life (dpa)	~500
Peak burnup (at%)	36

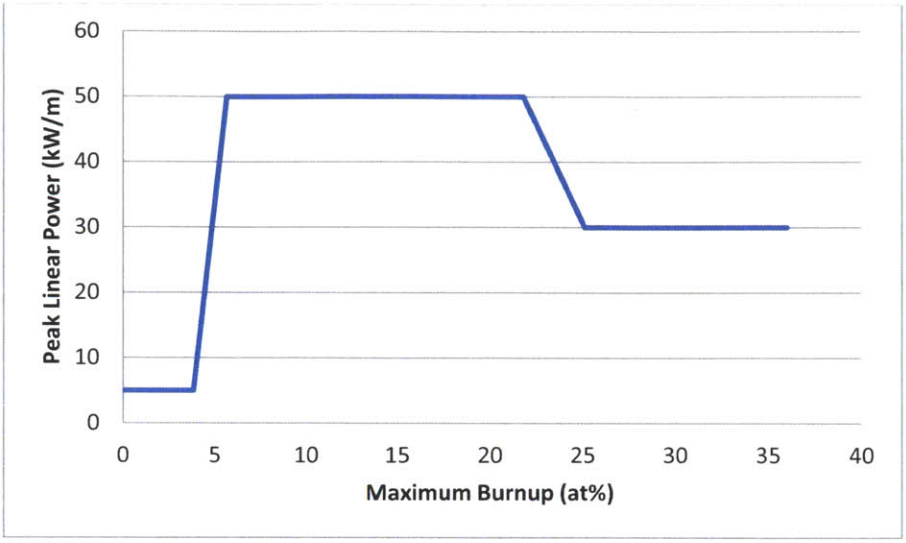

Figure 36: Peak linear power for long-term case [21]

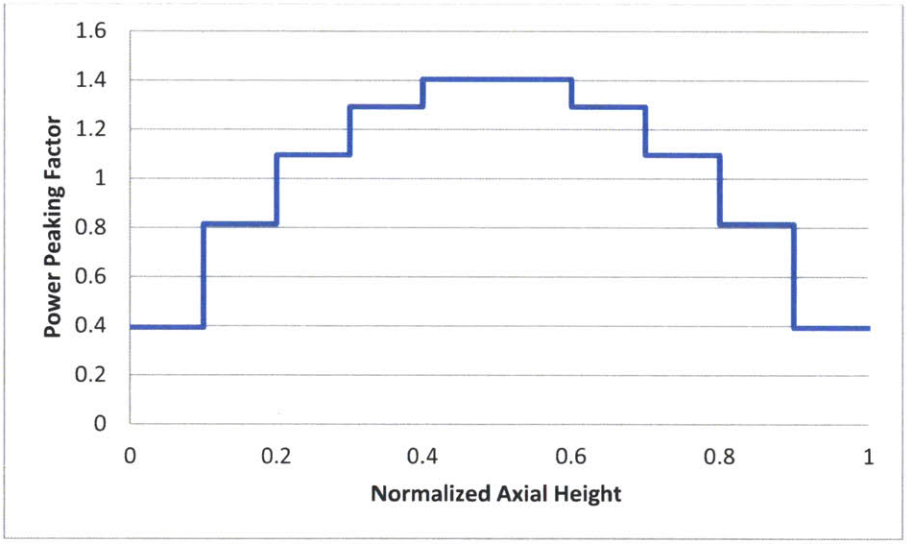

Figure 37: Power peaking factor for long-term case [21]

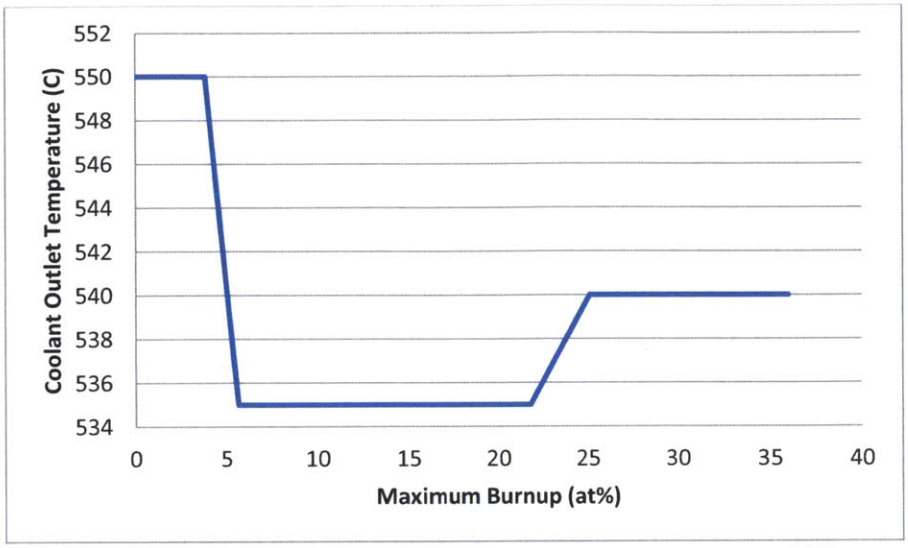

Figure 38: Coolant benchmark parameters for long-term case [21]

4.2. Benchmark against X425 and X430 Assemblies from EBR-II

All versions of the code developed were benchmarked against data from EBR-II. This section contains the results of these benchmarks for the maximum cladding strain, fractional fission gas release and fuel axial elongation. Fuel swelling plots are also shown for the third axial node, which had the highest cladding hoop strain. This demonstrates that the code is treating the interaction of the three types of fuel swelling – open, closed and solid fission products – correctly. In lieu of explaining the results in each of the following sub-sections, an overall explanation of the results will be included after all of the results from the benchmarks are summarized.

4.2.1. Constant Volume Approach (2, 3, 4 Bubble Groups)

This section contains the benchmarked results for the 2, 3 and 4 bubble group version of the code. The 2 group results are from the original version of the code developed by Dr. Karahan. All three versions addressed here use a constant volume approach for bubble groups.

2 Group

This section contains the cladding strain, fission gas release and fuel axial elongation results for the X425 and X430 benchmarks for the 2 group version of the code. Cladding strain is presented in Figure 39, while fission gas release and axial elongation can be seen in Figure 40 and Figure 41 respectively. Fuel swelling results obtained for the third axial node, which has the highest amount of cladding strain, are also shown for the X425 case in Figure 42.

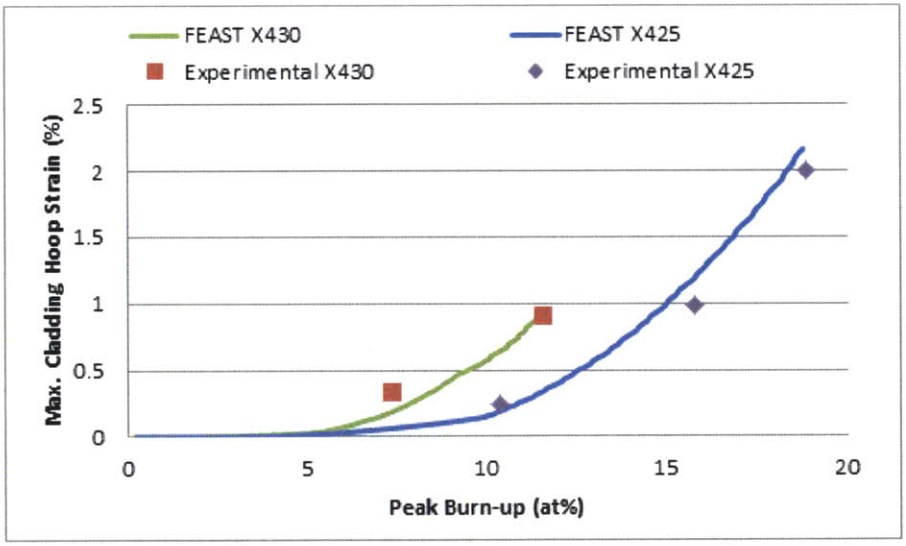

Figure 39: Maximum cladding strain results for the 2 group constant volume number version of FEAST-METAL for both X425 and X430 from EBR-II [2]

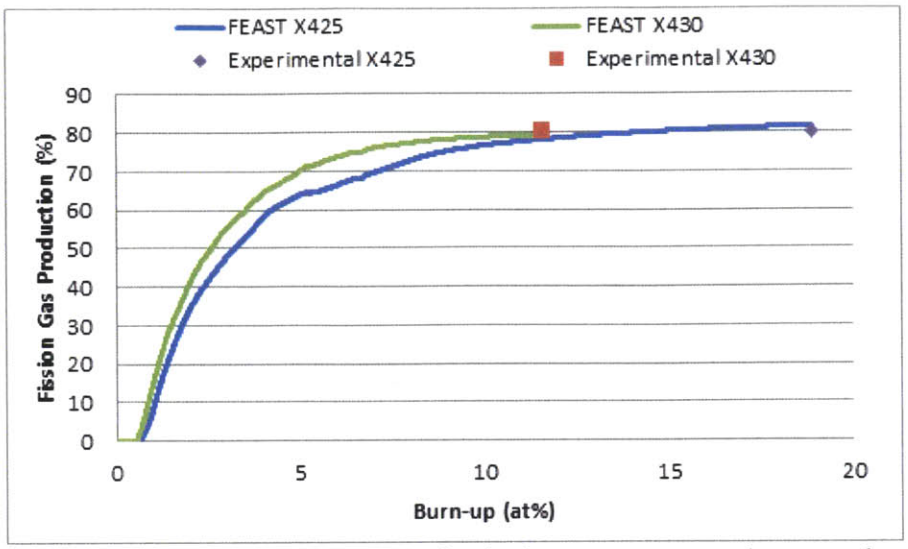

Figure 40: Fractional fission gas release results for the 2 group constant volume number version of FEAST-METAL for both X425 and X430 from EBR-II [2]

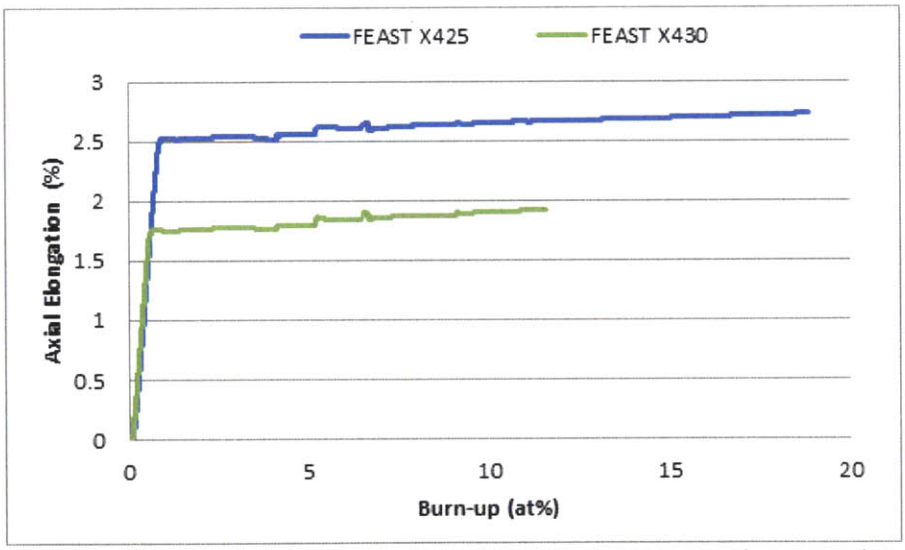

Figure 41: Fuel axial elongation release results for the 2 group constant volume number version of FEAST-METAL for both X425 and X430 from EBR-II

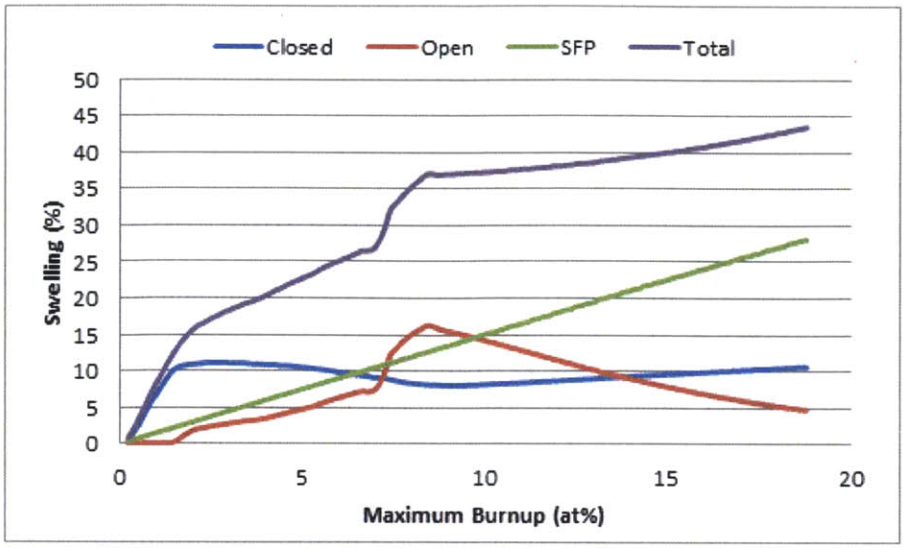

Figure 42: Fuel swelling results showing closed, open, solid fission products and total swelling for the 2 group constant volume number version of FEAST-METAL for case X425 at 0.37 normalized axial height

3 Group

This section contains the cladding strain, fission gas release and fuel axial elongation results for the X425 and X430 benchmarks for the 3 group version of the code. Cladding strain is presented in Figure 43, while fission gas release and axial elongation can be seen in Figure 44 and Figure 45 respectively. Fuel swelling results obtained for the third axial node can be seen in Figure 46 for the X425 case.

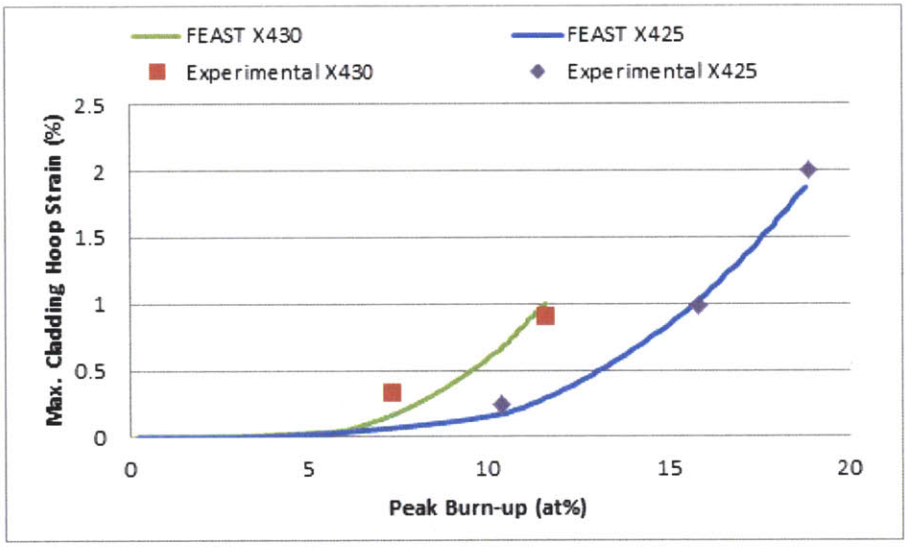

Figure 43: Maximum cladding strain results for the 3 group constant volume number version of FEAST-METAL for both X425 and X430 from EBR-II [2]

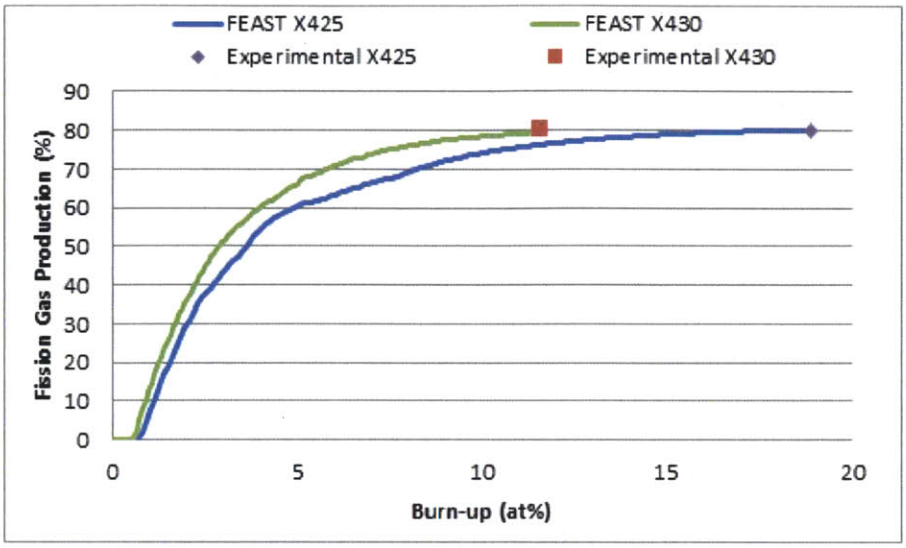

Figure 44: Fractional fission gas release results for the 3 group constant volume number version of FEAST-METAL for both X425 and X430 from EBR-II [2]

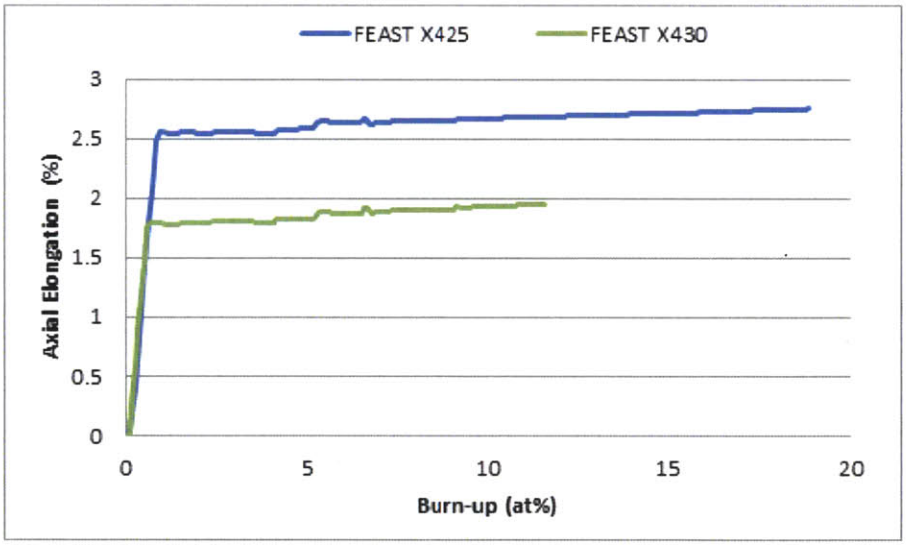

Figure 45: Fuel axial elongation release results for the 3 group constant volume number version of FEAST-METAL for both X425 and X430 from EBR-II

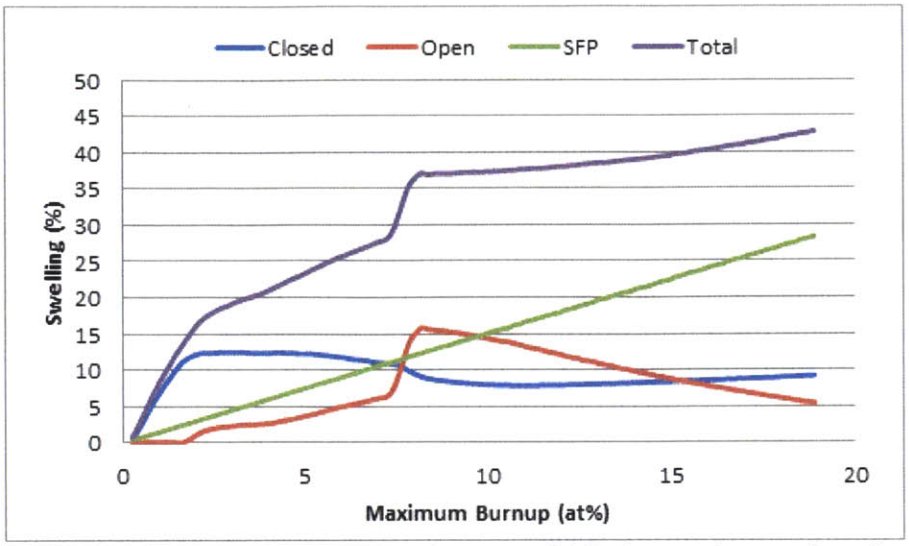

Figure 46: Fuel swelling results showing closed, open, solid fission products and total swelling for the 3 group constant volume number version of FEAST-METAL for case X425 at 0.37 normalized axial height

4 Group

This section contains the cladding strain, fission gas release and fuel axial elongation results for the X425 and X430 benchmarks for the 4 group version of the code. Cladding strain is presented in Figure 47, while fission gas release and axial elongation can be seen in Figure 48 and Figure 49 respectively. Fuel swelling results obtained for the third axial node can be seen in Figure 50 for the X425 case.

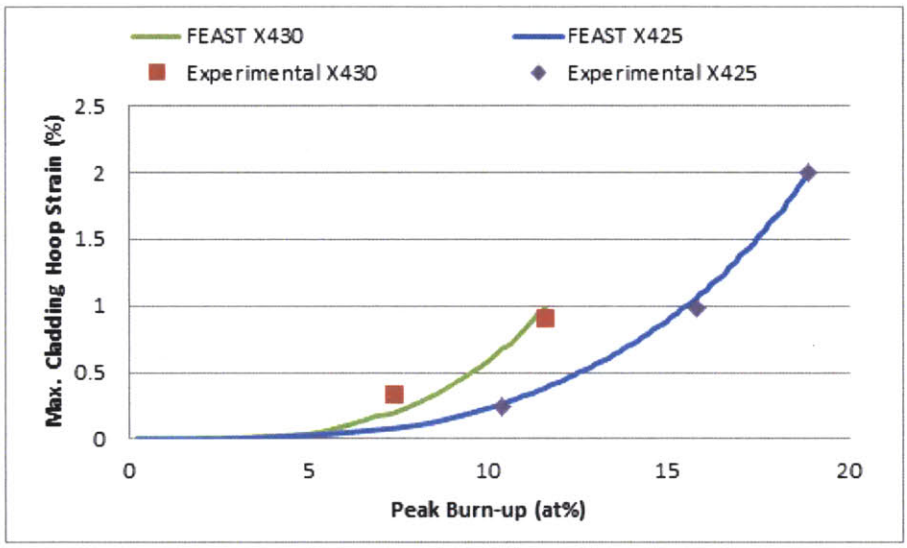

Figure 47: Maximum cladding strain results for the 4 group constant volume number version of FEAST-METAL for both X425 and X430 from EBR-II [2]

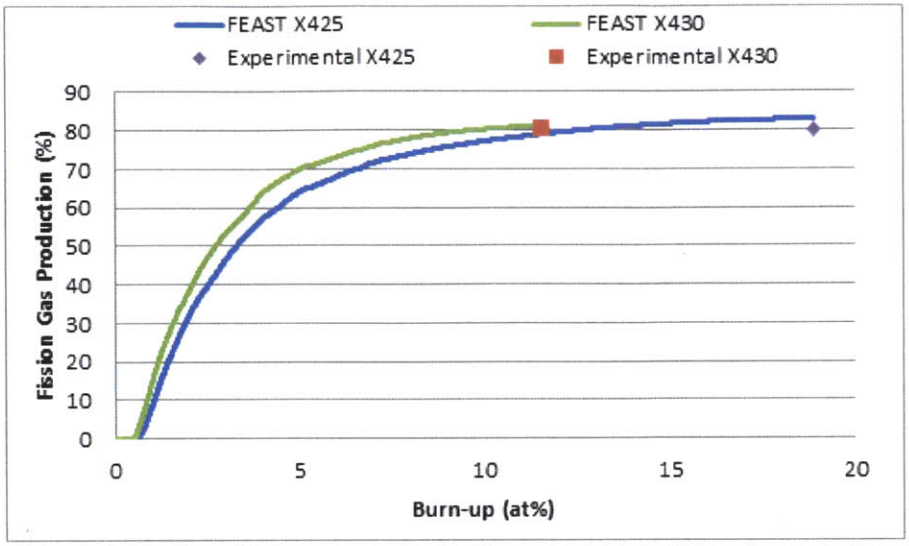

Figure 48: Fractional fission gas release results for the 4 group constant volume number version of FEAST-METAL for both X425 and X430 from EBR-II [2]

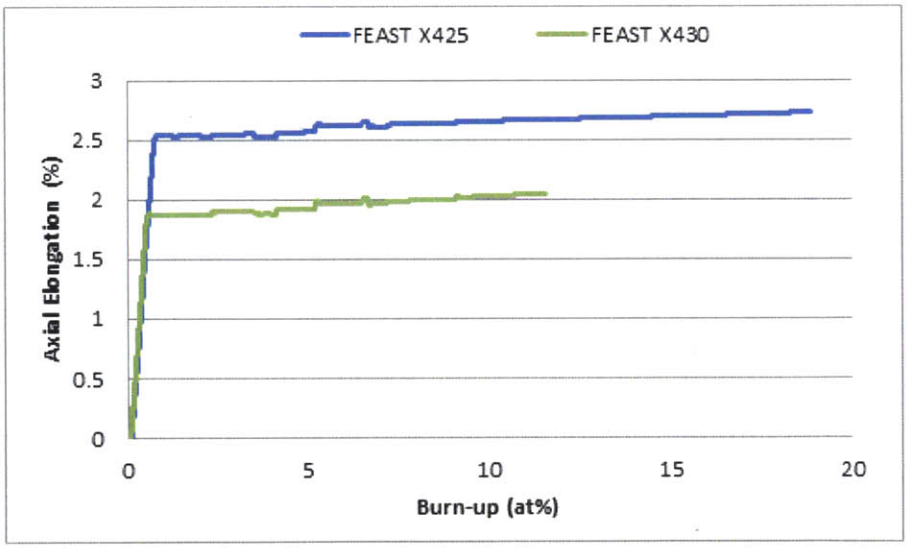

Figure 49: Fuel axial elongation release results for the 4 group constant volume number version of FEAST-METAL for both X425 and X430 from EBR-II

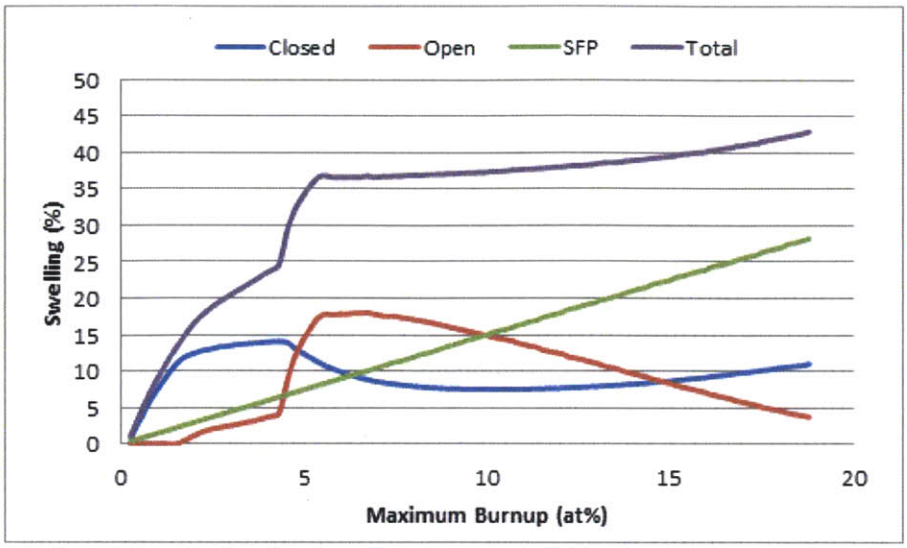

Figure 50: Fuel swelling results showing closed, open, solid fission products and total swelling for the 4 group constant volume number version of FEAST-METAL for case X425 at 0.37 normalized axial height

4.2.2. Constant Atom Number Approach

This section contains the cladding strain, fission gas release and fuel axial elongation results for the X425 and X430 benchmarks for the constant atom number version of the code. Cladding strain is contained in Figure 51, while fission gas release and axial elongation can be seen in Figure 52 and Figure 53 respectively. Fuel swelling results obtained for the third axial node can be seen in Figure 54 for the X425 case.

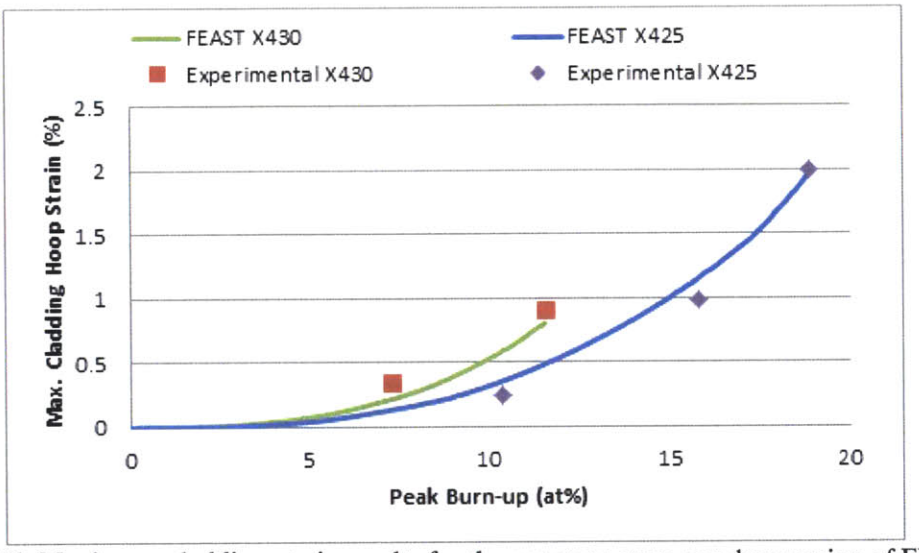

Figure 51: Maximum cladding strain results for the constant atom number version of FEAST-METAL for both X425 and X430 from EBR-II [2]

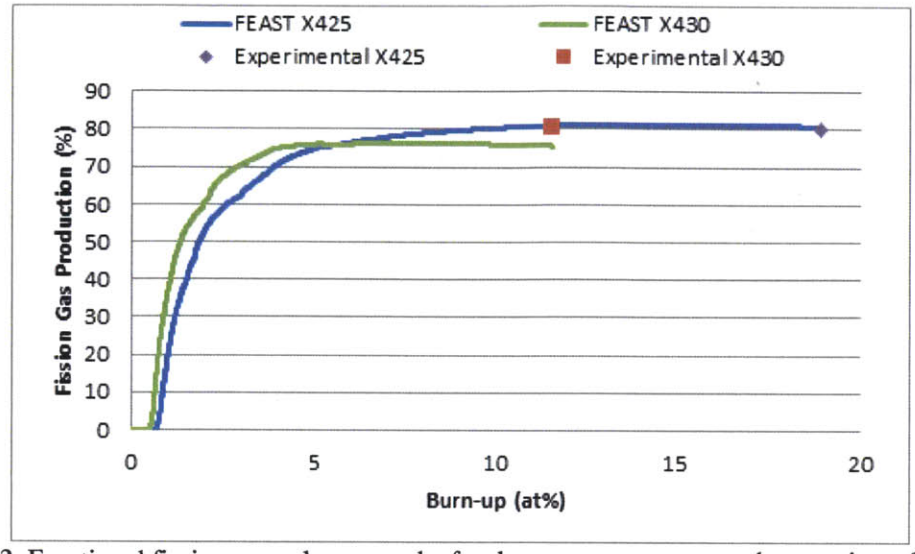

Figure 52: Fractional fission gas release results for the constant atom number version of FEAST-METAL for both X425 and X430 from EBR-II [2]

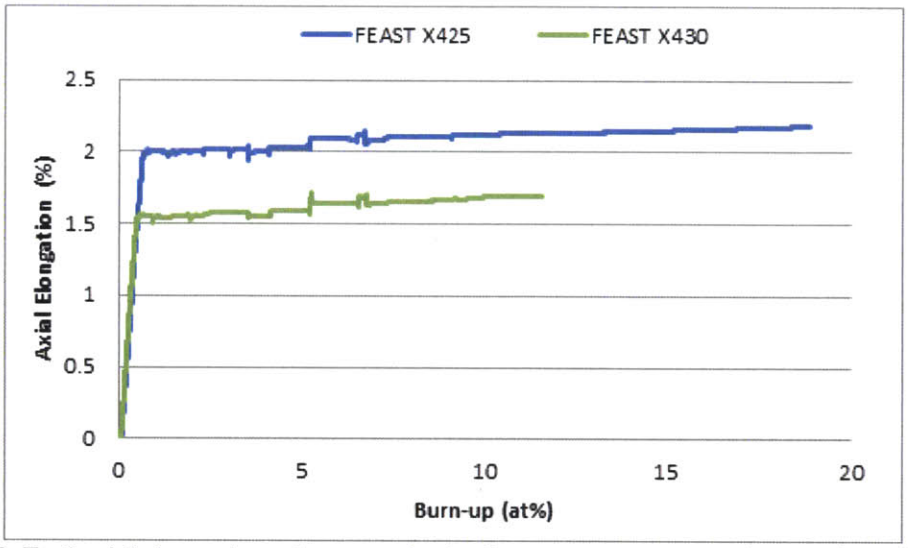

Figure 53: Fuel axial elongation release results for the constant atom number version of FEAST-METAL for both X425 and X430 from EBR-II

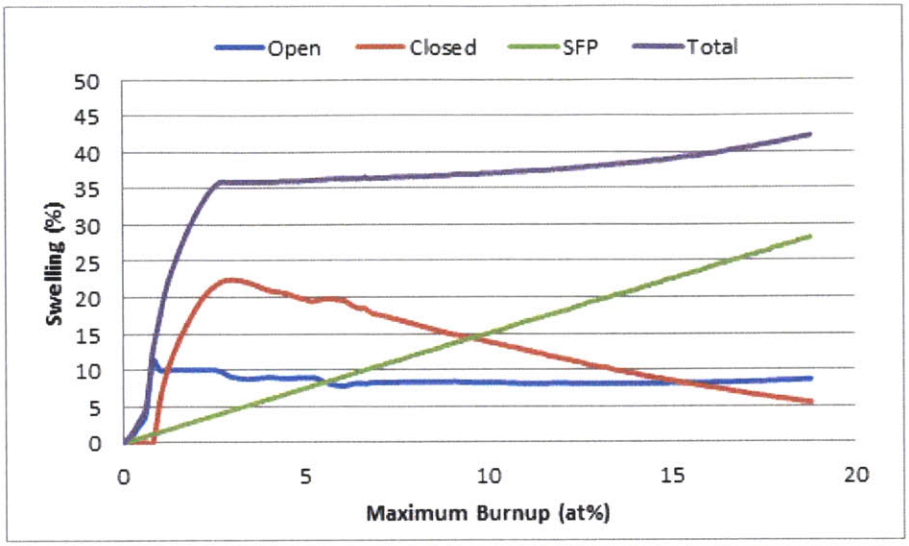

Figure 54: Fuel swelling results showing closed, open, solid fission products and total swelling for the constant atom number version of FEAST-METAL for case X425 at 0.37 normalized axial height

4.2.3. Phase Dependent Approach

This section contains the cladding strain, fission gas release and fuel axial elongation results for the X425 and X430 benchmarks for the phase dependent version of the code. Cladding strain is contained in Figure 55, while fission gas release and axial elongation can be seen in Figure 56 and Figure 57 respectively. Fuel swelling results obtained for the third axial node can be seen in Figure 58 for the X425 case.

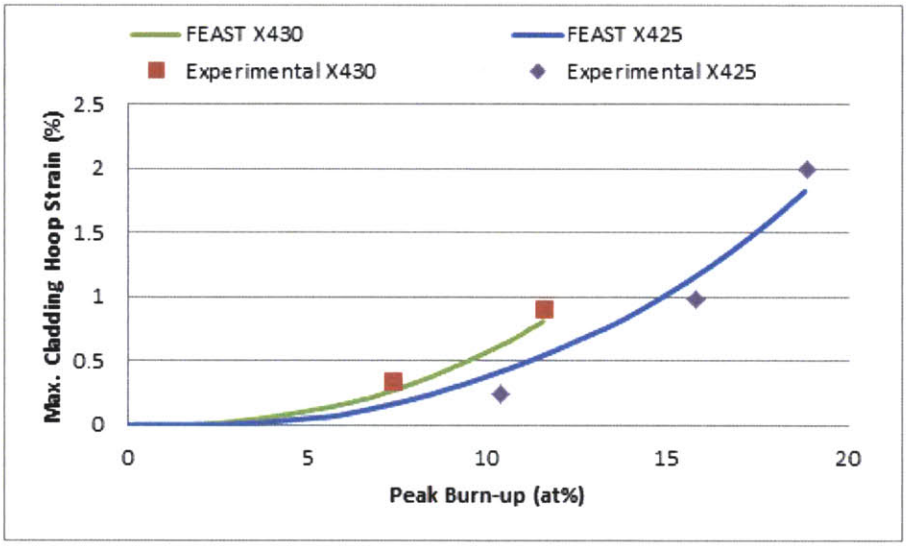

Figure 55: Maximum cladding strain results for the phase dependent constant atom number version of FEAST-METAL for both X425 and X430 from EBR-II [2]

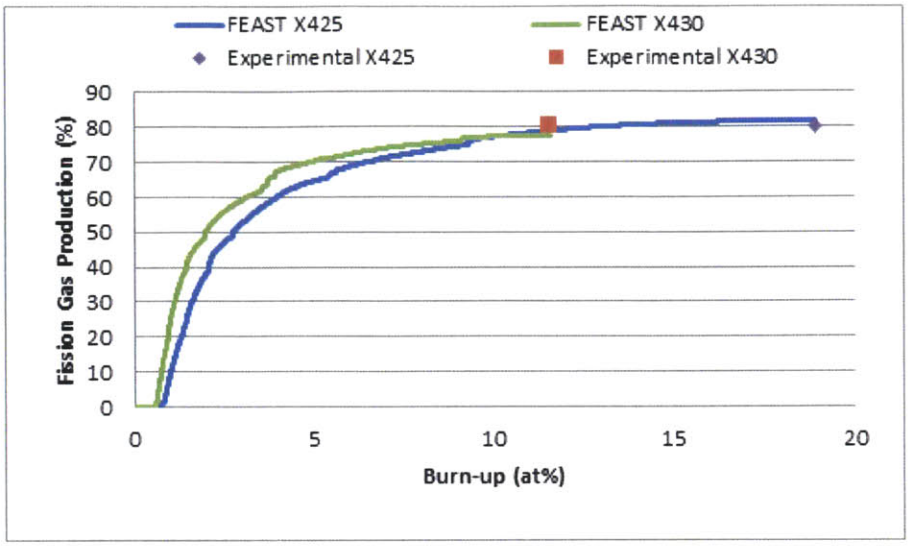

Figure 56: Fractional fission gas release results for the phase dependent constant atom number version of FEAST-METAL for both X425 and X430 from EBR-II [2]

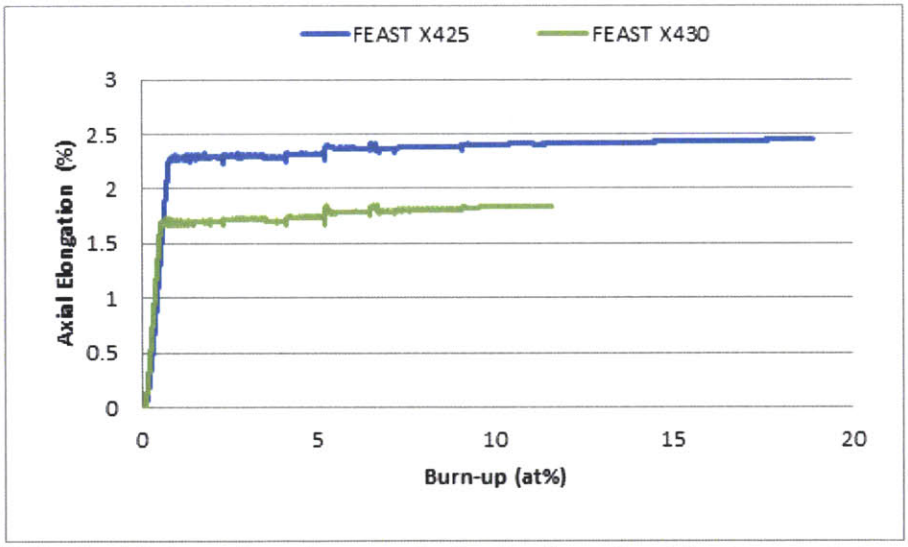

Figure 57: Fuel axial elongation release results for the phase dependent constant atom number version of FEAST-METAL for both X425 and X430 from EBR-II

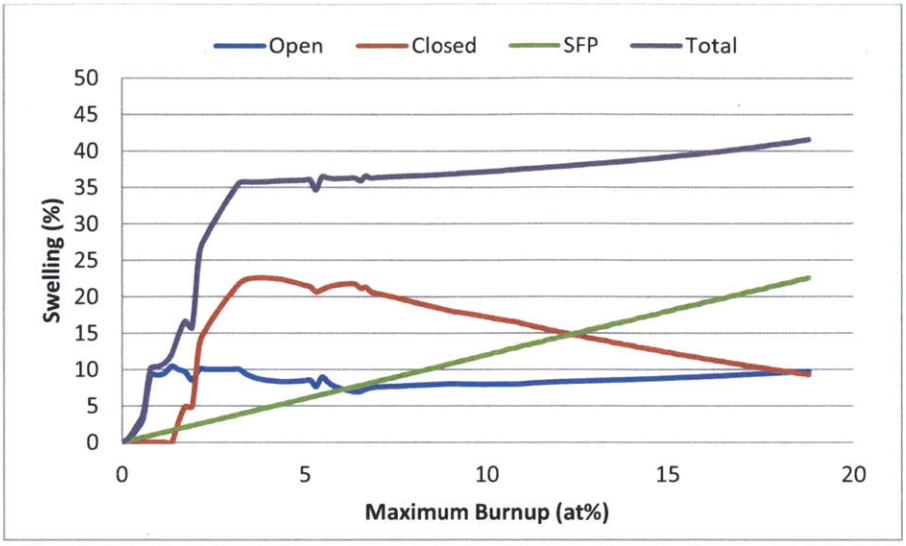

Figure 58: Fuel swelling results showing closed, open, solid fission products and total swelling results for the phase dependent constant atom number version of FEAST-METAL for case X425 at 0.37 normalized axial height

4.2.4. Using Improved Bubble Spacing Equations

This section contains the cladding strain, fission gas release and fuel axial elongation results for the X425 and X430 benchmarks for the phase dependent version of the code with altered bubble spacing equations. Cladding strain is contained in Figure 59, while fission gas release and axial elongation can be seen in Figure 60 and Figure 61 respectively. Fuel swelling results obtained for the third axial node can be seen in Figure 62 for the X425 case.

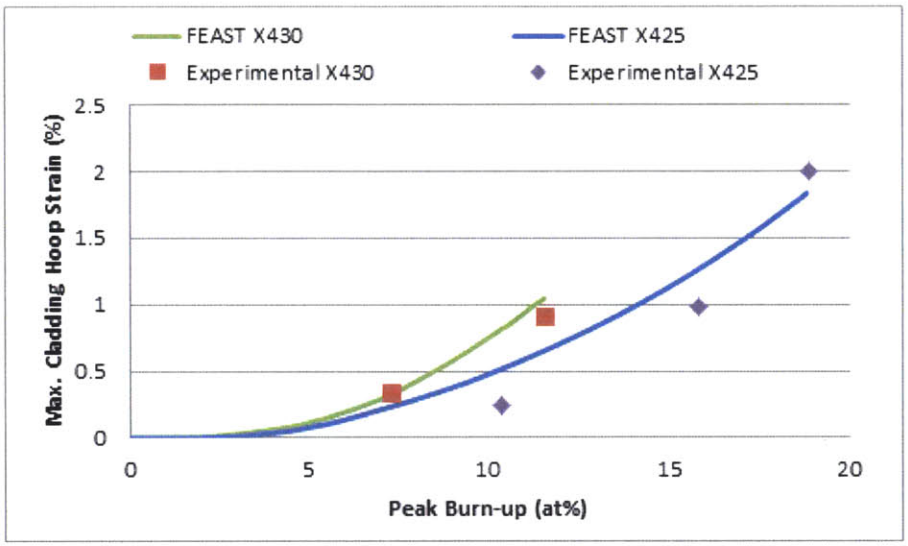

Figure 59: Maximum cladding strain results for the phase dependent constant atom number version with improved bubble distance equations of FEAST-METAL for both X425 and X430 from EBR-II [2]

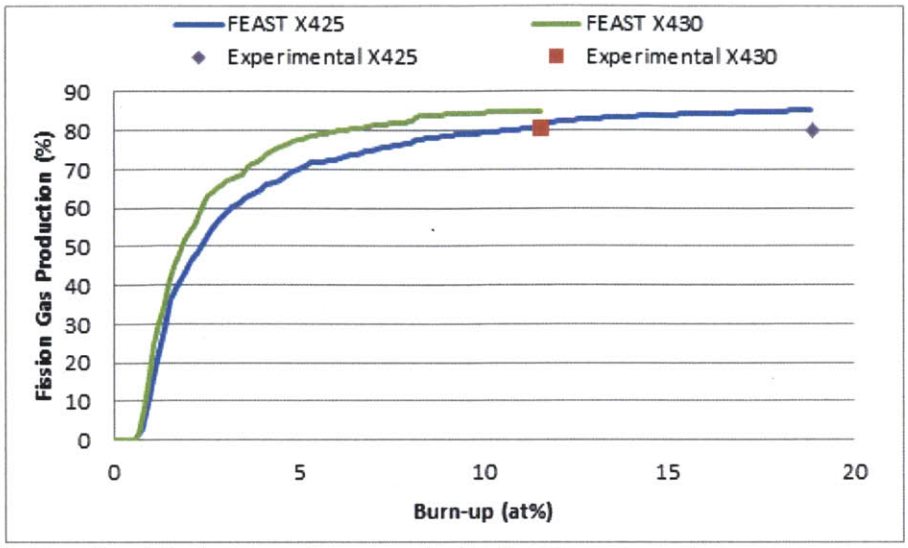

Figure 60: Fractional fission gas release results for the phase dependent constant atom number version with improved bubble distance equations of FEAST-METAL for both X425 and X430 from EBR-II [2]

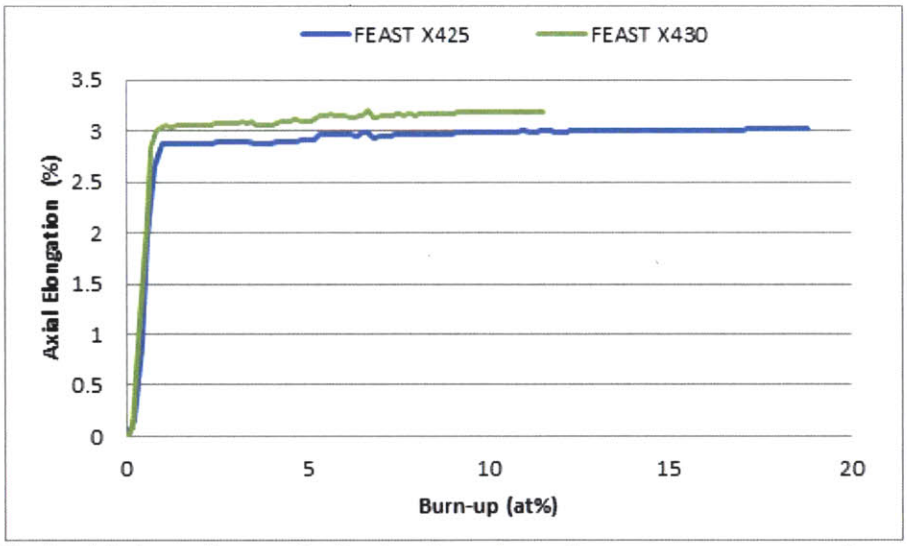

Figure 61: Fuel axial elongation results for the phase dependent constant atom number version with improved bubble distance equations of FEAST-METAL for both X425 and X430 from EBR-II

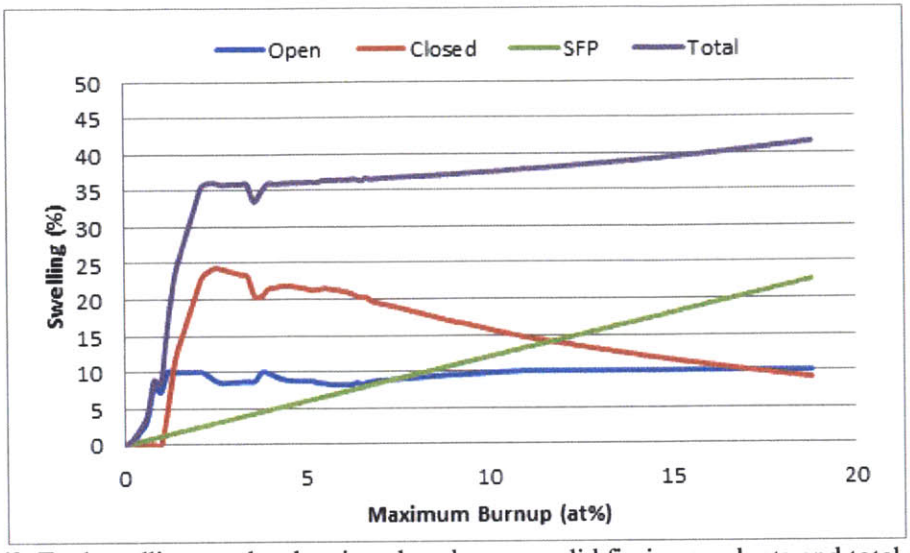

Figure 62: Fuel swelling results showing closed, open, solid fission products and total swelling results for the phase dependent constant atom number version with altered bubble distance equations of FEAST-METAL for case X425 at 0.37 normalized axial height

4.3. Comparison and Validity of Benchmarks

This section compares the results of the above benchmarks for fission gas release, cladding strain and axial elongation. It also shows the anisotropy fitting factor benchmarks developed for each case. For this, both high and low power cases are used. Figure 63 and Figure 64 show the anisotropy factors used for the constant volume version of the code.

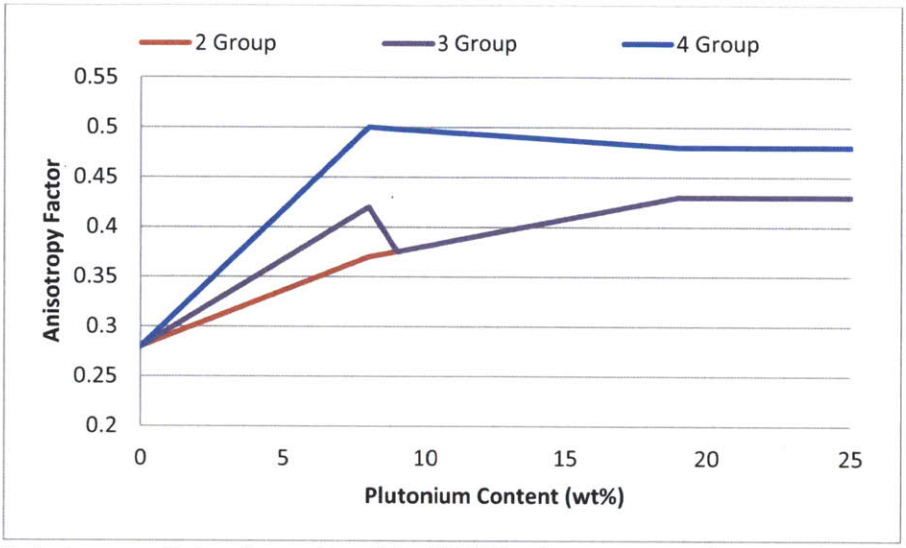

Figure 63: Anisotropy fitting factor for q/D=650 W/m for constant volume versions of FEAST-METAL [16]

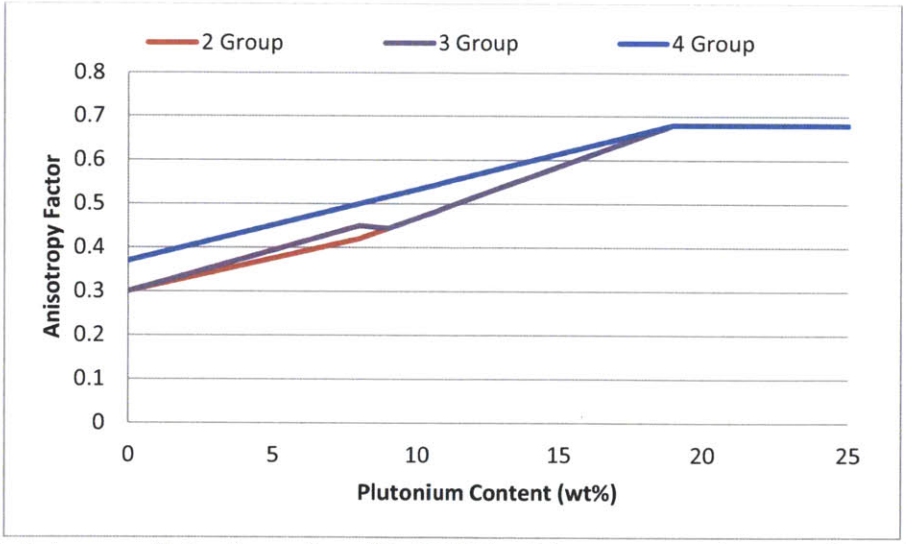

Figure 64: Anisotropy fitting factor for q/D=790 W/cm² for constant volume versions of FEAST-METAL [16]

Results from these cases are summarized in Table 12. Experimental data is shown for each of these cases. The scatter of the experimental results is also shown. The final three experimental points only have one data point.

Table 12: Fuel axial elongation results for constant volume versions of FEAST-METAL

Fuel Composition	Fuel Smear Density (%)	Heat Flux q/D (W/cm^2)	Axial Elongation (%)				
			Experimental Data	Range of Data	2 Group	3 Group	4 Group
U-10Zr	76	790	6.2 [22]	±1.2	6.7	5.6	5.6
U-19Pu-10Zr	76		1.5 [22]	±0.7	1.9	2.0	2.0
U-10Zr	72	830	8.5 [3]	±1.2	8.3	7.9	6.5
U-8Pu-10Zr	72		6.5 [3]	±0.6	7.0	6.5	6.1
U-19Pu-10Zr	72		2.5 [3]	±0.8	2.8	2.8	2.7
U-10Zr	75	650	8 [10]	-	6.9	6.9	7.0
U-8Pu-10Zr	75		5.8 [10]	-	5.8	6.0	6.0
U-19Pu-10Zr	75		6.5 [10]	-	5.2	5.4	5.4

Along the same lines, the anisotropy fitting factor for the constant atom number versions of the code can be seen in Figure 65 for the low power case and Figure 66 for the high power case.

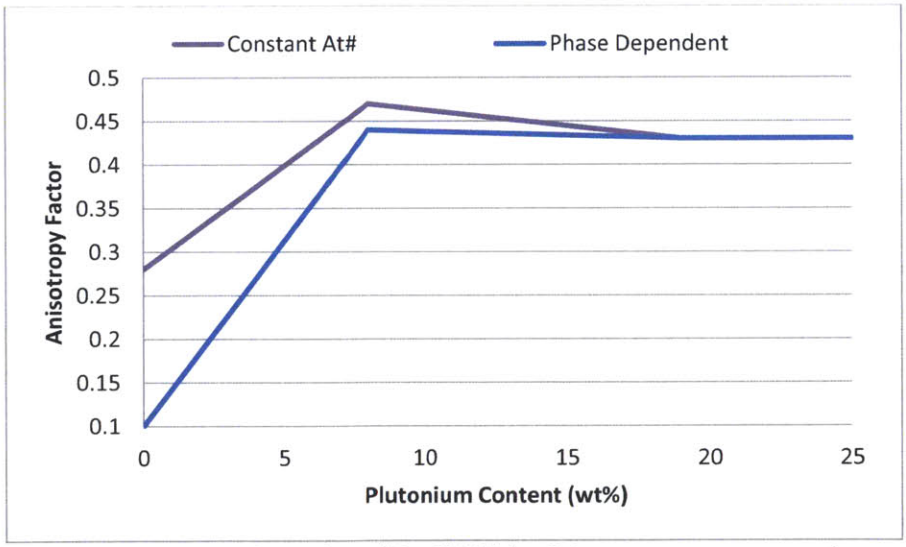

Figure 65: Anisotropy fitting factor for q/D=650 W/cm² for constant atom number versions of FEAST-METAL

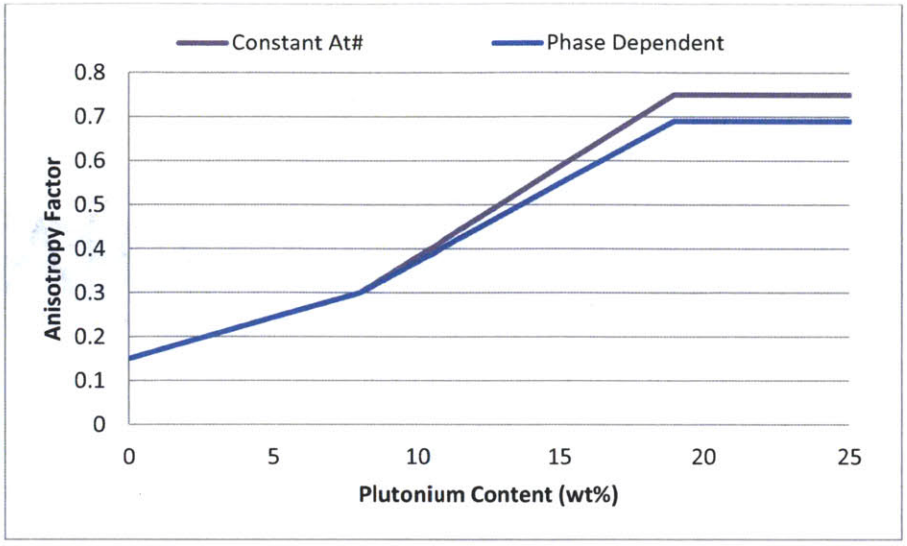

Figure 66: Anisotropy fitting factor for q/D=790 W/cm² for constant atom number versions of FEAST-METAL

Fuel axial elongation results for the three constant atom number versions of the code developed are shown in Table 13.

Table 13: Fuel axial elongation results for constant atom number versions of FEAST-METAL

Fuel Composition	Fuel Smear Density (%)	q/D (W/cm^2)	Axial Elongation (%)				
			Experimental Data	Range of Data	Constant Atom #	Phase Dependent	New Distance
U-10Zr	76	790	6.2 [22]	±1.2	5.2	7.1	-
U-19Pu-10Zr	76		1.5 [22]	±0.7	1.8	1.8	-
U-10Zr	72	830	8.5 [3]	±1.2	7.3	7.8	-
U-8Pu-10Zr	72		6.5 [3]	±0.6	6.3	6.7	-
U-19Pu-10Zr	72		2.5 [3]	±0.8	2.4	2.1	-
U-10Zr	75	650	8 [10]	-	8.4	8.0	-
U-8Pu-10Zr	75		5.8 [10]	-	4.5	5.8	-
U-19Pu-10Zr	75		6.5 [10]	-	6.8	7.1	-

Based on these results, no real conclusion can be made as to which version of the code is best. This is because this module of the code relies almost entirely on fitting parameters. This results in the data returned by the code being the same as experimental results.

A summary of the end of life fission gas release results for all the codes can be seen in Table 14. It is clear all of the codes show adequate matching of these results for both the X425 and X430 cases.

Table 14: Summary of fraction fission gas release results for developed benchmarks [2]

Case	Experimental	2 Group	3 Group	4 Group	Constant Atom #	Phase Dependent	New Distance Equations
X425	80	80	80	81	80	81	85
X430	80	80	80	80	75	78	85

The only data point for either is the end of life fractional fission gas release. However, general trends of fractional fission gas release can be seen in Figure 9. All of the benchmarks developed match this general trend. The greatest variation of the end of life data point is ~5% fractional gas release, which is well within the range of data obtained from similar tests in EBR-II.

All of the cladding strain results follow the general exponential trend. Table 15 and Table 16 show the relative error of the results cases for maximum cladding hoop strain for the X425 and the X430 cases.

Table 15: Cladding hoop strain results for constant volume versions of FEAST-METAL [2]

Case	Burnup (at%)	Experimental	2 Group	% Error	3 Group	% Error	4 Group	% Error
X425	10.4	0.25	0.19	-24	0.17	-32	0.265	6
	15.8	0.98	1.18	20	1.02	4	1.05	7
	18.9	2.00	2.19	10	1.90	-5	1.99	-1
X430	7.4	0.33	0.196	-41	0.17	-48	0.20	-39
	11.6	0.90	0.92	2	1.00	11	0.98	9

Table 16: Cladding hoop strain results for constant atom number versions of FEAST-METAL [2]

Case	Burnup (at%)	Experimental	Constant At#	% Error	Phase Dependent	% Error	New Dist. Eqn.	% Error
X425	10.4	0.25	0.35	40	0.42	68	0.52	108
	15.8	0.98	1.14	16	1.152	18	1.26	28
	18.9	2.00	1.94	-3	1.83	-9	1.83	-9
X430	7.4	0.33	0.22	-33	0.27	-18	0.34	3
	11.6	0.90	0.80	-11	0.81	-10	1.04	16

It can be seen that it is difficult to match the early life behavior of the fuel and the end of life behavior of the fuel. Percent errors for end of life cladding strain are much lower than beginning of life. When fitting, end of life data took precedence because it is a limiting factor for fuel lifetime and the quality of the data is better. If all of the data points are considered, the best results are returned by the four group constant atom number version of the code. In addition to the maximum hoop strain, the axial hoop strain at 15.8 at% burnup was also compared, as it is contained within open literature. Figure 67 shows the axial hoop strain profile at 15.8 at% burnup. It can be seen that none of the cases are an exact match to the data.

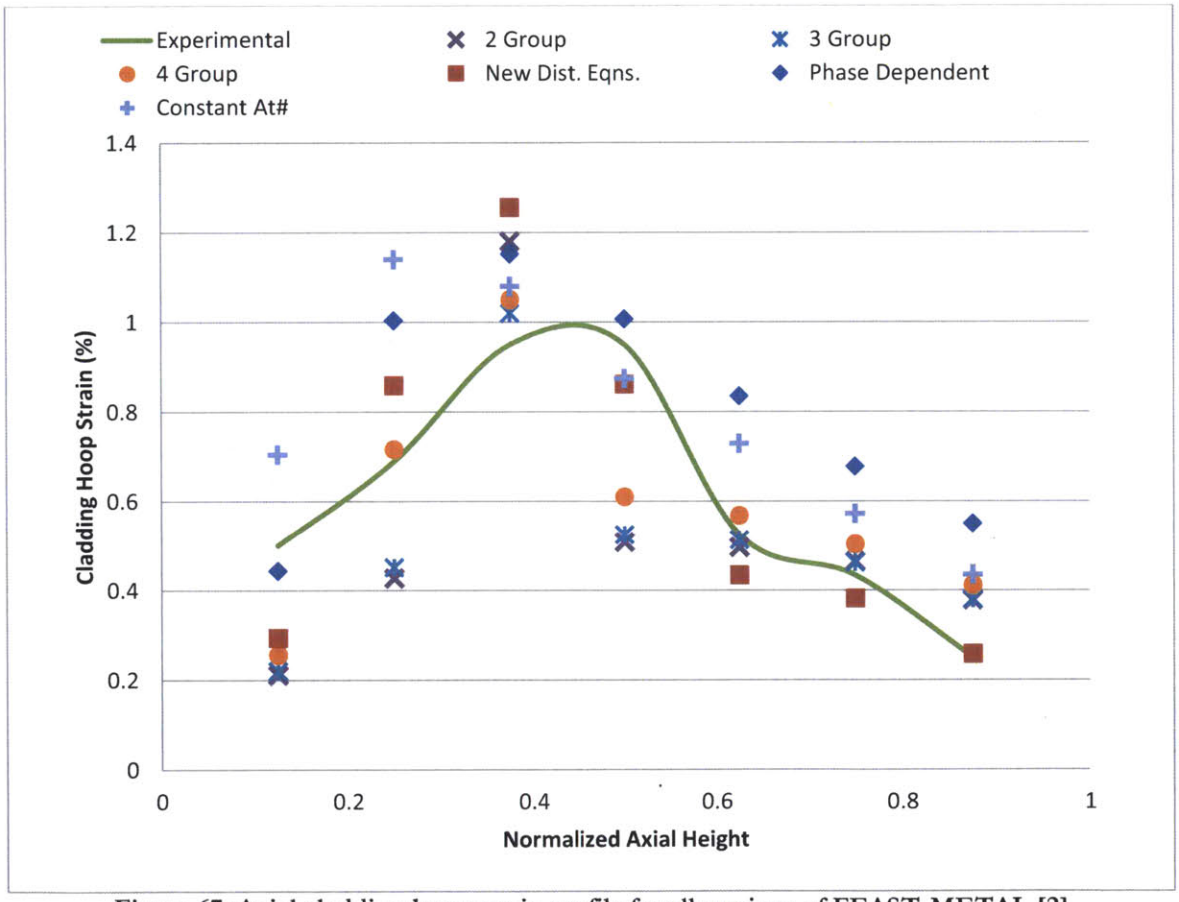

Figure 67: Axial cladding hoop strain profile for all versions of FEAST-METAL [2]

However, different trends are exhibited by the constant atom number and constant volume versions of the code. The constant volume versions of the code have a flatter axial profile with the exception of the large jump at the third axial node. The constant volume versions return generally larger strain results, especially at lower axial position. The largest difference can be seen at the second axial node. Mechanistically, this difference in profile shape may be related to the alterations in open pore compressibility, which is dependent on the phase of the fuel.

Fuel swelling plots all show the desired behavior; yet, distinct differences can be seen between the versions of the code that use a constant volume approach for bubble groups and those that use a constant atom number approach. Firstly, all versions of the code show the same solid fission product swelling behavior. This swelling increases linearly with burnup. At the beginning of life solid fission products do not make a large contribution to overall fuel swelling. At the end of life, they are the dominant factor in relation to swelling and cladding strain. All the codes also show the desired relation between open and closed porosity. Closed porosity dominates the swelling behavior of the fuel until the swelling threshold of 10%, the point at which gas begins to be released from the fuel, is reached. After this, open porosity becomes the dominant factor until the fuel becomes radially constrained by the cladding. Once the fuel is constrained, the open porosity is compressed at roughly the same rate solid fission products swelling is produced. This trend continues until the end of the irradiation. The versions differed, however, in the rate at which closed porosity was exchanged for open porosity. The constant atom versions saw the majority of closed porosity converted to open porosity in a much shorter irradiation time than the constant volume version of the code. This difference is most likely related to the alteration of the effective porosity correction factor and the open pore formation constant, which are both fitting parameters.

Since the results of the benchmarks are basically similar for each of the six versions of the codes developed, it is difficult to make a conclusion as to which is the best choice. First off, all versions of the code return decent results for fission gas release and axial elongation, so no conclusion can be based upon these results. Additionally, the maximum cladding strain results for all version of the code show reasonable results for all versions. However, the final constant atom number version of the code with the new inter-bubble distance equations has very large error at low burnup. The constant atom number version of the code without phase or distance modifications places the

maximum axial cladding strain point at the wrong location. Of the constant atom number versions, the 2-group version takes much less time to run to completion, so it is the best choice among them. In the end we have the two group constant volume version of the code and the phase dependent constant atom number version of the code as being a combination of the most valid and applicable. To choose between those versions, a third benchmark would be needed. Preferable this would be a blanket fuel case so that the validity of the alterations made to the fuel's compressibility model for the constant atom number versions of the code could be validated.

4.4. Results for Simulated Long-term Irradiation

This section contains the results obtained from the simulated long-term case, which is an approximation of the fuel which would be in the travelling wave reactor. Once again, results are summarized for cladding strain, fission gas release, fuel axial elongation and fuel swelling. While the results here cannot be used as a benchmark, they can show how the different versions predict the behavior of breeder fuel over its entire lifetime. The results for all six versions are presented on the same plot so that the differences can be seen clearly. For fuel swelling, only the two group constant volume version and the phase dependent version are presented since they are indicative of how constant atom number and constant atom number versions behave differently. Maximum hoop cladding strain for all six versions of the code is shown in Figure 68.

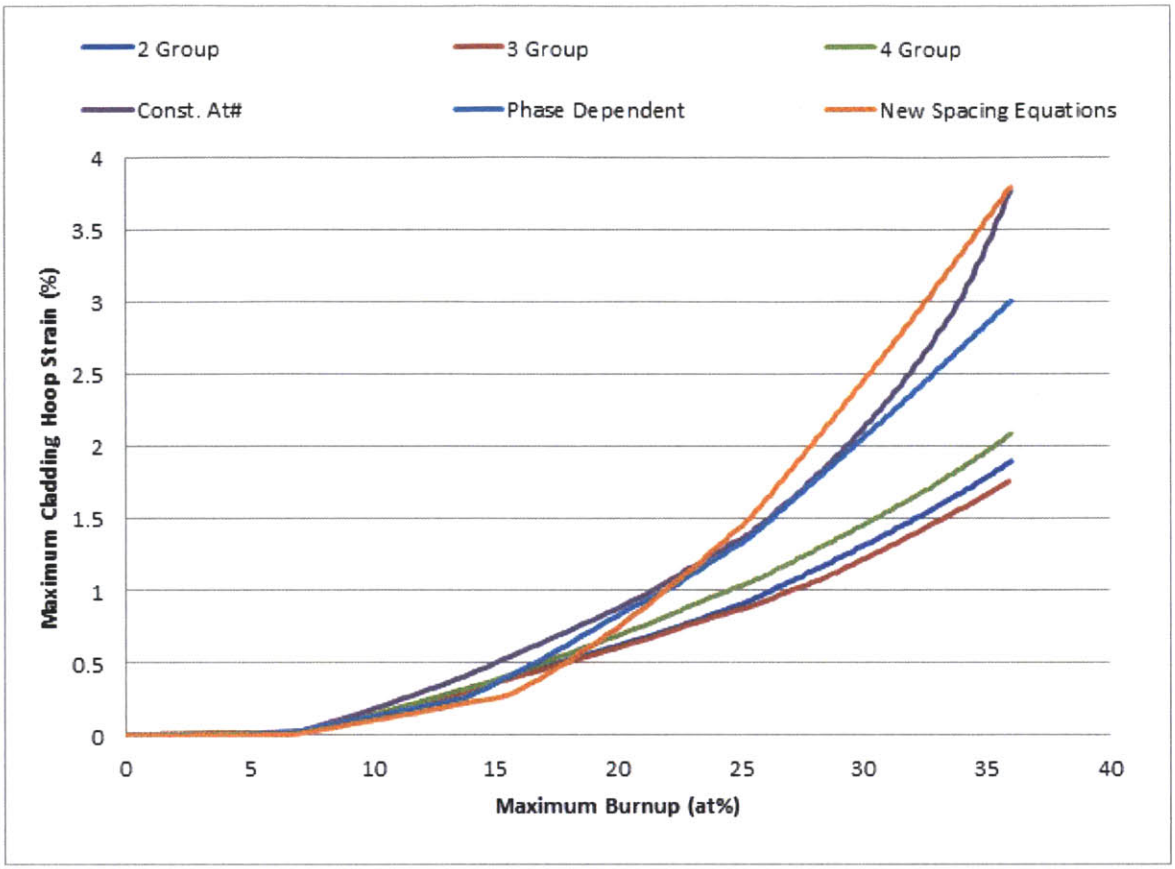

Figure 68: Comparison of maximum cladding hoop strain results for the sample long-term case (the 2/3/4 group designations all refer to constant volume versions of FEAST-METAL)

It can clearly be seen that the constant atom number versions of the code return much higher cladding strain predictions than the constant volume version of the code. This is a significant issue because cladding strain can become the principal limitation on fuel burnup. As is demonstrated in the next chapter of this thesis, the difference between these versions' results can be attributed to the inclusion of the effective porosity correction factor, which makes the fuel less compressible.

The fission gas release results for this case can be seen in Figure 69. No significant differences can be seen in the end of life fractional release. All versions return ~95% release fraction and follow experimental trends.

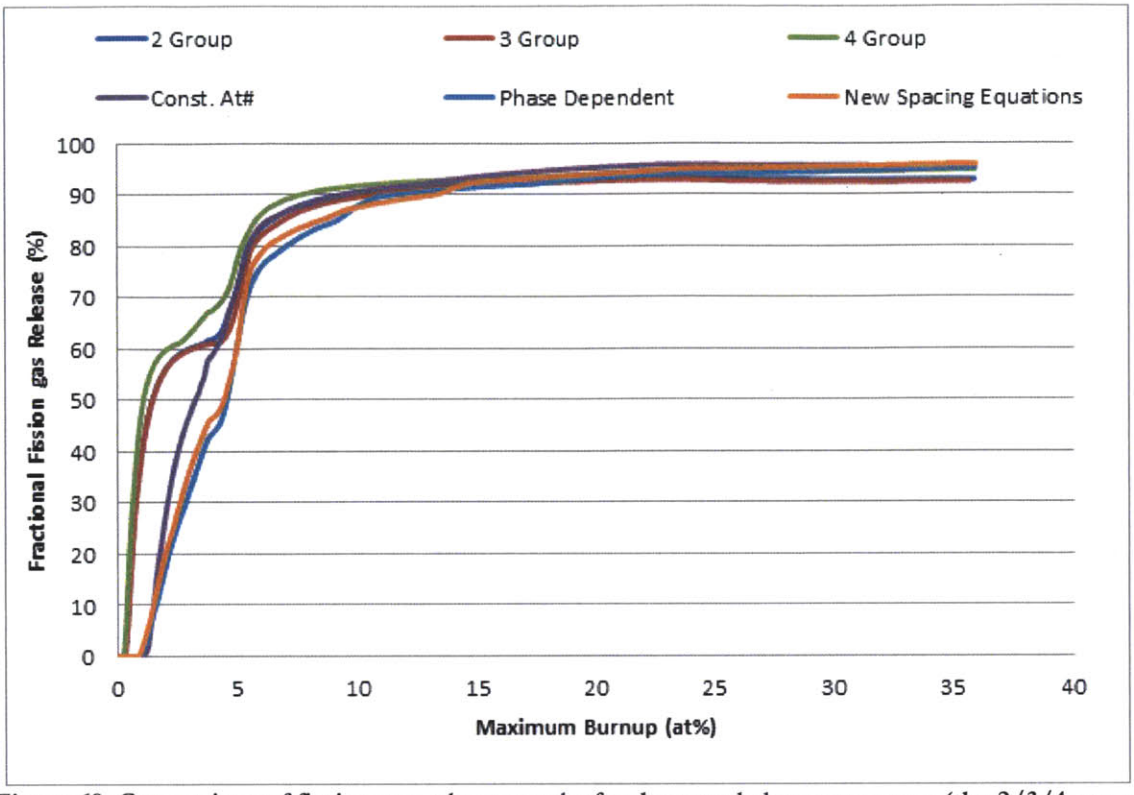

Figure 69: Comparison of fission gas release results for the sample long-term case (the 2/3/4 group designations all refer to constant volume versions of FEAST-METAL)

Similar to the cladding strain plots, large differences can be seen in the fuel axial elongation predictions that are returned by the different versions of FEAST-METAL. Figure 70 shows these differences.

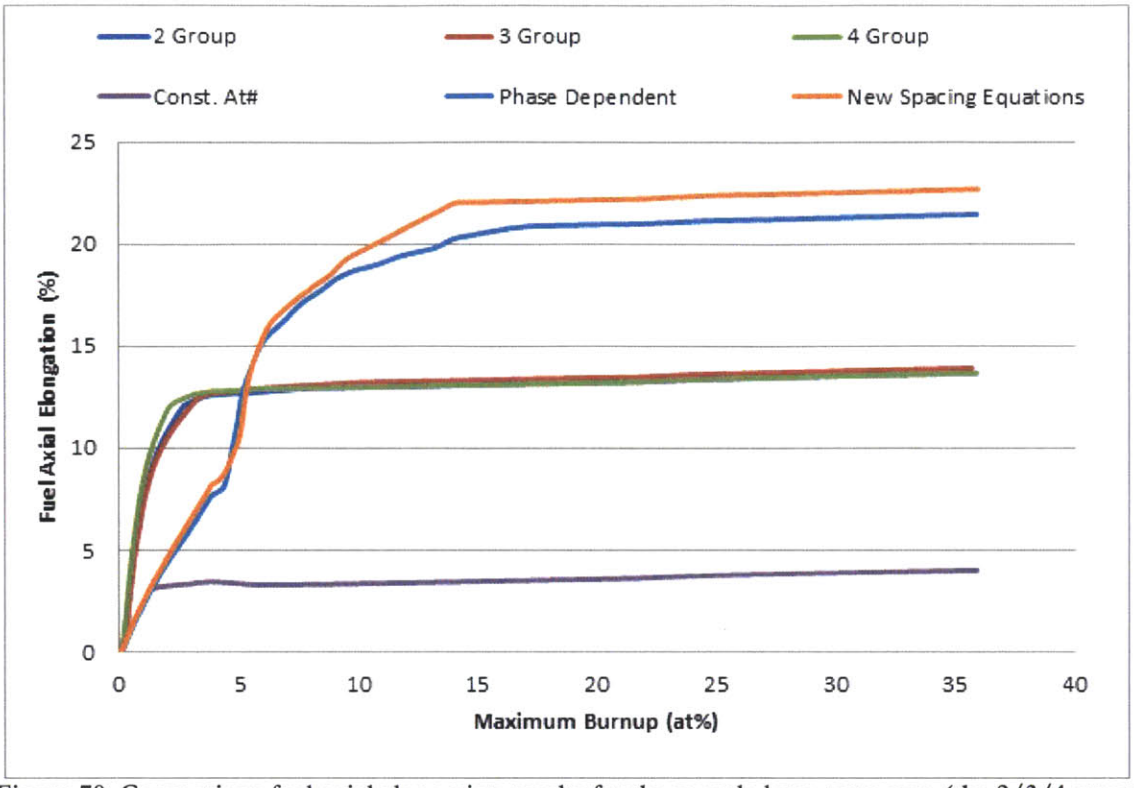

Figure 70: Comparison fuel axial elongation results for the sample long-term case (the 2/3/4 group designations all refer to constant volume versions of FEAST-METAL)

For all of the constant volume versions of the code, the results obtained for axial elongation are very similar. This is because the code algorithm for all three is the same. Among the constant atom versions of the code, a very large variation can be seen in the behavior of the different versions. This is most likely attributable to the successive changes that were made in the algorithm of the fission gas and swelling module. Differences may also have arisen from alterations in the fitting factors used in matching code results for anisotropic deformation to experimental results. In order to benchmark axial elongation, all of the cases used were developed through alterations made to the X425 and X430 cases. Because of this, it may be hard to apply the igniter fuel benchmarks to blanket fuel.

Fuel swelling plots of the code predictions are provided for the two group constant atom number and the two group phase dependent version of the code. Figure 71 shows the constant atom number version, and Figure 72 shows the constant volume version. Little difference can be seen between the overall trends displayed here beyond those discussed in the previous section. The large difference in overall swelling can be seen as large contributor to the increase in the strain of the

cladding (which can be seen in Figure 68) from the constant atom version of the code in comparison to the constant atom number version of the code. The very large amount in fuel swelling seen in all versions of the code (from 65% to 85%), for these long-term irradiation cases, is a result of low initial fuel smear density, which is only 60%. In comparison, the X425 benchmark has an initial smear density of 72% and only swells to ~40%. Additionally, the long-term case becomes fully restrained by the cladding until ~10 at% burnup. EBR-II cases become fully restrained by ~7 at%. This difference can also be seen as a result of the fuel's initial smear density.

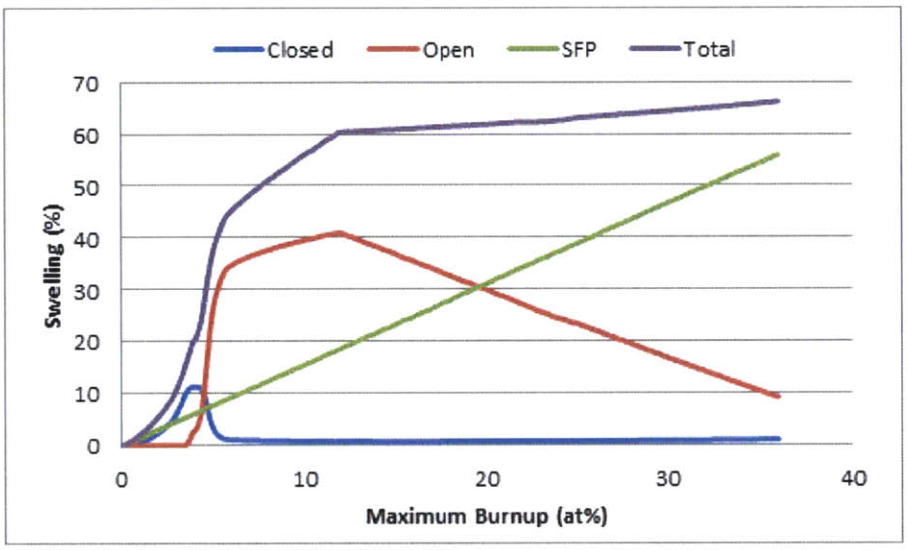

Figure 71: Fuel swelling at 0.37 normalized axial height for the long-term case using the 2 group constant volume version of FEAST-METAL

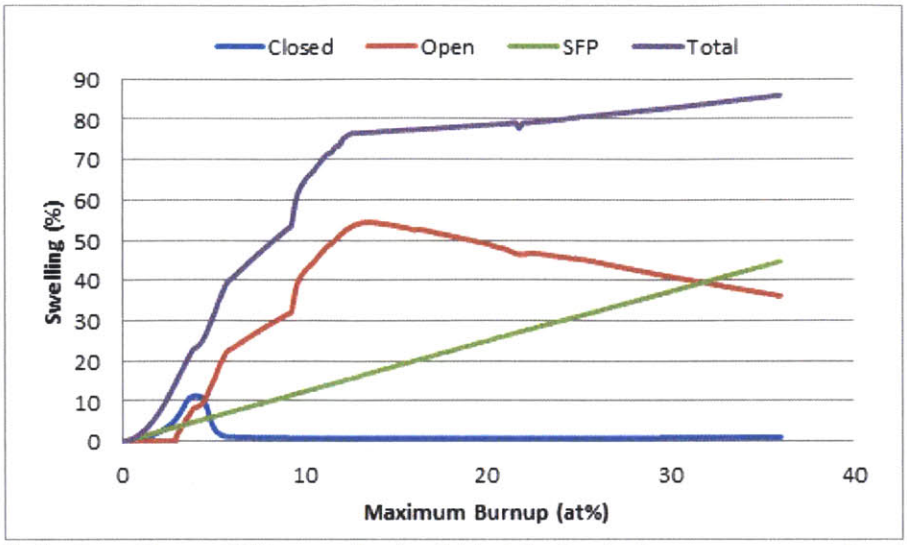

Figure 72: Fuel swelling at 0.37 normalized axial height for the long-term case using the phase dependent constant atom number version of FEAST-METAL

Based on these results, it appears that fuel under similar irradiation conditions should be able to survive in a reactor for this specified period. To make this determination, a cladding creep strain limit of 3% was used. After this point, cladding strain increases at a much higher rate. Since all fission gas is released to the plenum and axial elongation can be accounted for through effective fuel design, cladding strain is the limiting parameter. The constant volume versions of the code and the phase dependent version of the code indicate that this is possible. However, the dose to the clad is so high that maintenance of HT-9's favorable mechanical properties is in doubt. There is no data for irradiations of blanket material publicly available.

5. Sensitivity Studies Performed on Physical Factors, Fitting Factors and Code Input Parameters

The different models developed all make use of the same four fitting factors which are the diffusion constant, the open bubble formation constant, the surface area correction factor and the effective porosity correction. This section shows the sensitivity of the results of FEAST-METAL for variations of these factors. To perform each analysis, the relevant fitting factor was varied within the range of physical applicability and the other fitting factors correspond to the values obtained for the benchmarks explained in the previous chapter. Analyses were performed for the 4-group constant volume version and phase dependent version with the original distance equations. The studies were performed using the X425 EBR-II irradiation case detailed in the previous chapter. The equations which contain the fitting factors are included in each section, while their relation to the entire program can be seen in Chapter 2. Both the maximum cladding hoop strain and the fission gas release fraction are included for each analysis since these are the main parameters that are used to benchmark the code. Though the impact of these constants on the fission gas and swelling modules of the code can be seen in the fuel swelling plots, these plots are not as good of a measure of macroscopic behavior as cladding strain predictions, for which measurements exists. The importance of each factor and implications of the results are discussed. Plots that do not contain values to the full 18.9 at% burnup failed due to the alteration of fitting factors.

In addition to these sensitivity studies, the dependence of the code on the number (i.e. resolution) of axial nodes is examined. The cladding strain, at both 15.8 at% burnup and end of life, as well as the fractional fission gas release is compared using 7, 14 and 20 axial nodes. This study is performed for three separate versions of the code: the 2-group constant atom number, the 2-group constant atom number and the 2-group phase dependent version.

For each version of the code, the dependence of the results on the time step is examined. This is done using 7, 14 and 20 axial nodes to determine if there is any inter-dependence between axial resolution and the maximum length of a time-step. The time-steps analyzed ranged from 10 to 50 seconds in 5 second intervals.

This chapter also includes a runtime linearity analysis and a comparison of FEAST-METAL with the CAFÉ code, which is a merger of FEAST-METAL and COBRA-IV. [23]

5.1. Diffusion Constant

The diffusion constant controls the rate at which fission gas and fission gas bubbles move through the fuel matrix. Thus, it impacts both the formation of gas bubbles and their release to the plenum. It has a large influence on both fuel swelling and fission gas release. For the phase dependent version of the code, sensitivity studies were performed on both the low temperature and high temperature diffusion coefficients. The value of the diffusion constant for each study can be seen in Table 17.

Table 17: Diffusion constant sensitivity studies

Study	Case A	Case B	Case C	Case D	Case E
4-Group Diffusion Constant	0.3E-03	1.5E-03	3.0E-03	6.0E-03	15.0E-03
Phase Dependent Low Temperature Diffusion Constant	0.2E-04	0.5E-04	1.0E-04	2.0E-04	5.0E-04
Phase Dependent High Temperature Diffusion Constant	0.06E-08	0.15E-08	0.3E-08	0.6E-08	1.5E-08

The results of the study on the 4-group version of the code can be seen in Figure 73 and Figure 74. For this version of the code, the diffusion constant takes the form of Equation 124.

$$D_g = D_{g0} \exp\left(-\frac{Q_g}{RT}\right) \qquad \text{Eqn. 124}$$

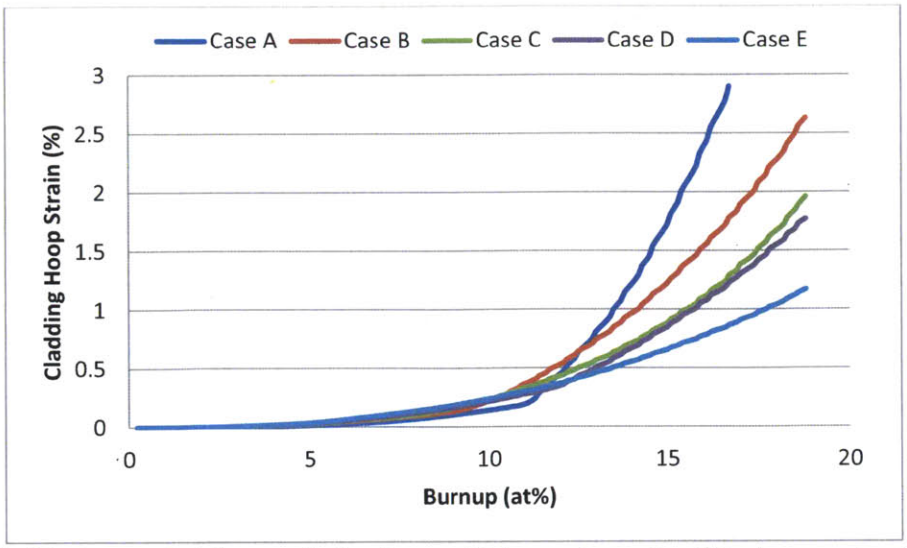

Figure 73: Maximum cladding strain for the sensitivity study on the diffusion constant for the 4-group model

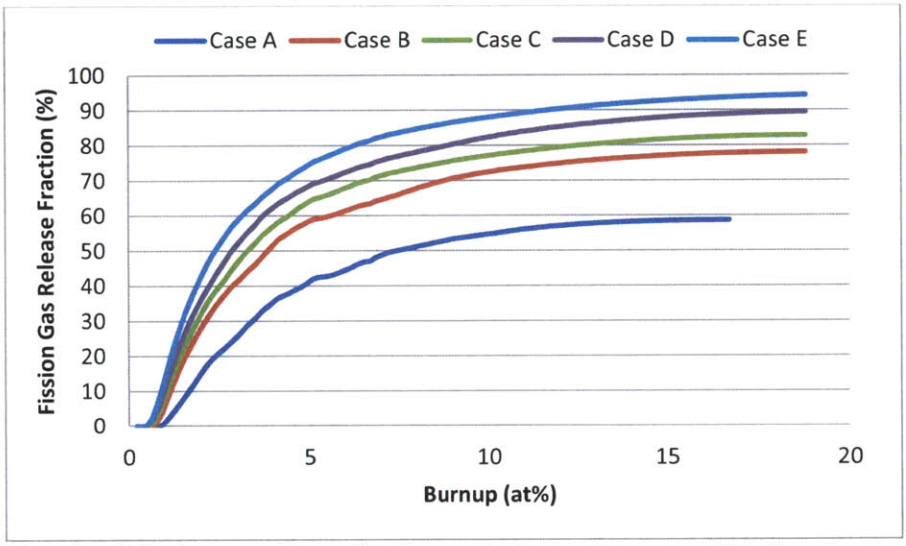

Figure 74: Fractional fission gas release for the sensitivity study on the diffusion constant for the 4-group model

For the constant volume version of the code, it can clearly be seen that as the diffusion constant increases, the fractional fission gas release increases correspondingly. This is logical because if the fission gas is more mobile, then it can diffuse to the plenum at a greater rate. An inverse relation between this constant and cladding strain can be seen. If more fission gas is retained in the fuel, which occurs because of a lower diffusion factor, then the cladding strain will increase. This is

because the gas in the fuel can only be compressed so far. In fact, a diffusion constant that is too low will cause enough strain to cause failure.

The results of the study on the high temperature diffusion constant for the phase dependent version of the code can be seen in Figure 75 and Figure 76. For this version of the code, the diffusion constant takes the form of Equation 125 where T_γ is the temperature above which the gamma phase exists.

$$D_g = \begin{cases} \mathbf{1.0 \times 10^{-4}\ exp\left(-\frac{5200}{RT}\right)} & T < T_\gamma \\ \mathbf{0.3 \times 10^{-8}\ exp\left(-\frac{28500}{RT}\right)} & T > T_\gamma \end{cases} \qquad \text{Eqn. 125}$$

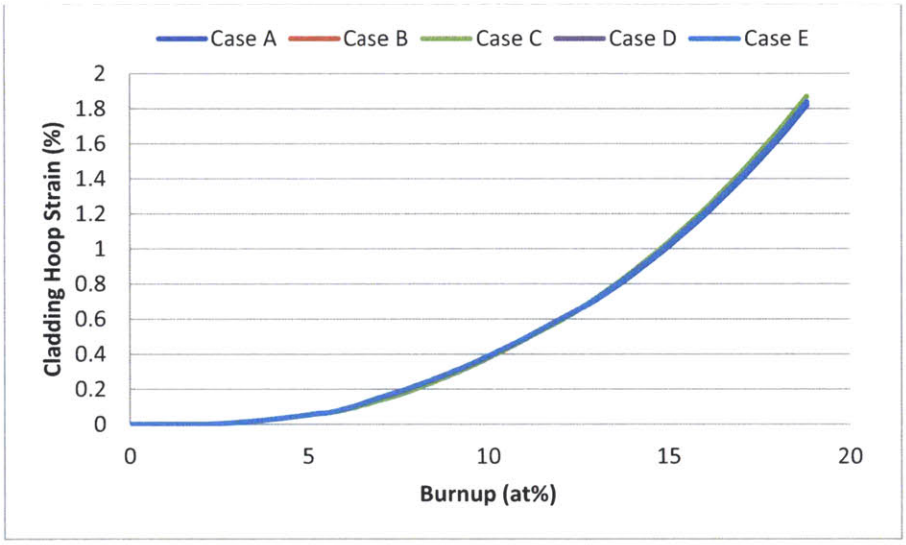

Figure 75: Maximum cladding strain for the sensitivity study on the high temperature diffusion constant for the phase dependent version

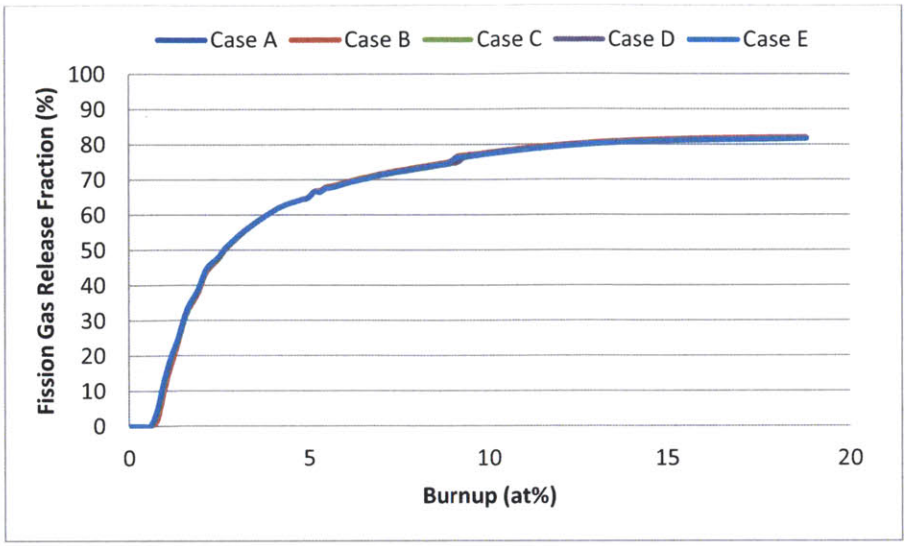

Figure 76: Fractional fission gas release for the sensitivity study on the high temperature diffusion constant for the phase dependent version

From the results, it can be seen that neither the cladding strain nor the fission gas release fraction have a significant dependence on the high temperature diffusion constant for the range of applicable values. The relatively low importance of this fitting factor is due to the fact that the higher temperature diffusion coefficient is much higher than the low temperature one when the temperature variable is taken into account. This follows experimental results, which show that the high temperature gamma phase has a much higher diffusion coefficient. The results of the study of the low temperature diffusion constant for the phase dependent version of the code can be seen in Figure 77 and Figure 78.

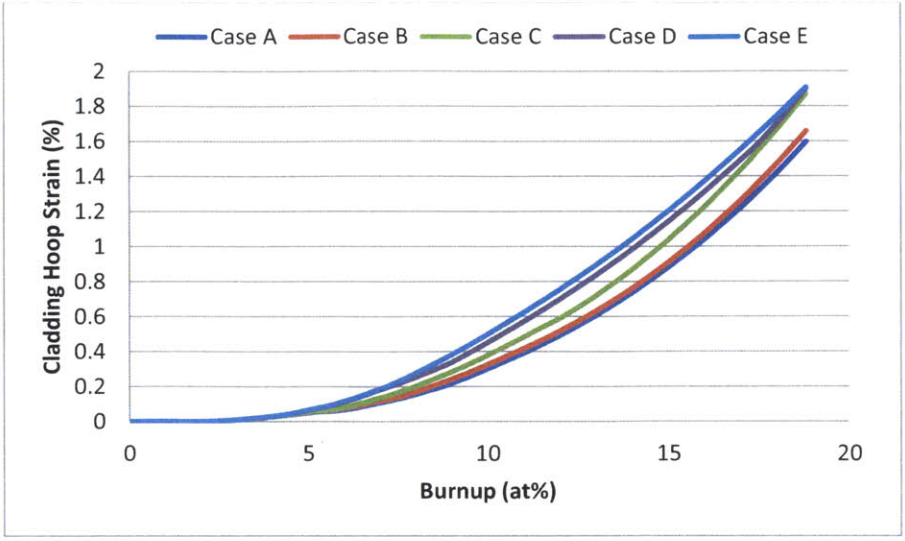

Figure 77: Maximum cladding strain for the sensitivity study on the low temperature diffusion constant for the phase dependent version

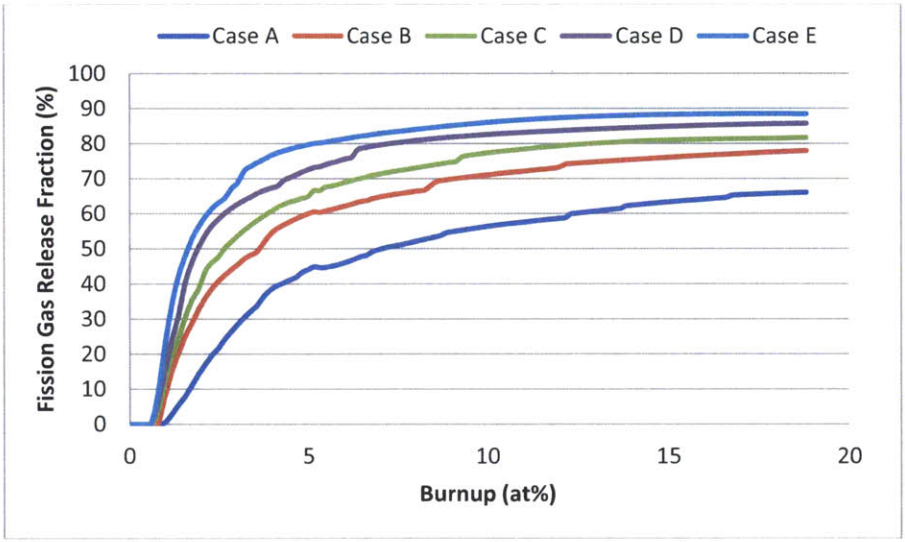

Figure 78: Fractional fission gas release for the sensitivity study on the low temperature diffusion constant for the phase dependent version

The results from the low temperature diffusion constant study show the same trends as the 4-group constant volume study. However, both cladding strain and fission gas release are dependent on the amount of gas retained in the fuel.

5.2. Open Pore Formation Constant

The rate at which open pores are formed from closed bubbles is dependent on the open pore formation constant and the distance between bubbles. This relation can be seen in Equation 126, where P_{ij} is the probability of bubble coalescence over a given time.

$$P_{ij} = \frac{\Delta r_{bi}}{d_l l_j} \qquad \textbf{Eqn. 126}$$

d_l: Open bubble formation coefficient (fitting factor)

l_j: Average distance between bubbles

The parameters used to determine the effect of this parameter on the code results can be seen in Table 18.

Table 18: Open pore formation constant sensitivity studies

Study	Case A	Case B	Case C	Case D	Case E
4-Group Open Pore Formation Constant	0.1	0.25	0.5	0.75	-
Phase Dependent Open Pore Formation Constant	0.1	0.25	0.5	0.75	1.0

Using these values, the results for the sensitivity study on the 4 bubble group version of the code can be seen in Figure 79 and Figure 80.

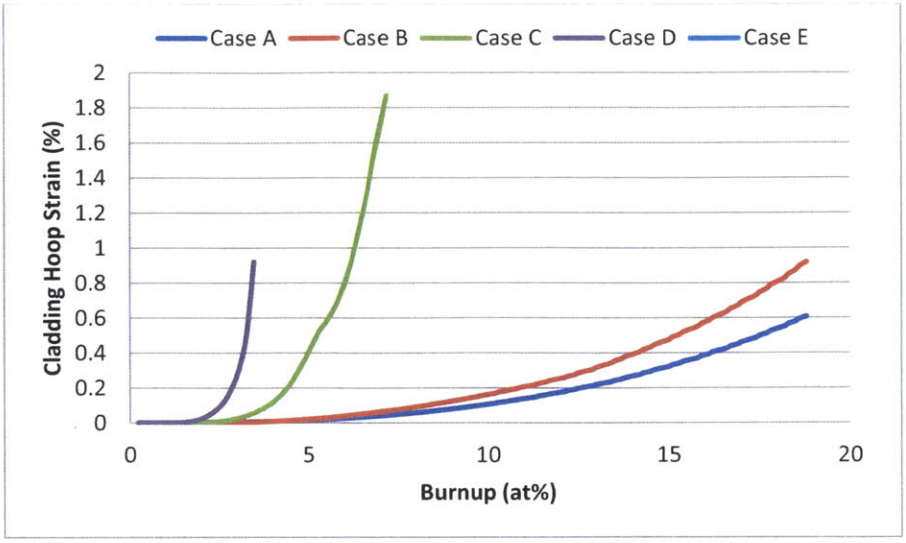

Figure 79: Maximum cladding strain for the sensitivity study on the open pore formation constant for the 4-group version

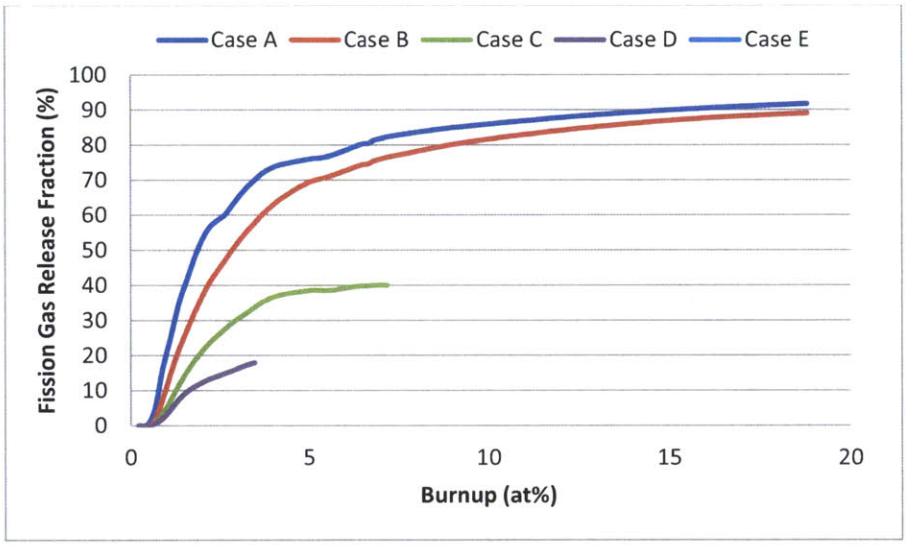

Figure 80: Fractional fission gas release for the sensitivity study on the open pore formation constant for the 4-group version

Likewise, the results for the sensitivity study on the phase dependent version of the code can be seen in Figure 81 and Figure 82.

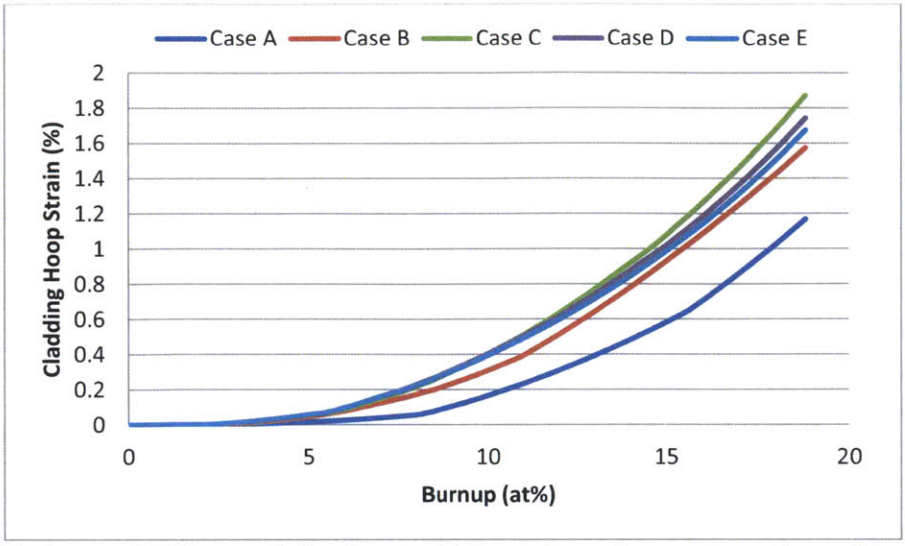

Figure 81: Maximum cladding strain for the sensitivity study on the open pore formation constant for the phase dependent version of the code

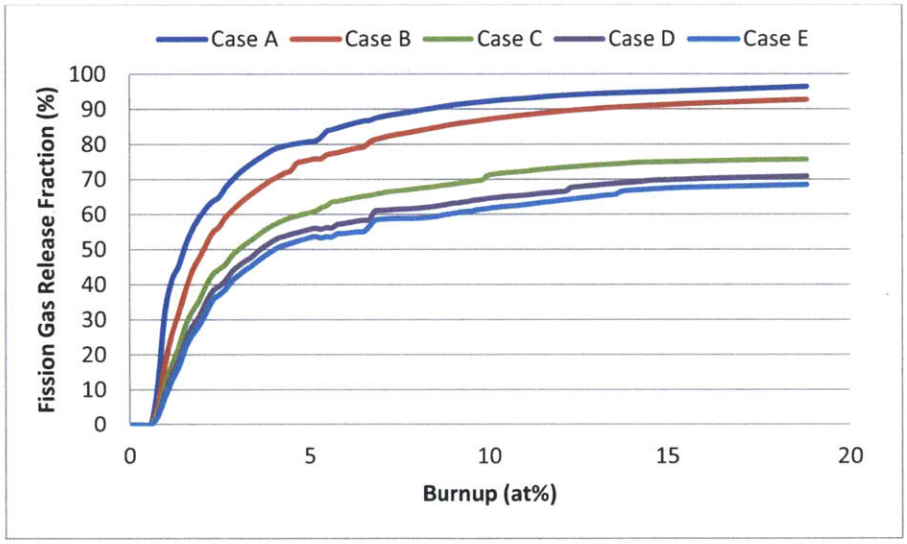

Figure 82: Fractional fission gas release for the sensitivity study on the open pore formation constant for the phase dependent version of the code

Both constant volume and the constant atom number versions of the code show the same trends in the behavior of fission gas. As the open pore formation constant increases, the fractional fission gas release decreases. This is because the probability of a bubble becoming an open pore is inversely dependent on this parameter. The overall cladding strain increases as this parameter increases since more fission gas is retained in the fuel as the parameter increases. For the constant atom number

version of this code, there is a maximum value, but the general trend is the same as for the constant volume version of the code.

5.3. Surface Area Correction Factor

The change in the surface area of bubbles when they become open pores is accounted for by the open pore formation constant. This parameter for physical reasons can only be between 0 and 1. The values of the parameter used in the study can be seen in Table 19. The factor equation for this factor can be seen in Equation 127.

$$A_3 = f_{th} f_s (A_1 + A_2) \qquad \text{Eqn. 127}$$

f_{th}: Fraction of closed bubbles that interconnect when swelling threshold is reached

f_s: Fractional surface area of a closed bubble after interconnection with open bubbles

Table 19: Surface area correction factor sensitivity studies

Study	Case A	Case B	Case C	Case D	Case E
4-Group Surface Area Correction Factor	0.1	0.25	0.5	0.75	1.0
Phase Dependent Surface Area Correction Factor	0.1	0.25	0.5	0.75	1.0

The results of the study for the 4-group version of the code can be seen in Figure 83 and Figure 84.

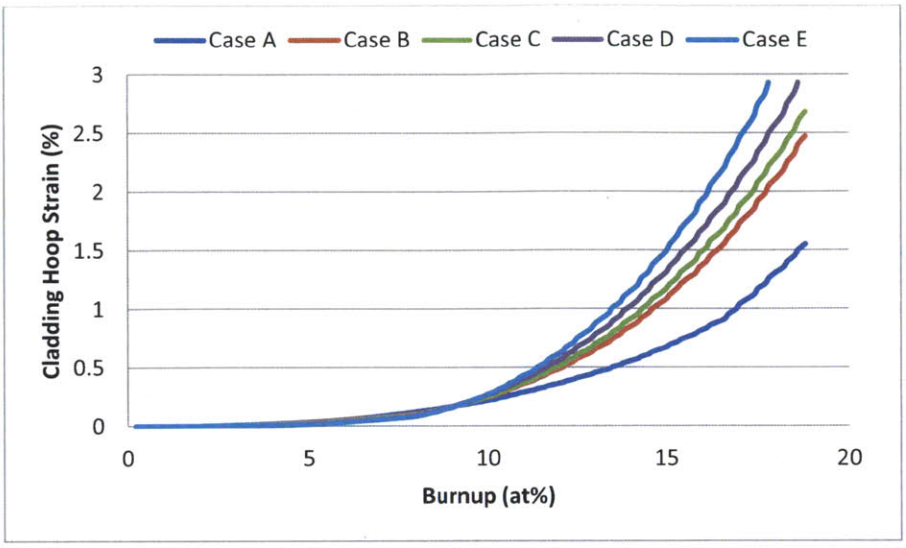

Figure 83: Maximum cladding strain for the sensitivity study on the surface area correction factor for the 4- group version of the code

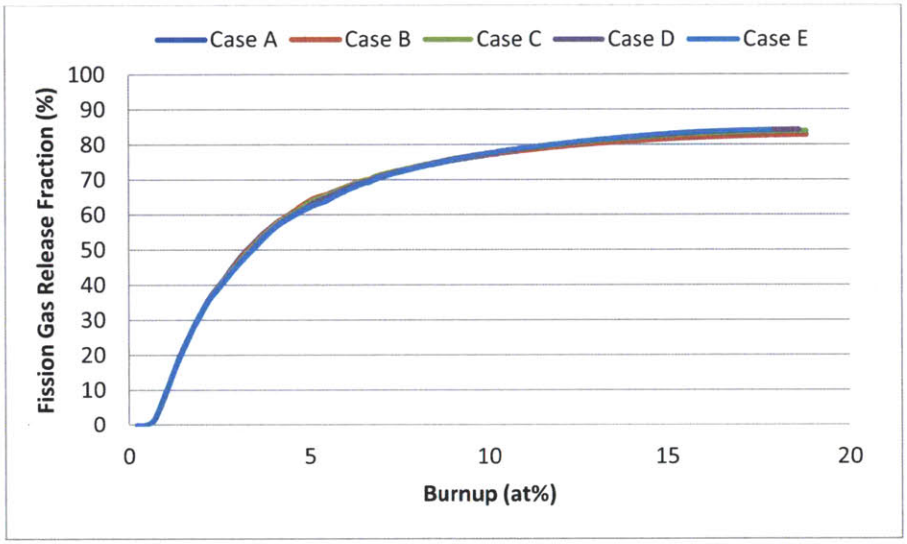

Figure 84: Fractional fission gas release for the sensitivity study on the surface area correction factor for the 4- group version of the code

For the constant atom number version of the code, the cladding strain increases as this fitting factor increases. However, the fission gas release fraction is independent of this factor. These trends are not mirrored in the phase dependent version of the code. The results for the phase dependent version can be seen in Figure 85 and Figure 86. In this version of the code the cladding strain shows the opposite behavior and increases as the fitting factor decreases. Additionally, the fission gas release fraction decreases as this factor decreases. It is unclear whether or not these differences are a

result of the use of a constant atom number algorithm or the incorporation of phase dependence into the code.

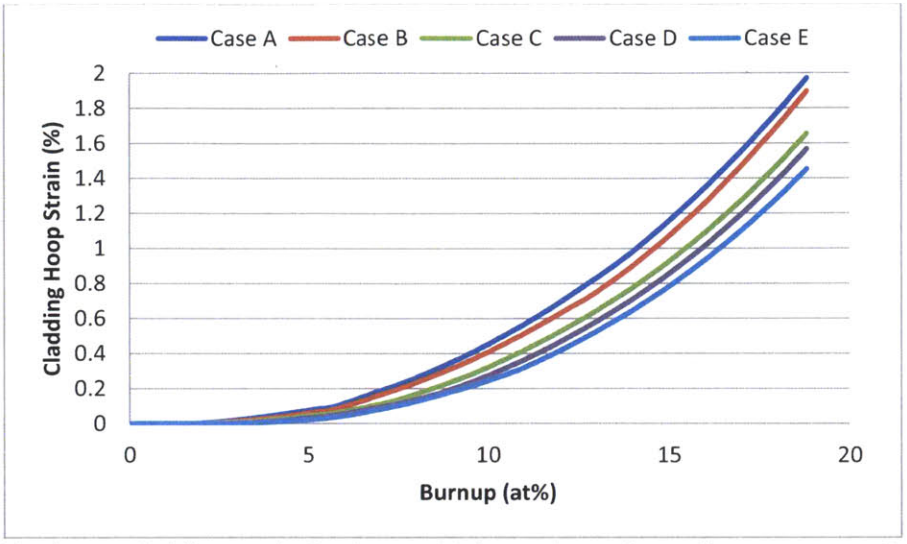

Figure 85: Maximum cladding strain for the sensitivity study on the surface area correction factor for the phase dependent version of the code

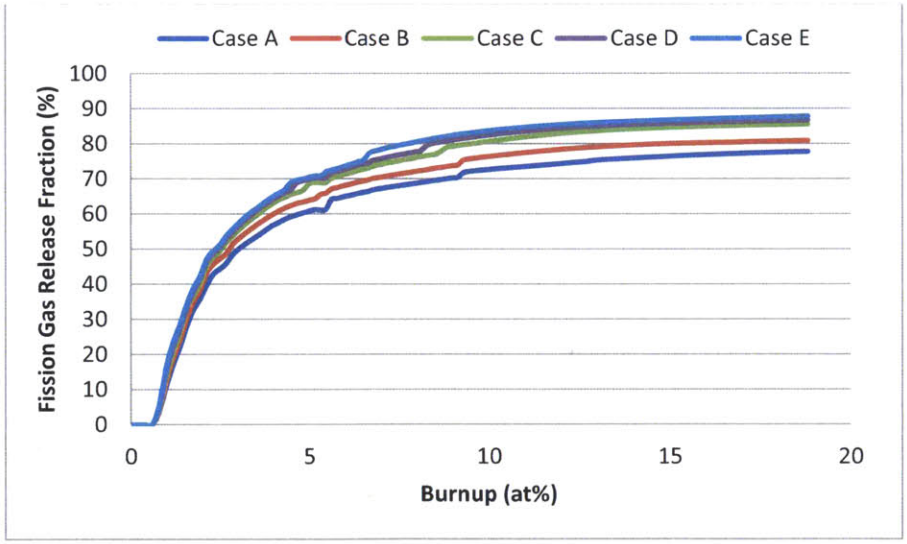

Figure 86: Fractional fission gas release for the sensitivity study on the surface area correction factor for the phase dependent version of the code

5.4. Effective Porosity Correction

The effective porosity correction adjusts the compressibility of fission gas bubbles based on the phase of the fuel. The parameters for the study can be seen in Table 20, while Equation 128 shows the effect of this parameter.

$$\alpha_c = \begin{cases} 0 & \epsilon_{sw}^{opn} = 0 \\ C\frac{1}{6}\left(\epsilon_{sw}^{opn}\right)^{1.5} & 0 < \epsilon_{sw}^{opn} < 0.1 \\ \frac{1}{6} & 0.1 > \epsilon_{sw}^{opn} \end{cases} \qquad \text{Eqn. 128}$$

ϵ_{sw}^{opn}: Open pore swelling (fraction)

α_c: Open porosity compressibility factor

C: Effective porosity correction - fitting factor

Table 20: Effective porosity correction sensitivity study

Study	Case A	Case B	Case C	Case D	Case E
Phase Dependent Effective Porosity Correction	0.2	0.4	0.6	0.8	1.0

Overall, as this fitting factor increases, the general trend shows that the cladding strain decreases. This is because the fission gas is more compressible, leading to less strain. Because the fission gas release module is independent of this factor, there is little impact on the results. These results can be seen in Figure 87 and Figure 88. Case C shows that it is possible for the creation of local minima and maxima to arise from the use of this parameter.

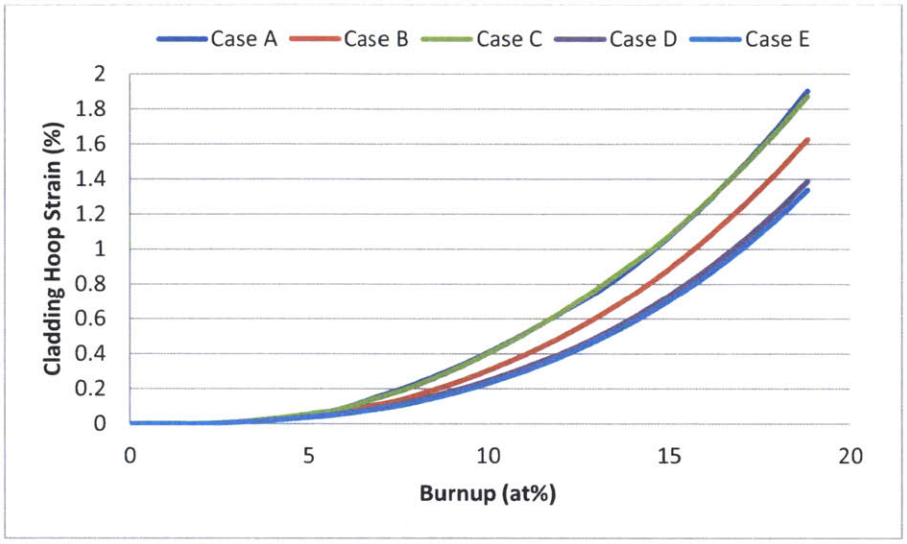

Figure 87: Maximum cladding strain for the sensitivity study on the effective porosity correction for the phase dependent version of the code

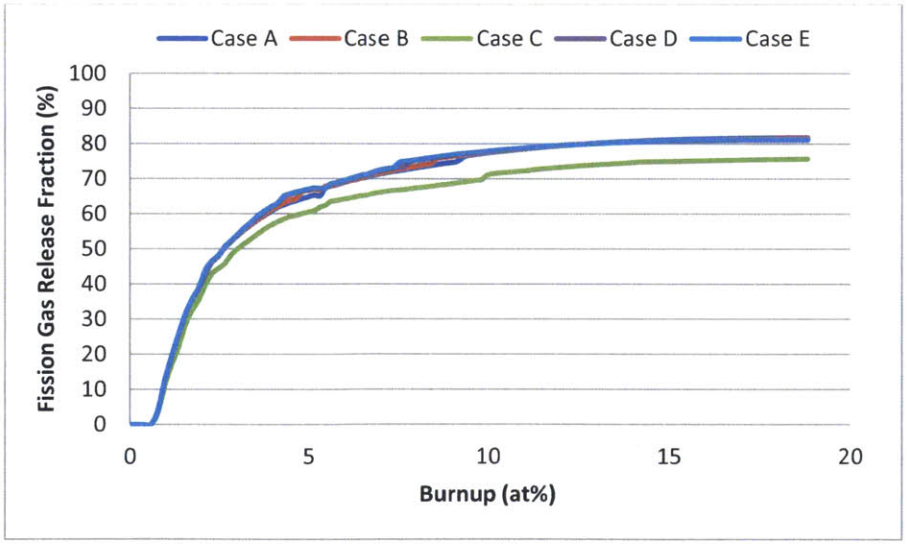

Figure 88: Fractional fission gas release for the sensitivity study on the effective porosity correction for the phase dependent version of the code

5.5. Time-step and Axial Resolution Dependence

The user specified time-step determines the frequency at which mechanical calculations are performed by the code. In order to determine the variability in code results from the time step used, three separate versions of the code were tested with 7, 14 and 20 axial nodes for time steps from 10 to 50 seconds in intervals of 5 seconds. Table 21, Table 22 and Table 23 show whether or not the code runs to completion with a given time step.

Table 21: Time-step stability analysis of three versions of FEAST-METAL using 7 axial nodes (running to completion is denoted by a "Y", otherwise code failure mechanism is noted)

Time Step (s)	Constant Atom Number	Phase Dependent	Constant Volume
10	Y	Y	Y
15	Y	Y	Y
20	Y	Y	Y
25	Y	Y	Y
30	Y	Y	Y
35	Irradiation Creep	All Clad Wastage	Y
40	Irradiation Creep	Irradiation Creep	Irradiation Creep
45	Irradiation Creep	Irradiation Creep	Irradiation Creep
50	Irradiation Creep	Irradiation Creep	Irradiation Creep

Table 22: Time-step stability analysis of three versions of FEAST-METAL using 14 axial nodes (running to completion is denoted by a "Y", otherwise code failure mechanism is noted)

Time Step (s)	Constant Atom Number	Phase Dependent	Constant Volume
10	Y	Y	Y
15	Y	Y	Y
20	Y	Y	Y
25	Y	Y	Y
30	Y	Y	Y
35	Irradiation Creep	All Clad Wastage	All Clad Wastage
40	Irradiation Creep	Irradiation Creep	Temperature out of Range
45	Irradiation Creep	Irradiation Creep	Irradiation Creep
50	Irradiation Creep	Irradiation Creep	Irradiation Creep

Table 23: Time-step stability analysis of three versions of FEAST-METAL using 20 axial nodes (running to completion is denoted by a "Y", otherwise code failure mechanism is noted)

Time Step (s)	Constant Atom Number	Phase Dependent	Constant Volume
10	Y	Y	Y
15	Y	Y	Y
20	Y	Y	Y
25	Y	Y	Y
30	Y	Y	Y
35	Irradiation Creep	All Clad Wastage	Y
40	Irradiation Creep	Irradiation Creep	Irradiation Creep
45	Thermal Creep	Thermal Creep	Irradiation Creep
50	Thermal Creep	Thermal Creep	Irradiation Creep

All three versions of the code showed that the maximum time step that can be used consistently is 30 seconds. Beyond this, numerical stability problems lead the code to fail unpredictably. The reason for code failure is primarily instability in the irradiation creep module. However, similar problems are seen in the thermal creep and clad wastage modules. In order to avoid these problems, it is recommended to use a time step of 25 seconds or less. Cladding strain and fractional fission gas release at end of life are compared as a function of time step and the number of axial nodes in Table 24 and Table 25. 7, 14 and 20 axial nodes are compared using time steps from 15 to 30 seconds for the 2-group constant volume version of the code and the 2-group phase dependent version of the code.

Table 24: Cladding strain (in terms of percentage - %) at 18.9 at% burnup for the X425 assembly from EBR-II with varying time-steps and number of axial nodes

Time Step (s)	Constant Volume			Phase Dependent		
	7 Nodes	14 Nodes	20 Nodes	7 Nodes	14 Nodes	20 Nodes
15	2.19	2.27	2.46	1.8	1.80	1.82
20	2.19	2.27	2.48	1.81	1.77	1.83
25	2.19	2.27	2.48	1.83	1.80	1.84
30	2.19	2.27	2.48	1.84	1.80	1.82

Table 25: Fraction fission gas release (in terms of percentage-%) at 18.9 at% burnup for the X425 assembly from EBR-II with varying time-steps and number of axial nodes

Time Step (s)	Constant Volume			Phase Dependent		
	7 Nodes	14 Nodes	20 Nodes	7 Nodes	14 Nodes	20 Nodes
15	81.4	80.0	79.9	81.8	81.6	80.5
20	81.5	80.0	79.9	81.7	81.7	80.4
25	81.4	80.0	79.9	81.5	81.0	80.2
30	81.4	80.0	79.9	81.3	80.8	80.1

Neither version of the code showed large variances in results as a function of time-step. It can be seen that in the phase dependent version of the code, there is little variance in the results returned when the number of nodes is increased. However, in the constant volume version of the code, the maximum cladding strain seemingly increases. In order to characterize the origin of this difference, cladding strain as a function of normalized axial height is examined for both the constant volume and phase dependent versions at 15.8 at% burnup. These analyses can be seen in Figure 90 and Figure 89.

Figure 89: Cladding hoop strain for the constant volume version of FEAST-METAL at 15.8 at% burnup for 20 second time-steps

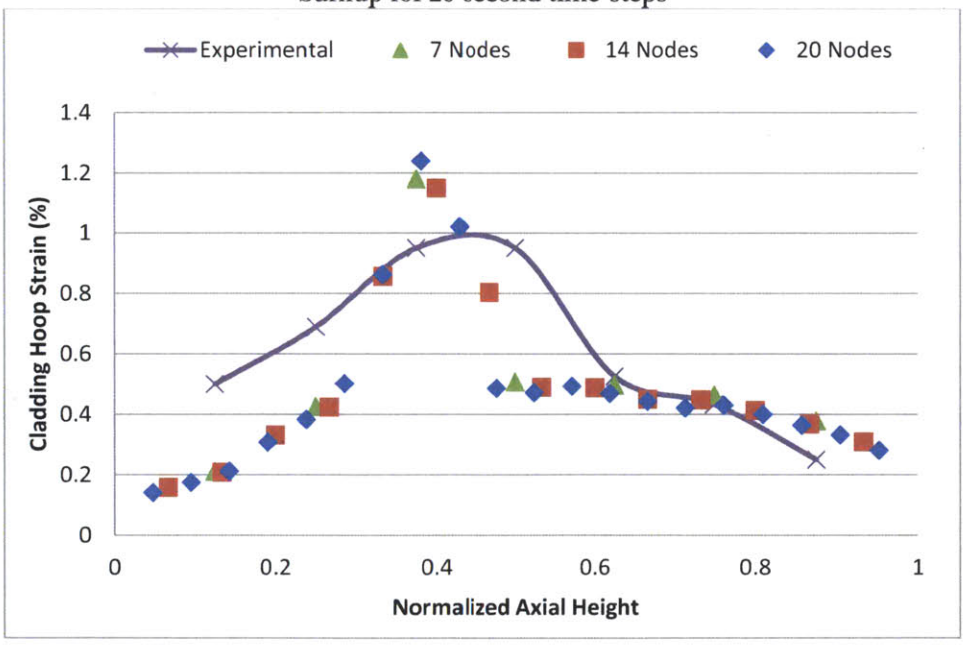

Figure 90: Cladding hoop strain for the phase dependent version of FEAST-METAL at 15.8 at% burnup for 20 second time-steps

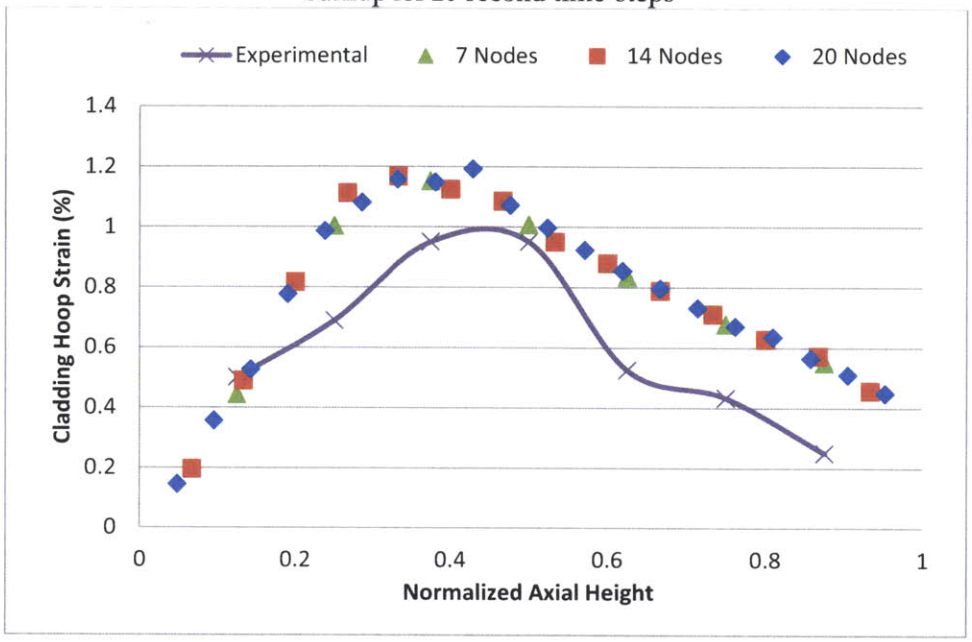

Comparing the results for the nodal characterization of both versions of the code, it can be seen that for both versions the general trend of the results is the same. However, with more nodes the actual maximum of the results is better characterized. This indicates that behavior can be mischaracterized if too few data points are used. It is best to use an axial resolution not much larger than 7-10% of axial height to ensure axial behavior is well characterized. In comparison to the phase dependent version, the constant volume version of the code shows a discontinuity in the behavior of cladding strain near the maximum. This discontinuity occurs between a normalized axial height of 0.3 and 0.5. Other portions of the cladding hoop strain curve show much lower strains. This local peaking is possibly a result of numerical inflexibility in terms of fission gas bubble size. It may also be a result of the fact that this version of the code does not model differences in fuel plasticity and permeability to fission gas, which become a major issue in the axial region where the fuel is transitioning to the γ-phase from lower temperature phases. The phase dependent version, in which fission gas bubble behavior (in particular bubble size, compressibility and diffusion constant) has a higher dependency on temperature and pressure, shows a relaxation in this phenomenon. In this version, the 0.3-0.5 axial region follows the trend of the rest of the curve.

5.6. Comparison of FEAST-METAL with the CAFÉ code

The computer code CAFÉ is a combination of fuel code FEAST-METAL and the sub-channel analysis code COBRA-IV. [23] It was developed by Joe Fricano at MIT for the analysis of sodium fast reactor fuel. CAFÉ uses COBRA-IV to determine the behavior of the coolant axially and radially. This output is then used as an input for FEAST-METAL, since the axial variation of coolant temperature with time is one of the necessary inputs. [23] In contrast to this, FEAST-METAL (used alone) interpolates the coolant temperature based only on the inlet and outlet temperatures of the sub-channel and the pin-power, assuming no radial mass exchange with adjacent sub channels. Figure 91compares the results returned by CAFÉ and FEAST-METAL, using 2-group constant volume (V1) and constant atom number (V2) versions of the codes.

Figure 91: Cladding hoop strain for 14 node FEAST-METAL and 13 node CAFÉ at 15.8 at% burnups with constant volume (V1) and constant atom number (V2) fission gas release models [23]

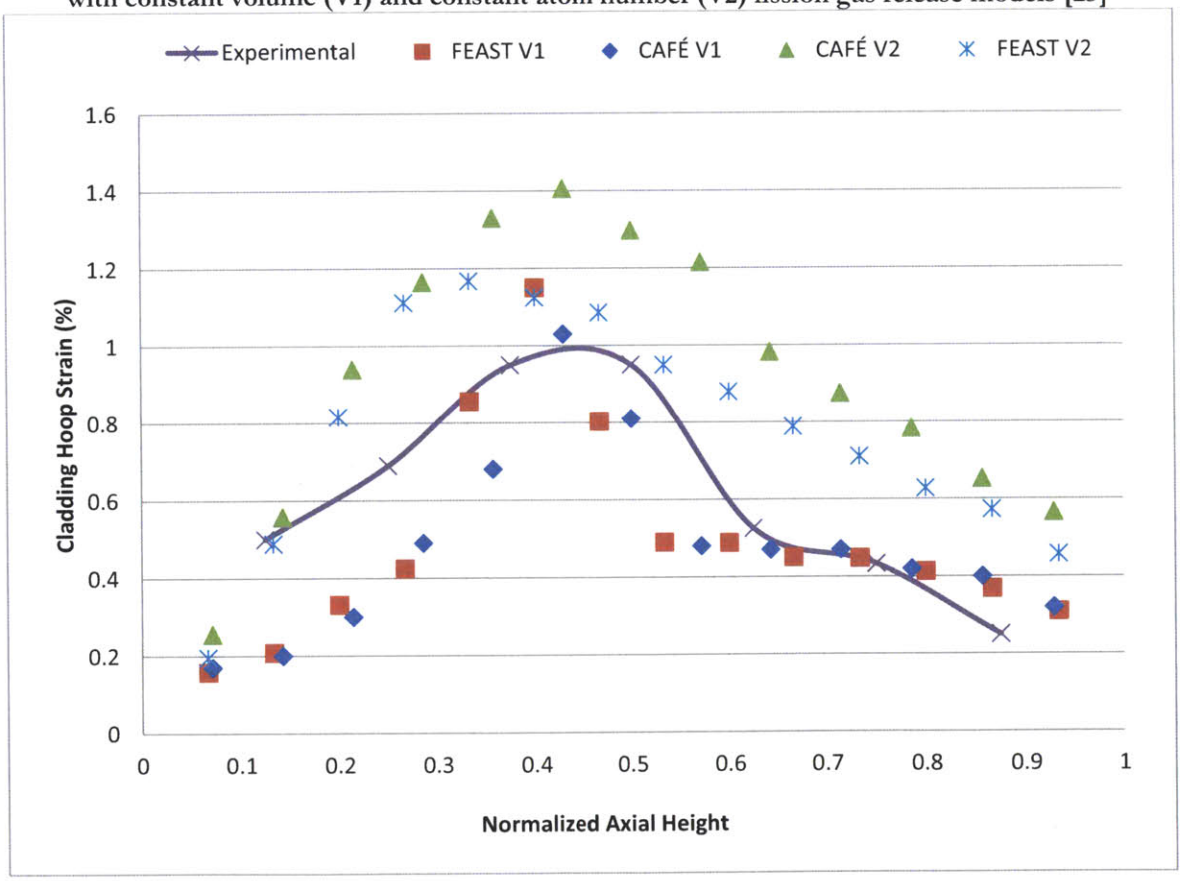

It can be seen that there is a large similarity in the results returned when the constant volume versions of FEAST-METAL are used (FEAST V1 and CAFÉ V1). However, when the constant atom number fission gas algorithm is used with FEAST-METAL in CAFÉ (CAFÉ V2), a large increase in the predicted cladding strain is seen. This indicates that this version of CAFÉ returns results that do not mirror the experimental data well enough; accordingly, it should not be used as an analysis tool, unless the fitting parameters are adjusted.

5.7. Code Runtime: Linearity Analysis

The code FEAST-METAL was also examined to ensure that runtime scaled linearly with both the time step used and the number of axial nodes used for analysis. First the runtime of four different runs were timed, each with a different number of nodes and time steps. This result can be seen in Table 26.

Table 26: Runtime (in seconds) for Version II of FEAST-METAL, varying nodes and time-steps on dedicated 3.33 GHz CPU

Time Step (s)	7 Nodes	20 Nodes
15	3368	9207
30	1657	4632

These runtimes were then analyzed to ensure they scaled linearly with both the number of nodes and time-step. To do this, the following equation was used. The results from the analysis are summarized in Table 27.

$$Runtime\ change\ fraction = \frac{\frac{Case\ Runtime}{Slowest\ runtime\ (7\ node, 30s)}}{Linear\ scaling\ of\ lowest\ runtime\ (nodes\ and\ timestep)}$$

Table 27: Runtime change fraction from increasing the number of nodes and time-step on dedicated 3.33 GHz CPU

Time Step (s)	7 Nodes	20 Nodes
15	1.02	0.97
30	1	0.98

It can be seen that the code maintains linearity when both the time-step and the number of nodes are changed.

5.8. Conclusions from Studies

The high variability of results from the alteration of the four fitting parameters indicates that more experimental work needs to be performed. This is especially true for the diffusion parameters used in the code, for which there are no data for irradiated fuel. There is also little information available on diffusion characteristics of low temperature phases. The compressibility also has not been well characterized experimentally. The high sensitivity of the code results to the fitting parameters indicates that they are all phenomena that need to be further examined.

The code showed minimal dependence on the length of the user-specified time-step for all versions of the code. Additionally, there is little dependence of cladding strain and fission gas release results on axial resolution. However, if the axial resolution is not small enough, it is possible to miss local peaks in the calculated results. If the size of axial nodes is less than 10% of the length of the fuel, then the probability of missing artificial maxima is greatly reduced.

The constant volume version of the code showed discontinuities in the region of the fuel with the maximum amount of strain. In contrast, the constant atom number version of the code did not show this discontinuity. It is thought that this improved behavior results from the increased degrees of freedom in the latter version.

Comparing FEAST-METAL and CAFÉ while using both the 2-group constant atom number and constant volume fission gas release and swelling modules, shows that using CAFÉ with the constant atom number approach produced unacceptable results. All other analyses (i.e. constant volume models and phase-dependent model) were acceptable.

Finally, the code was shown to scale linearly with the number of axial nodes and the number of time-steps used in the code.

6. Summary, Conclusions and Future Work

6.1. Summary and Conclusions

Five new fission gas and swelling modules for the fast reactor metallic fuel code FEAST-METAL were incorporated and checked against the limited available experimental observations. The improvements and alterations made to the code were done in an attempt to increase the degrees of freedom in the code and make the models used in the code more scientifically based. All of the models developed were benchmarked against data from EBR-II that is in the open literature. Particularly, the code was benchmarked against U-19Pu-10Zr fuel and was applied to U-6Zr fuel. Modeling fuel swelling and fission gas generation for fast reactor fuels is of high importance since it is one of the main limiting factors in the development of metallic fast reactor fuel.

When metallic fuel is placed in a fast reactor it begins to rapidly expand due to the formation of fission gases within the fuel matrix. At first, single gas atoms form. These atoms migrate together, coalesce and form progressively larger bubbles within the fuel matrix, deforming it and causing swelling. Eventually these fission gases reach grain boundaries and migrate to the plenum. At ~10 at% burnup, these gases begin to be released to the plenum. While the fission gas is contained within the fuel, the bubbles are known as closed pores; after the fission gas reaches the boundary and begins to be released, these closed pores become open pores because they are connected to the plenum. Once the fuel comes into contact with the cladding the open pores begin to be sintered due to the contact pressure, reducing their total volume. Proceeding concurrently with the generation of fission gas bubbles is the generation of solid fission gas products, which results in ~ 1.2% volumetric swelling per 1.0 at% burnup.

The rates of fission gas release from the fuel and fuel swelling are dependent on a large number of parameters, the most important of which are fuel operating history, initial metallic composition and manufacturing process. This results in a large interdependence between fission gas and swelling with fuel chemistry, fuel phase structure, fuel temperature distribution, and the fuel-cladding interactions, both FCCI and FCMI. How fission gas is treated in the code alters the code predictions drastically for a large number of these importance phenomena. Therefore, five new models of the fission gas and swelling module were developed for the FEAST-METAL. While all versions

maintain the GRSIS algorithm already implemented in the code, they provide various means of increasing the degrees of freedom and limit the dependence on fitting parameters.

The first alteration made to the code increased the number of closed bubble groups within the GRSIS from two to three and then to four. This was done because the rate at which fission gas is released into the plenum in the GRSIS algorithm directly depends on the rates at which gas bubbles are transferred from one group to another and eventually the plenum. A large number of groups would better characterize this process of gas release.

The next alteration allowed the radii of bubble groups to become capable of varying with time. In order to do this, bubble groups were defined based on the number of atoms in the bubble and not the size of the bubble. Through a van der Waals relation, the radius of the bubble group was made dependent on the temperature and the pressure exerted on the bubble. The alterations made to the code resulted in a fourth fitting factor being added to the three already present in the code (surface area correction factor, diffusion constant and open pore formation constant). This altered the compressibility of the fuel so that fractional fission gas release could be fitted in conjunction with cladding strain.

Next, the fission gas model was altered to include a dependence on the phase of the fuel. FEAST-METAL approximates the ternary fuel structure of the U-Pu-Zr matrix by a binary one at a constant plutonium concentration. This results in the fuel having three different phase regions at operating temperatures (which correspond well to the actual three phase nature of the fuel). In the center there is the single-γ region. In the intermediate zone, there is a $\beta + \gamma$ region. In the outer region, the fuel is primarily $\alpha + \delta$. Each of these phases has different structural properties and morphologies. The different morphologies result in different fission gas bubble behavior. In the central zone, the fission gas bubbles form large spheres; in the intermediate zone, the gas forms spherical bubbles of medium size; in the outer region, the gas forms ellipsoidal bubbles along grain boundaries - expanding in two directions along the interface while being constrained in the one normal to the interface plane. These effects were modeled and placed into the constant atom number version of the code.

The final alteration applied to the code was to modify the bubble spacing equations for closed bubble groups to become dependent on the results of a Monte-Carlo algorithm written to simulate bubble generation in a uniform matrix. The results from this study replaced the bubble to bubble distance equations in the code, which were previously based on the assumption that the bubbles form a uniform FCC lattice.

All of these codes were benchmarked against EBR-II assemblies X425 and X430. The resultant benchmarks were then used to evaluate a long-term irradiation similar to one that would be performed in the Travelling Wave Reactor. Analyses of the benchmarks showed that the two group constant volume code and the phase dependent code with FCC lattice spacing equations had the best combination of accuracy and runtime. Of these two codes, the phase dependent constant atom number version showed continuous behavior over the entire fuel length. In contrast, the constant volume version of the code showed a sharp discontinuity in certain axial regions. It was also determined that a third benchmark case is needed to determine which is more valid, since both exhibit different behaviors when analyzing the long-term case. Some of the difference may be attributed to the fact that the benchmark cases are both U-19Pu-10Zr igniter fuel. The long-term irradiation case is U-6Zr, which first starts in the outer blanket.

When the codes were used to analyze the long-term case, they showed that it will be difficult for the fuel to survive to high burnups near ~35 at%. The capability of the clad and fuel matrix to withstand the total projected neutron dose is in doubt. The dose would result in atom displacements on the order of ~500 dpa, which is much above current irradiation data for this material, especially when the unique environment and constantly expanding fuel are taken into account.

The four group constant volume version of the code and the phase dependent version of the code with bubble distance equations based on the FCC lattice were used to perform sensitivity studies on the four fitting factors used in the benchmarking of the code. These studies were used to show how the cladding strain and fission gas release results varied depending on these values. They also showed the range of applicability for the fitting factors. The most striking result of this study was the large dependence of fuel swelling, and thus cladding strain, on the effective porosity correction factor used for constant atom number benchmarks.

Lastly, the two group constant volume and the two group phase dependent version of the code were run with 7, 14 and 20 axial nodes for time-steps from 10 to 50 seconds. Both versions showed little dependence on the user-specified time-step. They also showed that the code was numerically unstable if the time-step is set to more than 30 seconds. Axial node resolution analyses indicated that the constant volume version of the code had a discontinuity at the point of maximum cladding strain. This leads to over prediction of cladding hoop strain, especially at higher burnups. This discontinuity was not noticed in the phase dependent version of the code. Both versions showed little dependence on axial resolution for cladding strain results. However, if the axial mesh size is too large then the true maxima may be missed.

Given this, the version of the code which provides the best compromise between stability, accuracy and time is the phase dependent version of the code. However, it was found that when this module was used in the code CAFÉ, which couples FEAST and COBRAIV, unacceptable results were returned. It seems that the CAFÉ code was fitted with the original FEAST models, and that changing the fuel swelling models affects its accuracy.

6.2. Future Work

Ideally more experimental data needs to be available to perform a better benchmark of the code. Current benchmarks make use of only igniter fuel of U-19Pu-10Zr composition. This may inherently limit the applicability of the code since the irradiation histories of breeder (blanket) and igniter fuels are drastically different.

More information on the diffusion behavior of fission gas in an irradiated fuel pin for all of the phases present would be very useful in developing a better benchmark for the code. It would effectively eliminate one of the fitting factors. Along the same lines, if more work were performed to determine the compressibility of low temperature phases, not just the single gamma phase, then some of the questions of fuel compressibility would be resolved.

The benchmarking of the FEAST-METAL algorithm, which is used in CAFÉ, should be examined to improve the accuracy of CAFÉ. The new coolant model may require new fitting parameters.

Works Cited

[1] TerraPower, LLC, "Traveling-Wave Reactors: A Truly Sustainable and Full-Scale Rescource for Global Energy Needs," in *Proceeding of ICAPP 2010*, San Diego, CA, 2010.

[2] R. G. Pahl, D. L. Porter, D. C. Crawford and L. C. Walters, "Irradiation Behavior of Metallic Fast Reactor Fuels," *Journal of Nuclear Materials,* vol. 188, pp. 3-9, 1992.

[3] G. L. Hofman and R. S. Wisner, "Steady-state Irradiation Testing of U-Pu-Zr Fuel to >18 at% Burnup," in *International Fast Reactor Safety Meeting* , Idaho Falls, 1990.

[4] A. Karahan, *Doctoral Thesis: Modeling of Thermo-Mechanical and Irradiation Behavior of Metallic and Oxide Fuels for Sodium Fast Reactors,* Massachusetts Institute of Technology, 2009.

[5] G. L. Hofman, L. C. Walters and T. H. Baur, "Metallic Fast Reactor Fuels," *Progress in Nuclear Engineering* , vol. 31, pp. 83-110, 1997.

[6] G. L. Hofman, "Irradiation Behavior of Experimental Mark-II Experimental Breeder Reactor II Driver Fuel," *Nuclear Technology,* vol. 47, pp. 7-20, 1980.

[7] L. C. Walters, "Thirty Years of Fuels and Materials Information from EBR-II," *Journal of Nuclear Materials,* vol. 270, pp. 39-48, 1998.

[8] D. Porter, C. Lahm and R. Pahl, "Fuel Constituent Redistribution during the Early Stages of U-Pu-Zr Irradiation," *Metallurgical Transactions A,* vol. 21A, pp. 1871-1876, 1990.

[9] S. Kim, G. L. Hofman, S. L. Hayes and Y. H. Sohn, "Constituent Redistribution in U-Pu-Zr Fuel during Irradiation," *Journal of Nuclear Materials,* vol. 327, no. 1, pp. 27-36, 2004.

[10] G. Hofman, R. G. Pahl, C. E. Lahm and D. L. Porter, "Swelling Behavior of U-Pu-Zr Fuel," *Metallurgical Transactions A,* vol. 21A, pp. 517-528, 1990.

[11] R. G. Pahl, D. Porter, C. E. Lahm and G. L. Hofman, "Experimental Studies of U-Pu-Zr Fast Reactor Fuel Pins in the Experimental Breeder Reactor-II," *Metallurgical Transactions A,* vol. 21A, pp. 1863-1870, 1990.

[12] T. Kobayashi, M. Kinoshita, S. Hattori, T. Ogawa, Y. Tsuboi, M. Ishida, S. Ogawa and H. Saito, "Development of the SESAME Metallic Fuel Performance Code," *Nuclear Technology,* vol. 89, pp. 183-193, 1989.

[13] Y. Tsuboi, T. Ogata, M. Kinoshita and H. Saito, "Mechanistic Model of Fission Gas Behavior in Metallic Fuel," *Journal of Nuclear Materials,* vol. 188, pp. 312-318, 1992.

[14] T. Ogata, M. Kinoshita, H. Saito and T. Yokoo, "Analytical study on the deformation and fission gas behavior of metallic fas reactor fuel," *Journal of Nuclear Materials,* vol. 230, pp. 129-139, 1996.

[15] W. Hwang and e. al., "MACSIS: A Metallic Fuel Performance Analysis Code for Simulating In-Reactor Behavior under Steady-State Conditions," *Nuclear Technology,* vol. 123, pp. 130-141, 1998.

[16] A. Karahan and J. Buongiorno, "A New Code for Predicting the Thermo-mechanical and Irradiation Behavior of Metallic Fuels in Sodium Fast Reactors," *Journal of Nuclear Materials,* vol. 396, no. 2-3, pp. 283-293, 2010.

[17] C. B. Lee, D. H. Kim and Y. H. Jung, "Fission gas release and swelling model of metallic fast reactor fuel," *Journal of Nuclear Materials,* vol. 288, pp. 29-42, 2000.

[18] S. M. McDeavitt and A. A. Solomom, "Hot-Isostatic Pressing of U-10Zr by a Coupled Grain Boundary Diffusion and Creep Cavitation Mechanism," *Journal of Nuclear Materials,* vol. 228, pp. 184-200, 1996.

[19] T. Ogata and T. Yokoo, "Development and Validation of ALFUS: An Irradiation Behavior Analysis Code for Metallic Fast Reactor Fuels," *Nuclear Technology,* vol. 128, pp. 113-123, 1999.

[20] E. E. Gruber and J. M. Kramer, "Gas-Bubble Growth Mechanisms in the Analysis of Metal Fuel Swelling," in *Radiation-Induced Changes in Microstructure: 13th International Symposium (Part 1) ASTM STP 955*, 432-444, 1987.

[21] K. Aydin and N. Andrews, MIT Departement of Nuclear Science and Engineering, Unpublished Paper in Review, 2011.

[22] D. Crawford, S. Hayes and R. Pahl, "Large-Diameter, High-Plutonium Metallic Fuel Testing in EBR-II," *Transactions of the American Nuclear Society,* vol. 71, pp. 178-179, 1994.

[23] J. Fricano, Doctoral Thesis, "Integrated Fuel Performance and Thermal-Hydraulic Sub-channel Models for Analysis of Sodium Fast Reactors," Massachusetts Institute of Technology, 2012.

[24] A. Karahan, "FEAST-METAL Version-1 User's Manual," Center for Advanced Nuclear Energy Systems, Cambridge, MA, 2010.

[25] W. Steele, A. R. Wazzan and D. Okrent, "Steady-state Fission Gas Behavior in Uranium-Plutonium-Zirconium Metal Fuel Elements," *Nuclear Engineering and Design,* vol. 113, pp. 289-295, 1989.

Appendix A: X425 Main Input Deck for FEAST-METAL

This appendix shows the main input deck used for the X425 assembly benchmark from EBR-II. The FEAST-METAL Version 1 Manual contains a description of the input files, their required formatting and the units are used. This manual and the FEAST-METAL executable are available from RSICC. [24]

```
"FEAST: metal fuel code"
im= 50
na= 7
dt= 10.0
ptof= 1.0
rfo= 2.16e-03,2.16e-03,2.16e-03,2.16e-03,2.16e-03,2.16e-03,2.16e-03
rci= 2.539e-03
rco= 2.92e-03
rw= 0.71e-03
xpu= 0.19
xzr= 0.10
fgpav= 0.84E5
bonds= 6.35e-03
lfu= 0.049,0.049,0.049,0.049,0.049,0.049,0.049
pco= 1.0e5
tcin= 370.0
time= 0.000E+00,0.198E+00,0.198E+00,0.329E+00,0.329E+00,0.344E+00,
0.344E+00,0.512E+00,0.512E+00,0.598E+00,0.598E+00,0.775E+00,0.775E+00,
0.775E+00,0.775E+00,0.938E+00,0.938E+00,0.101E+01,0.101E+01,0.105E+01,
0.105E+01,0.105E+01,0.105E+01,0.107E+01,0.107E+01,0.114E+01,0.114E+01,
0.116E+01,0.116E+01,0.125E+01,0.125E+01,0.131E+01,0.131E+01,0.150E+01,
0.150E+01,0.152E+01,0.153E+01,0.152E+01,0.152E+01,0.158E+01,0.158E+01,
0.158E+01,0.158E+01,0.176E+01,0.176E+01,0.176E+01,0.176E+01,0.190E+01,
0.190E+01,0.344E+01
tout= 0.559E+03,0.559E+03,0.559E+03,0.553E+03,0.553E+03,0.547E+03,
0.547E+03,0.541E+03,0.541E+03,0.557E+03,0.557E+03,0.534E+03,0.534E+03,
0.509E+03,0.509E+03,0.522E+03,0.522E+03,0.522E+03,0.522E+03,0.505E+03,
0.505E+03,0.527E+03,0.527E+03,0.526E+03,0.526E+03,0.518E+03,0.518E+03,
0.516E+03,0.516E+03,0.514E+03,0.514E+03,0.514E+03,0.514E+03,0.516E+03,
0.516E+03,0.510E+03,0.510E+03,0.514E+03,0.514E+03,0.514E+03,0.514E+03,
0.511E+03,0.511E+03,0.510E+03,0.510E+03,0.510E+03,0.510E+03,0.510E+03,
0.510E+03,0.510E+03
dos= 5.0
tfre= 10.0
pres= 3.0e+8,3.0e+5,10.0
tr= 0
```

Appendix B: X430 Main Input Deck for FEAST-METAL

This appendix shows the main input deck used for the X430 assembly benchmark from EBR-II. [24]

```
"FEAST-M: metal fuel code"
im= 50
na= 7
dt= 10.0
ptof= 1.4
rfo= 2.858e-03,2.858e-03,2.858e-03,2.858e-03,2.858e-03,2.858e-03,2.858e-03
rci= 3.277e-03
rco= 3.683e-03
rw= 0.710e-03
xpu= 0.19
xzr= 0.10
fgpav= 0.84E5
bonds= 6.35e-03
lfu= 0.049,0.049,0.049,0.049,0.049,0.049,0.049
pco= 1.0e5
tcin= 370.0
time= 0.000E+00,0.280E+00,0.284E+00,0.465E+00,0.469E+00,0.486E+00,
0.491E+00,0.724E+00,0.728E+00,0.846E+00,0.850E+00,0.110E+01,0.110E+01,
0.111E+01,0.111E+01,0.133E+01,0.133E+01,0.143E+01,0.143E+01,0.149E+01,
0.149E+01,0.150E+01,0.150E+01,0.151E+01,0.152E+01,0.161E+01,0.162E+01,
0.164E+01,0.164E+01,0.177E+01,0.178E+01,0.185E+01,0.186E+01,0.212E+01,
0.213E+01,0.215E+01,0.216E+01,0.216E+01,0.217E+01,0.223E+01,0.224E+01,
0.225E+01,0.226E+01,0.249E+01,0.250E+01,0.250E+01,0.251E+01,0.269E+01,
0.270E+01,0.283E+01
tout=  0.559E+03,0.559E+03,0.553E+03,0.553E+03,0.547E+03,0.547E+03,
0.541E+03,0.541E+03,0.557E+03,0.557E+03,0.534E+03,0.534E+03,0.509E+03,
0.509E+03,0.522E+03,0.522E+03,0.522E+03,0.522E+03,0.505E+03,0.505E+03,
0.527E+03,0.527E+03,0.526E+03,0.526E+03,0.518E+03,0.518E+03,0.516E+03,
0.516E+03,0.514E+03,0.514E+03,0.514E+03,0.514E+03,0.516E+03,0.516E+03,
0.510E+03,0.510E+03,0.514E+03,0.514E+03,0.514E+03,0.514E+03,0.511E+03,
0.511E+03,0.510E+03,0.510E+03,0.510E+03,0.510E+03,0.512E+03,0.512E+03,
0.512E+03,0.512E+03
dos= 5.0
tfre= 10.0
pres= 3.0e+8,3.0e+5,10.0
tr= 0
```

Appendix C: Long Term Case Main Input Deck for FEAST-METAL

This appendix shows the main input deck used for the long term case. [24]

```
"FEAST: metal fuel code"
im= 6
na= 10
dt= 20.0
ptof= 1.0
rfo= 3.00e-03,3.00e-03,3.00e-03,3.00e-03,3.00e-03,3.00e-03,3.00e-03,3.00e-03,3.00e-03,3.00e-03
rci= 3.873e-03
rco= 4.50e-03
rw= 0.71e-03
xpu= 0.0
xzr= 0.06
fgpav= 0.84E5
bonds= 6.35e-03
lfu= 0.20,0.20,0.20,0.20,0.20,0.20,0.20,0.20,0.20,0.20
pco= 1.0e5
tcin= 390.0
time= 0.000E+00,9.5E+00,10.5E+00,14.5E+00,15.5E+00,20.0E+00
tout= 0.550E+03,0.550E+03,0.535E+03,0.535E+03,0.540E+03,0.540E+03
dos= 4.02
tfre= 20.0
pres= 1.0e+6,1.0e+6,10.0
tr= 0
```